# Quantum Entanglement of the Spatial Modes of Light

Barry Jack

Submitted in fulfilment of the requirements for the Degree of Doctor of Philosophy

School of Physics and Astronomy

University of Glasgow

November 2011

# ABSTRACT

This thesis is a dissemination of the experimental work I have carried out in the last three and a half years, under supervision of Prof. Miles Padgett and Dr. Sonja Franke-Arnold. Presented within are seven unique experiments investigating the orbital angular momentum (OAM) states of light, and the associated spatial modes. Six of these experiments relate to measurements on quantum-entangled photon pairs produced in down-conversion.

The first chapter of my thesis is a brief review of the some of the contributions made to the field of research of OAM, both involving classical and quantum states of light. This chapter introduces some of the hallmark experiments within the subject, from which my experimental work reported in this thesis is inspired.

The second chapter details the set up of the down conversion experiment, and the experimental techniques used to design a fully functioning quantum measurement system. Most importantly, this includes the holographic techniques used to measure the spatial states of the photon pairs. In ad-

dition to holographic measurements, a system to holographically auto-align the down-conversion experiment was developed. Due to the sensitive nature of the experiments presented, this automated system has been crucial to the success of all of the single photon experiments presented within this document.

The experimental results are split into three separate categories. The first (Chapter 3) describes measurements investigating the Fourier relationship between OAM and angular position states, both at the classical and quantum levels. The following chapter (Chapter 4) consists of four experiments designed to quantify the degree of entanglement of states of OAM and angular position. This includes the first demonstration of the historic EPR (Einstein-Podolsky-Rosen) paradox for OAM and angle states, violation of a Bell-type inequality for arbitrary OAM states, and characterisation of the density matrices for a range of OAM state-spaces. The final chapter (Chapter 5) reports a new type of ghost imaging using down-converted photon pairs. In this experiment, we violate a Bell inequality within a ghost image, demonstrating the entangled nature of our system and contributing a new element to the long standing contention over quantum *vs.* classical features within ghost imaging.

These experiments have seen a wide range of collaboration. The experimental work on the Fourier relation on single photons was carried out in collaboration with Dr. Anand Kumar Jha (University of Rochester). The work on ghost imaging was performed with collaboration with Prof. Monika

Ritsch-Marte (Innsbruck Medical University), and the angular EPR paradox work was carried out in collaboration with Prof. Robert Boyd (Univ. of Rochester) and Prof. David Ireland (Univ. of Glasgow). The work I present here is experimental, however any theoretical developments are in a large part due to the support of Dr. Sonja Franke-Arnold and Prof. Steve Barnett (Univ. of Strathclyde).

# AUTHOR'S DECLARATION

I hereby declare that this thesis is the result of my own work, except where explicit reference is made to the work of others, and has not been presented in any previous application for a degree at this or any other institution.

.....

Barry Jack

# CONTENTS

# LIST OF FIGURES

# ACKNOWLEDGEMENTS

For the help and support I have received over the past few years, there are simply too many people to acknowledge! Every one of my friends and co workers have all helped in their own way at different times, and you all know who you are.

Firstly, thanks go to my supervisor Miles, for all you have taught me, and for the opportunities you have given me. Special thanks to Jonathan Leach, who (patiently!) worked with me throughout my PhD and whom I learned much from. I would also like to thank all of those who I worked with at different times; Dr. Sonja Franke-Arnold, Prof. Steve Barnett, Dr. Alison Yao, Dr. Kevin O'Holleran, Dr. Ryan Warburton, Jacqui Romero and Filippo Miatto - It has truly been a pleasure.

Thanks go to the entire cast of the Optics Group, which is the most pleasant and creative environment to work in. In particular to Aline Vernier, Martin Lavery, Graham Gibson, Richard Bowman, Johannes Courtial, and Arran Curran - You have all been a constant presence throughout my time

in the group, and have kept me going.

Also, thanks to my parents Val and Steven. I wouldn't have gotten anywhere without your continual support, which manifests itself in many different ways.

# PUBLICATIONS

## Peer-Reviewed Publications

- **Angular Diffraction** Jack B, Padgett M and Franke-Arnold S *New Journal of Physics* **10** 103013 (2008)

- **Fourier relationship between the angle and angular momentum of entangled photons** Jha A, Jack B, Yao E, Leach J, Boyd R, Buller G, Barnett S, Franke-Arnold S and Padgett M *Physical Review A* **78** 4 043810 (2008)

- **Violation of a Bell inequality in two-dimensional orbital angular momentum state-spaces** Leach J, Jack B, Romero J, Ritsch-Marte M, Boyd R, Jha A, Barnett S, Franke-Arnold S and Padgett M *Optics Express* **17** 10 pp.8287-8293 (2009)

- **Holographic Ghost Imaging and the Violation of a Bell Inequality** Jack B, Leach J, Romero J, Franke-Arnold S, Ritsch-Marte

M, Barnett S and Padgett M *Physical Review Letters* **103** 03602 (2009)

- **Precise Quantum Tomography of Photon Pairs with Entangled Orbital Angular Momentum** Jack B, Leach J, Ritsch H, Barnett S, Padgett M and Franke-Arnold S *New Journal of Physics* **11** 103024 (2009)

- **Angular Two-Photon Interference and Angular Two-Qubit States** Jha A, Leach J, Jack B, Franke-Arnold S, Barnett S, Boyd R and Padgett M *Physical Review Letters* **104** 1 010501 (2010)

- **Isolated Optical Vortex Knots** Dennis M, King R, Jack B, O'Holleran K and Padgett M *Nature Physics* **6** 2 pp.118-121 (2010)

- **Entanglement of Arbitrary Superpositions of Modes Within Two-Dimensional Orbital Angular Momentum Subspaces** Jack B, Yao A, Leach J, Franke-Arnold S, Ireland D, Barnett S and Padgett M *Physical Review A* **81** 4 043844 (2010)

- **Quantum Correlations in Optical Angle-Orbital Angular Momentum Variables** Leach J, Jack B, Romero J, Jha A, Yao A, Franke-Arnold S, Ireland D, Boyd R, Barnett S and Padgett M *Science* **329** 5992 pp. 662-665 (2010)

- **High-Dimensional Quantum Nature of Ghost Angular Young's Diffraction** Chen L, Leach J, Jack B, Padgett M, Franke-Arnold S, and She W *Physical Review A* **82** 3 033822 (2010)

- **Violation of Leggett Inequalities in Orbital Angular Momentum Subspaces** Romero J, Leach J, Jack B, Barnett S, Padgett M and Franke-Arnold S *New Journal of Physics* **12** 123007 (2010)

- **Entangled Optical Vortex Links** Romero J, Leach J, Jack B, Dennis M, Franke-Arnold S, Barnett S and Padgett M *Physical Review Letters* **105** 100407 (2011)

- **Demonstration of the Angular Uncertainty Principle for Single Photons** Jack B, Aursand P, Franke-Arnold S, Ireland D, Leach J, Barnett S and Padgett M *Journal of Optics* **13** 064017 (2011)

*I would call this not one but the characteristic trait of quantum mechanics, the one that enforces the entire departure from the classical lines of thought*

– Erwin Schrödinger on Quantum Entanglement

CHAPTER

# ONE

# INTRODUCTION

## 1.1 Preamble

Perhaps the most significant paradigm shift in physics within the past century occurred with the development of quantum theory. As a relatively young field of study, the theoretical developments occurred at a rapid pace. Even more recent are the experimental tests of quantum mechanics. The theoretical foundations of quantum physics were laid down within the turn of the $20^{th}$ century, around 100 years ago, whereas most experiments in quantum mechanics became technologically possible only within the last 50 years. Experimental quantum optics - laboratory observations of the quantum states of light, have only been technically possible within the last 30 years. With technology advancing at such a rapid pace, new observations are still being

made in quantum optics today. As technology continues to advance, even more are we able to test previously untested theories and make observations in new and different ways.

## 1.2 Light as a Scalar Wave Field

A full description of wave fields is essential to a description of light, both at the classical and quantum level. The most readily observed property of light is Fermat's principle, that is, light behaving as rays. A ray contains only a small amount of the information contained in the wave optical description; the direction of a ray is perpendicular to the wavefronts of the wave, meaning the ray has the same direction as the wave vector $\mathbf{k}$, Fig. 1.1. However, because rays contain no phase information, ray optics does not adequately describe interactions at a distance scale of the order of the wavelength of light. In particular, ray optics cannot describe interference phenomena, such as diffraction.

An optical wave with a single direction component is a plane wave, and can be represented in complex notation, as

$$\psi = A_0 e^{i\Phi} \tag{1.1}$$

where $\Phi = kz$ is the phase change of the plane wave upon propagation through a distance $z$, with wavenumber $k = \frac{2\pi}{\lambda}$.

By Fourier analysis, any spatially distributed wave field can be decom-

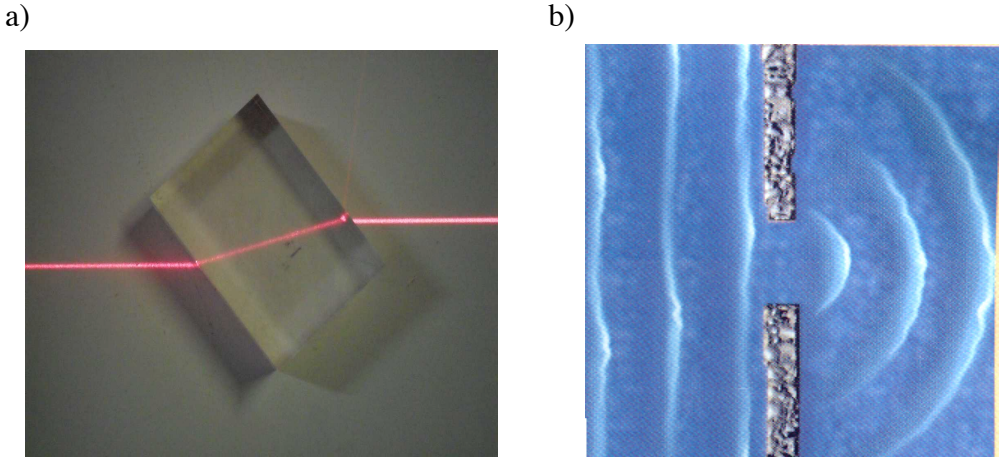


Figure 1.1: a) The propagation direction of a well-collimated laser beam can be described using ray optics (Image: http://www.electrosound.co.uk). b) Illustration of water waves diffracting at an aperture. The wavelength of the water waves is comparable to the size of the aperture. (Image: http://www.upscale.utoronto.ca/PVB/Harrison/Diffraction/Diffraction.html)

posed into its plane wave components. In 1-D, any function $f(z)$ can be decomposed into a sum of sine waves with given amplitudes, frequencies and phases. For sine waves with periodic boundary conditions, this is expressed as the sum:

$$f(z) = \sum_{n=-\infty}^{+\infty} c_n e^{ik_n z}, \tag{1.2}$$

or more specifically for our purposes:

$$f(z) = \frac{1}{\sqrt{2\pi}} \int_{-\infty}^{\infty} A_k e^{ikz} \mathrm{d}k, \tag{1.3}$$

where $A_k$ describes the amplitude of each plane wave $e^{ikz}$ component of $f(z)$. The equation above is the Fourier transform of the spatial distribution, translating a distribution in position to a distribution in momentum. Symmetrically, a momentum distribution $A_k$ can be expressed as a sum of position states,

$$A(k) = \frac{1}{\sqrt{2\pi}} \int_{\infty}^{\infty} f(z) e^{-ikz} \mathrm{d}z. \tag{1.4}$$

This relationship between $z$ and $k$ means that confining the wave within a bounded region $z$ introduces additional frequency components. For example, a pulsed wave is confined spatially, but is composed of a range of frequencies, as dictated by equations (1.3) and (1.4). These equations together form the Fourier relationship between $z$ and $k_z$. Variables which are related by a Fourier transform are called conjugate variables.

Variables which are related by a Fourier transform are also fundamentally linked to each other with an uncertainty relationship. At the quantum level, Heisenberg's uncertainty principle relates quantum measurements of conjugate variables[1], but classically, an uncertainty relation can be explained from the principle of diffraction. Consider a plane wave travelling in 1 direction in space, Fig. 1.2. This wave can be expressed by $e^{ikz}$, and has a wavevector, $\mathbf{k}$, in the direction of propagation. For this to be true, the plane wave must extend to $\pm\infty$ in the transverse direction, $x$. Expressed in another way, the wavevector $\mathbf{k}$ is known with absolute certainty, while the position $x$ remains

completely uncertain (or undefined). If we wish to locate the wave within the transverse region $\Delta x$, by an aperture for example, we inevitably spread the transverse momentum by $\Delta k$ through diffraction at the aperture. From the Fourier relationship above, as we restrict the aperture size $\Delta x$ we increase the effect of diffraction, and spread $\Delta k$.

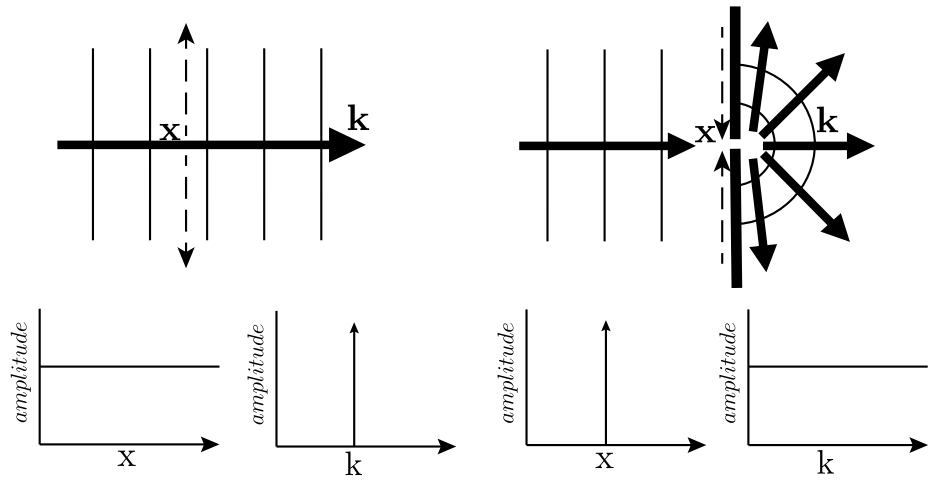


Figure 1.2: Extreme cases of the uncertainty relation between position and wavevector. a) A plane wave is unbound in space, and corresponds to a single wavevector component. b) Confining the positional variable spreads the momentum through diffraction, with the extreme case of a delta function in position corresponding to an unbound momentum distribution.

By analysis of equations (1.3) and (1.4), one can evaluate that the position and wave number are related by $\Delta k = 1/2\Delta x$. Thus the uncertainty relationship between $x$ and $k$ is

$$\Delta x \Delta k_x \geq \frac{1}{2}. \tag{1.5}$$

One can derive uncertainty relations for other conjugate variables using the same Fourier analysis.

## 1.3 Angular Momentum of Light

It has been known since Maxwell's equations, that light carries linear momentum[2]. A less well known property of light is its angular momentum, which in most cases can be separated into spin angular momentum (SAM)[3] and orbital angular momentum (OAM)[4] components.

### 1.3.1 Spin Angular Momentum

The origin of SAM is the rotation of the electric field of light as it propagates. The polarization of light is the direction of the electric field oscillation as it propagates. If the field oscillates in a single plane, the light is linear polarized. If it rotates around the propagation axis, then the light is circular polarized. This rotation can be clockwise (right hand, $\sigma = +1$) or counter-clockwise (left hand, $\sigma = -1$), with respect to the direction of propagation. The polarization states of light can be represented as a point on the Poincaré sphere[5] Fig. 1.3.

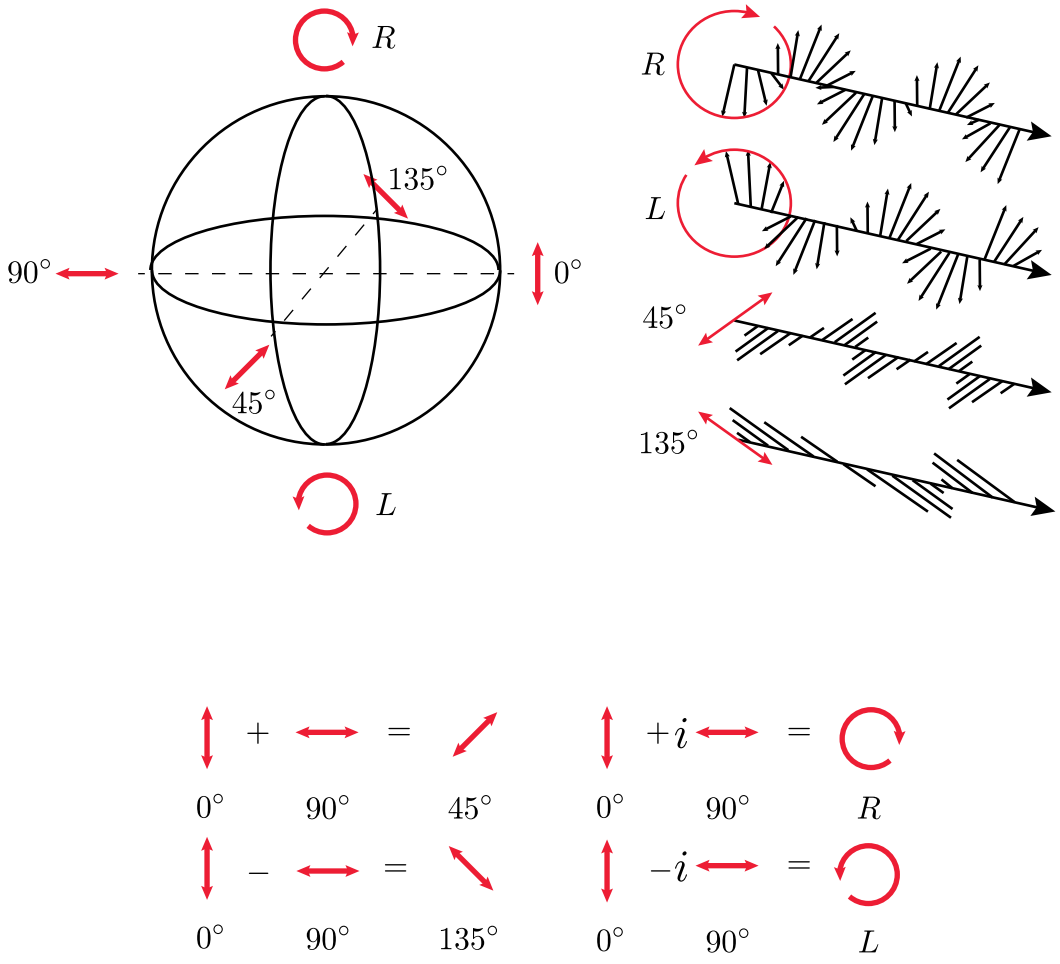


Figure 1.3: Polarization states can be represented on a Poincaré sphere. Each point on the sphere corresponds to a different direction of the oscillating field vectors. Typically, the chosen bases are circular polarization (north and south poles) and the linear states (equatorial).

Using this representation, right hand circular (r.h.c.) and left hand circular (l.h.c) polarization states lie at the north and south pole respectively. On the equator lie the linear polarization states which carry no SAM ($\sigma = 0$). States which lie between the equator and the poles correspond to states of elliptical polarization. R.h.c. and l.h.c. polarizations can be expressed as superpositions of linear polarization states and vice versa. Indeed, any general point on the Poincaré sphere can be expressed as a superposition of two other states.

### 1.3.2 Orbital Angular Momentum

Whereas spin arises due to the rotating electric field of the light wave, OAM arises due to the direction of energy flow around the beam axis (described by the Poynting vector[6]). Examples of light modes which carry OAM are the Laguerre-Gaussian modes[7], Fig. 1.4. A light field where the direction of energy flow rotates around the beam axis upon propagation, has phase-fronts (surfaces of constant phase) which are helical in form. A light field of this form can be described in a cylindrical coordinate system:

$$\Psi(r, \phi, z) = \Psi_0(r, z)e^{i\ell\phi}, \tag{1.6}$$

where the OAM is characterized by the phase term $e^{i\ell\phi}$[8]. The $\ell$ term defines how many times the phase rotates azimuthally from 0 to $2\pi$ in one full cycle Fig. 1.5. The index $\ell$ is referred to as the azimuthal index. Unlike SAM

$$LG_{\ell,p} = C^{LG}_{\ell,p}\left(\frac{r\sqrt{2}}{w(z)}\right)^{|\ell|} exp\left(-\frac{r^2}{w^2(z)}L_p^{|\ell|}\right)\left(\frac{2r^2}{w^2(z)}\right)$$
$$\times exp\left(ik\frac{r^2}{2R(z)}\right) exp(i\ell\phi) exp(-i(2p+|\ell|+1)\zeta(z))$$

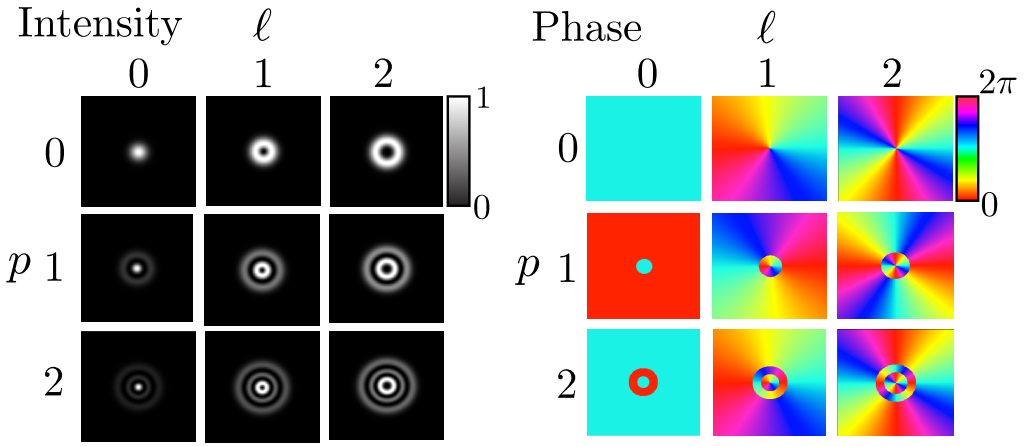


Figure 1.4: The amplitude of a Laguerre-Gaussian field, $LG_{\ell,p}$ is described by the equation (top). Shown below are examples of phase and intensity distributions as a function of the azimuthal index $\ell$ and the radial index $p$.

(which has two unique modes of rotation), the azimuthal index, $\ell$ is unbound and can take on any value.

Crucially for OAM, the phase rotates azimuthally, and the phase at the centre of the rotation axis is undefined. These phase singularities are ubiquitous in nature, and can occur through superpositions of random fields, such as optical speckle[9]. Because the phase is undefined on-axis, there is complete destructive interference in the vicinity of this point, and the intensity distribution contains an optical vortex with zero intensity at the centre. Conversely, nodes in an intensity field indicate which are stable upon propagation

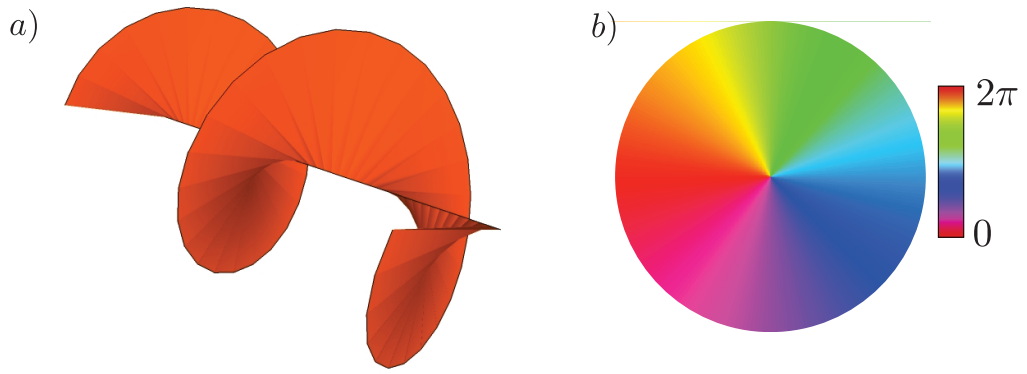


Figure 1.5: a) Phasefronts of a helically phased beam carrying OAM charge $\ell = +1$. b) Phase cross-section of a helical phased beam.

indicates singularities in the phase of the field.

The topological properties of light carrying OAM is a field of recent interest. Because the spiral phase is preserved upon propagation, optical vortices are remarkably stable, and are persist in all optical planes. Plotting a phase singularity as propagated through space shows that in theory the singular phase point, and the optical vortex, propagates from $z = -\infty$ to $z = +\infty$, Fig. 1.6 (a). By superposing light modes of differing OAM charge $\ell$, phase, and amplitude, it is possible to produces complex topological structures (such as loops, links and knots) of phase singularities which remain stable in space[10,11]. Because each OAM eigenstate has a different phase change upon propagation, due to the Gouy phase[8] of the Laguerre-Gauss modes, the constructive/destructive interference weaves the phase singularities in 3-dimensional space Fig. 1.6 (b). These topological features are expected to have analogies in other 3-D wave fields, such as in superfluids[12]

and Bose-Einstein condensates[13].

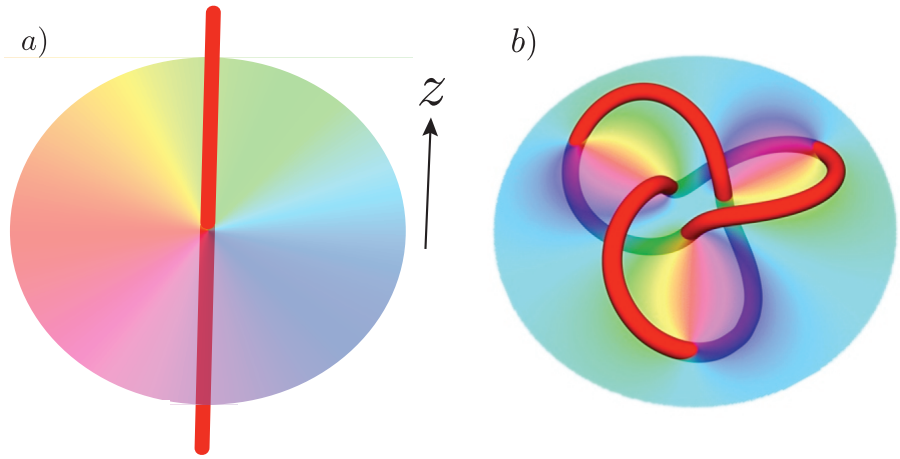


Figure 1.6: a) Propagation of the phase singularity of a Laguerre-Gauss mode with $\ell = 1$. The singular point propagates from $-\infty$ to $+\infty$. b) A trefoil knot is formed by the superposition of the modes shown. This light field is stable in space, and many different topologically distinct features (knots, loops and links) can be formed in this way. The phase cross-section shown here is of the beam-waist plane.

A key difference between SAM and OAM is that OAM is a spatial property of the light field. In circularly polarized light, the spin information exists in every point of the field, i.e. it is a local property of the light. The OAM state of light is a bulk, or global property of the field. This means, to fully determine the OAM of a light field, the entire field has to be measured. A small region of a helically phased beam measured independently appears

just as an inclined plane wave, Fig. 1.7, which contains no information about the OAM state. This property can in fact, be used to enhance security of communication. If OAM is used to communicate information, an eavesdropper cannot intercept the communication by measuring a small fraction of the beam, only by collecting the entire field which disrupts the communication[14].

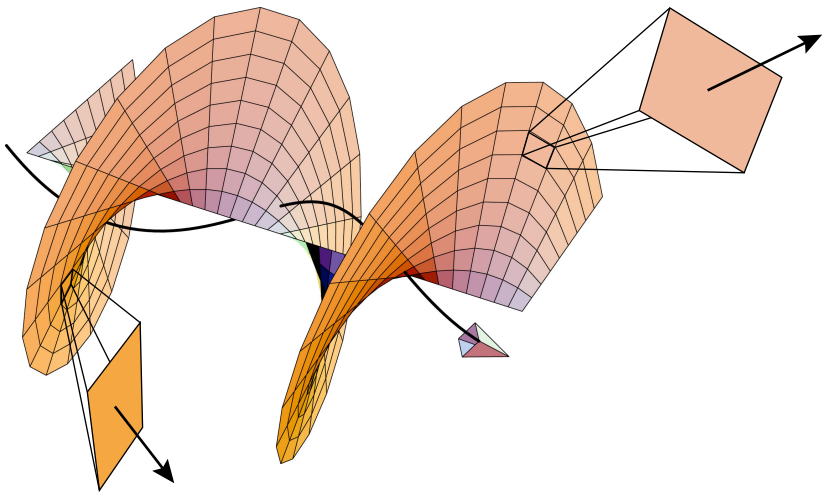

Figure 1.7: To measure the OAM state of light, it is required that the entirety of the field is measured. For this $\ell = 1$ spiral phase beam, a small section of the field appears as an inclined plane wave, carrying no OAM.

Pure OAM eigenstates can be superposed to create different spatial modes. Due to the unbound nature of the OAM states, the number of possible superposition states which can be formed is also infinite. A conceptually simpler place to start would be to first look at a 2-D subspace of the unbound OAM state-space. For example, consider a superposition of two opposite charged modes of equal amplitude, say, the Laguerre-Gauss modes $LG_{10}$ and $LG_{-10}$,

Fig. 1.8. The resulting superpositions no longer have a phase singularity, but a phase step between 0 and $\pi$. This arises from the modulo $2\pi$ addition of modes with counter-rotating phases. Changing the phase between these modes superposed corresponds to a rotation of the phase step. For this case, a $2\pi$ phase shift corresponds to a 360° rotation of the mode. The physical angle by which the phase step rotates as the phase angle changes is $\ell$ dependent. For example, for a superposition of $\ell = \pm 2$, a $2\pi$ phase shift corresponds to a 90° rotation of the mode.

These superpositions of two OAM eigenstates can be considered to be in a 2-D subspace of the potentially unbound OAM state-space. Restricting ourselves to these 2-D spaces, one can draw an analogy with the 2-D state-space of polarization. This analogy was formulated by Padgett and Courtial[15] by forming a Poincaré sphere equivalent for Laguerre-Gauss modes of $LG_{10}, LG_{-10}$, translating between the Laugerre-Gauss basis and the complementary Hermite-Gauss basis, Fig. 1.9.

This analogy is particularly true for the OAM state space of $\ell = \pm 1$ because, like with the electric field of circular polarized light, the phase rotates in a single helix around the propagation axis. It will also be useful to form Poincaré sphere equivalents for higher order OAM state-spaces.

The polarization variable has long been considered as the variable of choice in quantum systems such as quantum key distribution (QKD)[16], in part due to the ease of measurement (using polarizing filters or beam-splitters). In quantum information processing (QIP), spin states are often used as infor-

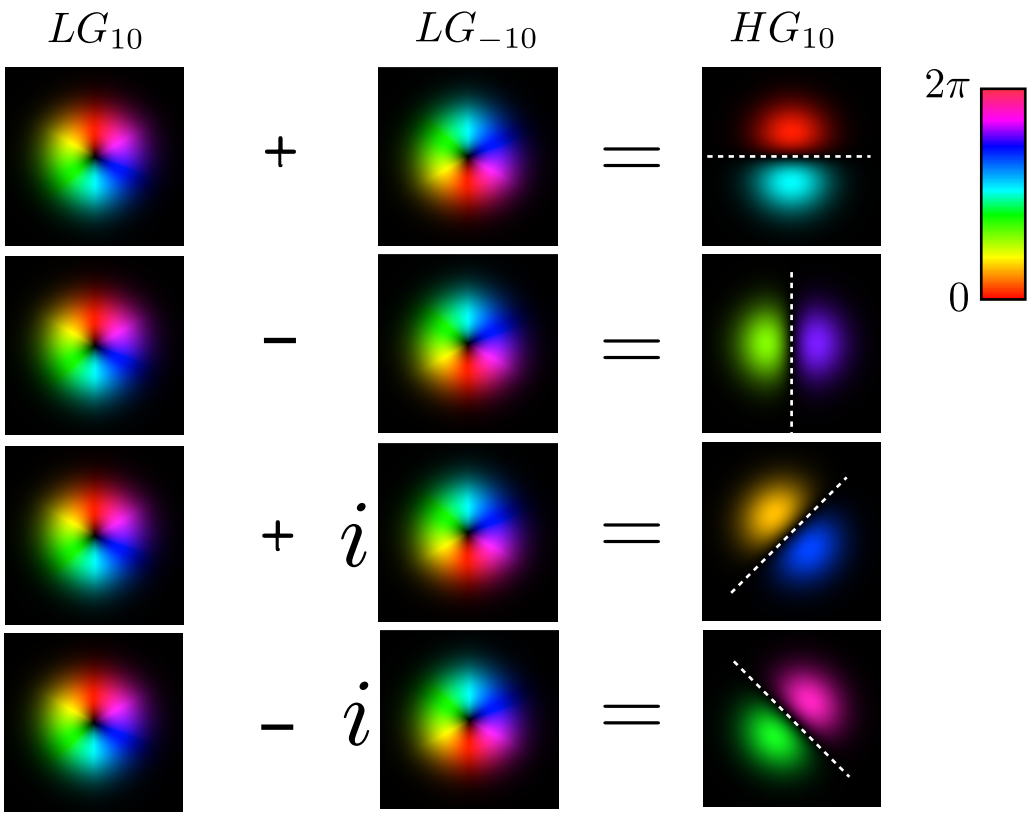


Figure 1.8: Laguerre-Gaussian states of $L = \pm 1$ can be added together in the same way as polarization states, as they exist within a 2-dimensional state-space. The orientation of the phase step is determined by the phase of the $LG$ states superposed, analogous with polarization.

mation states, called quBits. The Poincaré sphere for polarization provides a good mapping for quBits, where the poles represent the $\sigma = \pm 1$ spin states, and the equator represents the equally weighted $\sigma = 0$ states. The Poincaré sphere specifically describes the polarization states of light, however quBits can be represented by any 2-state quantum system in general. The Bloch sphere, named after physicist Felix Bloch, describes a 2-state quantum sys-

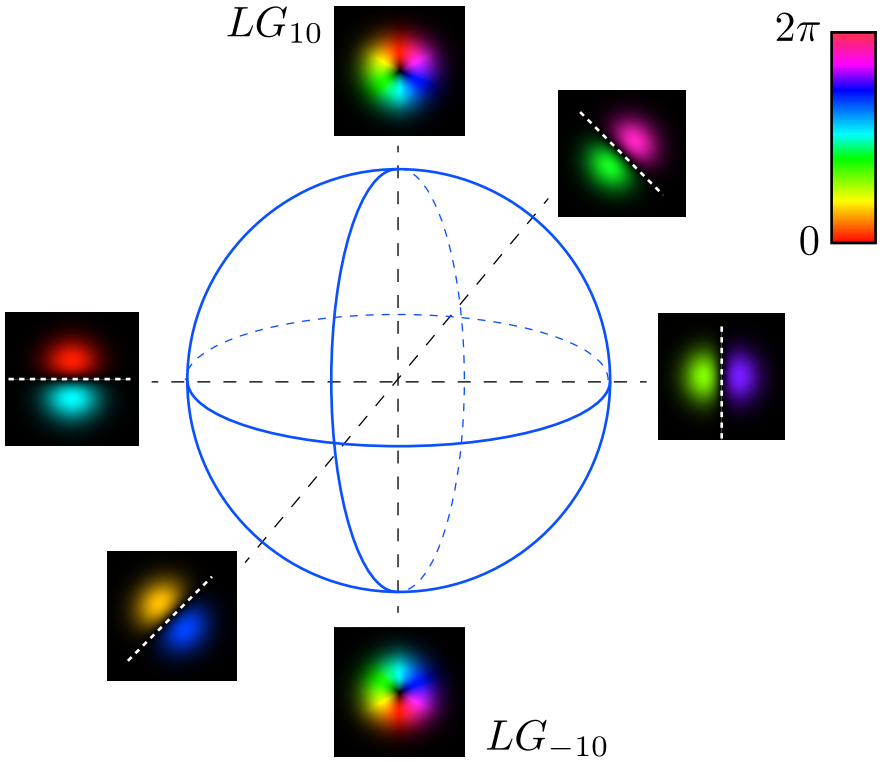


Figure 1.9: The Bloch sphere for Laguerre-Gauss and Hermite-Gauss modes of charge 1.

tem of states $|0\rangle$ and $|1\rangle$ (represented in Dirac notation[17]). A 2-D quantum state characterised by its OAM could be represented in this notation. Shown in Fig. 1.10 is a Bloch sphere equivalent[18] for superpositions of OAM states $|+\ell\rangle$ and $|-\ell\rangle$.

Consider a point on this sphere, characterised by spherical coordinates of $\theta$ and $\phi$. A state $|a\rangle$ is described by

$$|a\rangle = cos\left(\frac{\theta}{2}\right)|+\ell\rangle + e^{i\phi}sin\left(\frac{\theta}{2}\right)|-\ell\rangle \tag{1.7}$$

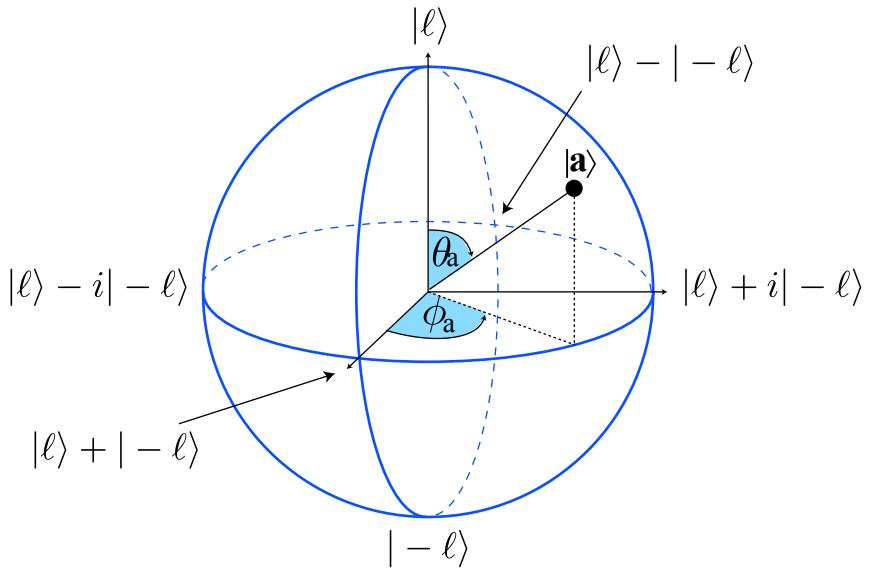


Figure 1.10: Generic Bloch sphere for OAM superposition states of $\pm\ell$.

At the north and south pole ($\theta = [0, 2\pi]$), we have either $|+\ell\rangle$ or $|-\ell\rangle$. At the equator ($\theta = \pi/2$), there are equal amplitudes of each. The $e^{i\phi}$ term describes the phase of addition of the two states, between 0 and $2\pi$. Less commonly encountered states are those which lie neither on the equator or at the poles of the Bloch sphere. These states are analogous to the elliptical polarization states on the Poincaré sphere.

### 1.3.3 Fourier Relationship Between Angle and OAM

Much like the Fourier relation linking variables of position and momentum, OAM is Fourier related with *angular position*. The amplitude of OAM states, $A_\ell$ is related by the angular function $\Psi(\phi)$ by

$$A_\ell = \frac{1}{\sqrt{2\pi}} \int_{-\pi}^{+\pi} \Psi(\phi) e^{-i\ell\phi} \mathrm{d}\phi \tag{1.8}$$

$$\Psi(\phi) = \frac{1}{\sqrt{2\pi}} \sum_{\ell=-\infty}^{\infty} A_\ell e^{i\ell\phi}. \tag{1.9}$$

An simple angular function is an aperture with an azimuthal opening angle of width $\phi$. This could be an aperture which varies in its transmission (with 0 transmission out with the region $\phi$ and maximum transmission inside the region), or a phase aperture (which shifts the phase within the defined angular region). By the above Fourier relation, any azimuthally varying angular function can be decomposed into a sum of harmonics with different $\ell$. See Fig. 1.11.

There are some notable differences between the linear position-momentum Fourier relation and this angular form. Firstly, the variables $x$ and $p$ are continuous and range from $-\infty$ to $+\infty$. An angular function, $\Psi(\phi)$ is continuous, but is also $2\pi$ cyclic. This $2\pi$ periodicity has led to discussion over whether or not angle can be an observable in quantum mechanics[19] (a periodic function has an ill-defined standard deviation). For our purposes it is sufficient to bound the function within the region $\pm\pi$. The periodic nature of angle is the reason that the OAM eigenstates $\ell$ are a discrete series of integers. Although light can have a fractional net OAM, it can always be expressed in terms of the integer OAM eigenstates[20].

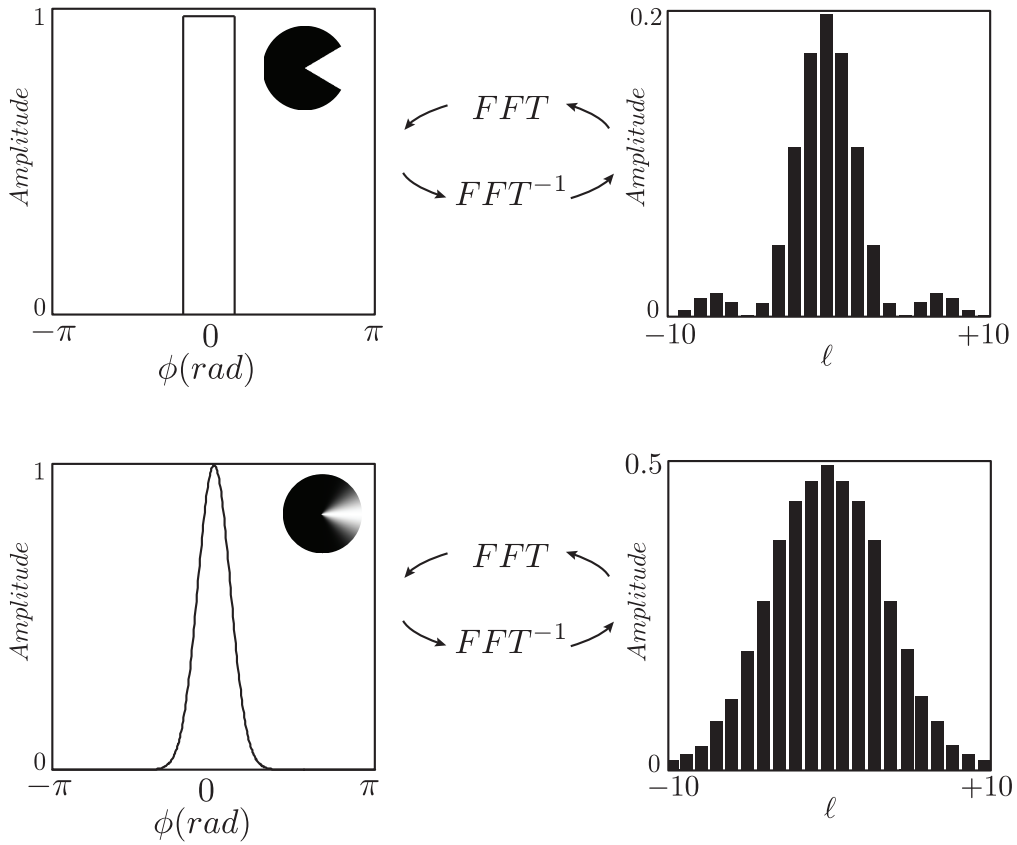


Figure 1.11: Fourier decomposition of an angular function. The upper diagram shows a narrow hard-edged angular amplitude function, which is composed of the modes shown with the appropriate weightings. The lower diagram shows an angular mask with Gaussian transmission function. The corresponding OAM spectrum is a Gaussian envelope of discrete eigenmodes.

### 1.3.4 Uncertainty Relationship Between Angle and OAM

From this angular Fourier relation, we can also consider an uncertainty relation between variables of $\ell$ and $\phi$. If we consider a light mode with no uncertainty in OAM (i.e. a pure OAM eigenstate), then by definition it cannot contain any angular information e.g. a Gaussian beam or a plane wave.

If we wish to restrict the angular distribution of such a beam, we could pass it through an angular aperture. In the position - momentum case restricting the position spreads the momentum due to diffraction. Here, by restricting the angle, we invoke the angular equivalent[21]. We know from the Fourier relation that a mode with an azimuthal dependence can be decomposed into a superposition of OAM states, given by the Fourier transform of the aperture. This OAM distribution is a discrete distribution, with an envelope which is determined by the Fourier transform of the aperture. For example, a hard edged aperture (Heaviside function) will result in an OAM spectrum with a $\mathrm{sinc}^2$ envelope, where as a Gaussian angular transmission will result in a Gaussian envelope of OAM states.

The angle-OAM uncertainty relation has properties which make it remarkably different form the familiar position-momentum uncertainty relation. The linear uncertainty relation $\Delta x \Delta k \geq 1/2$ is bound on the right hand side by a constant, meaning the minimum possible value of the product of the uncertainties of $x$ and $k$ is $1/2$. States which saturate the inequality are known as the *intelligent states*[22], and for the linear position-momentum variables the intelligent states are gaussian.

The uncertainty relation between angle and OAM is less familiar[23],

$$\Delta\phi\Delta\ell \geq \frac{1}{2}|1 - 2\pi P(\theta)| \tag{1.10}$$

where $P(\theta)$ is the probability density of the light mode at the edge of

the angular window. By setting boundary conditions at $\pm\pi$, we define the boundary $\theta = \pm\pi$ and $P(\theta) = P(\pi)$. This angular form of the uncertainty relation is notably different from the linear case as the right hand side of the inequality depends on the state under consideration. As with the linear case, there exist intelligent states of $\ell$ and $\phi$ such that the inequality is saturated, i.e. $\Delta\ell\Delta\phi = \frac{1}{2}|1 - 2\pi P(\pi)|$. The intelligent states for angle are Gaussian in form, truncated at $\phi = \pm\pi$, with a corresponding intelligent state in OAM which has an approximately Gaussian envelope.

For small values of $\Delta\phi$ (small angular transmission region), the probability $P(\pi)$ is small, and the relationship simplifies to $\Delta\ell\Delta\phi = 1/2$. However, for large values of $\Delta\phi$ (large angular transmission region), the value of the uncertainty product falls monotonically to zero. For a uniform angular distribution (no angular restriction), $P(\pi) = 1/2\pi$ and the uncertainty product becomes $\Delta\ell\Delta\phi = 0$. For no angular restriction, $\Delta\phi = \pi/\sqrt{3}$, which is the minimum uncertainty for an angular state[24]. It may appear unusual that the product of two conjugate variables can be equal to zero. However, this is a direct consequence of the cyclic nature of angle; the Fourier transform of a flat distribution in angular position is a delta function in OAM i.e. a pure OAM eigenstate. A distinction should be made between the *intelligent states* and the *minimum uncertainty states*[25]. For the position momentum case, the intelligent states which saturate the inequality are also the minimum uncertainty states. For the angular uncertainty relationship, they are in fact not the same, because the right hand side of the inequality depends on the

angular state. This angular uncertainty principle has recently been tested both at the single photon level, and between entangled pairs of photons[26].

## 1.4 Quantized Light

Evidence to support the quantization of electromagnetic radiation became apparent around the turn of the $20^{th}$ century. Experimental observation of the photo-electric effect[27], and consideration of the black-body spectrum[28] necessitated light to possess discrete quantization of energy. Compton demonstrated the first measurements of the momentum of photons through inelastic scattering with matter[29]. Light as a quantized property of the electromagnetic field can be derived semi-classically from Maxwell's equations. By bounding an electromagnetic wave in a 1-D cavity it acts as a simple harmonic oscillator. The energy states of this oscillator exists in discrete modes, which is the basis of the photon.

Moving further away from classical physics is the notion of a probability amplitude, as a physical interpretation of the quantum wavefunction. The existence of probability amplitudes gives rise to the principle of quantum superpositions, and it is consistent with observations of single-photon interference, as demonstrated with single photons interfering at a double slit[31], or passing through a Mach-Zender interferometer[32].

The qualitative derivation of a Fourier relation between variables can be modified to encompass quantized light. Equations (1.3) and (1.4) describe

the Fourier relation between variables $x$ and $k$, and $\Delta x \Delta k \geq 1/2$ is the uncertainty relation which arises from this Fourier relation. From quantum mechanics, momentum is expressed as $p = \hbar k$. Thus, the wavenumber distribution expressed in terms of linear momenta, $p$, becomes:

$$\psi(x) = \frac{1}{\sqrt{2\pi\hbar}} \int_{-\infty}^{\infty} A_p e^{ipx/\hbar} dp, \tag{1.11}$$

and therefore the uncertainty relation between $x$ and $p$ is,

$$\Delta x \Delta p \geq \frac{\hbar}{2}, \tag{1.12}$$

which is Heisenberg's Uncertainty relation between position and momentum[1].

### 1.4.1 Orbital Angular Momentum in Quantum Mechanics

It was shown theoretically in 1992 by Allen et al.[8] that photons can be described in terms of their OAM, as eigenmodes of the angular momentum operator $L_z$, and carry an OAM of $\ell\hbar$ per photon. It was also suggested that mode transformations between the LG and HG bases could occur using cylindrical lenses to invoke the appropriate phase transformation.

The first experiment to demonstrate that OAM is a property of single photons was that of Mair et al.[33] in 2001, where OAM measurements were

made holographically on pairs of down-converted photons. They demonstrated the quantum entanglement of OAM between the photons by showing that correlations persisted not only when measuring pure OAM states, but also for superpositions thereof. One year later, the same group went on to violate a Bell-type inequality for OAM states, an explicitly quantum mechanical result[34]. Since then there has been a great deal of interest in exploring the quantum properties of OAM states, including methods to quantify the degree of entanglement[35,36,37], how to access high-dimensional OAM state-spaces and the use of OAM in quantum information protocols (QIP)[38,39].

## 1.5 Quantum Entanglement

Many observed phenomena can be at least qualitatively understood using semi-classical theories or analogies. Quantum entanglement is an effect which can only be described using quantum mechanics. It is a *non-local* phenomenon, where separated systems have shared properties in such a way that does not obey classical mechanics.

### 1.5.1 The Einstein-Podolsky-Rosen (EPR) Paradox

*Note: The original EPR thought-experiment supposed measurements of spin states in a Stern-Gerlach type experiment. The thought experiment here utilises variables of position and momentum, which are equally valid, but contextually more relevant within this thesis.*

The EPR paradox[40] is a thought experiment (German: *Gedanken-experiment*) which supposed that quantum entanglement cannot be realized without physical contradiction, and thus, quantum mechanics as a theory is insufficient to describe the physical phenomenon under scrutiny. This paradox challenges the incompatibility of two of the largest contributions to 20th century physics; Quantum mechanics and the Theory of Relativity. In formulating the paradox, the authors make two fundamental assumptions about nature.

- Locality: That two sufficiently separated systems (or the wave functions describing two separated quantum states) do not interact with each other. This assumption relates to Einstein's theory of relativity.

- Reality: That, if a state can be predicted with certainty (without measurement), then it has a definite physical reality - suggesting that the state was determined at birth (and before measurement).

Their proposal supposed the existence of a state of two particles (A and B) that were perfectly correlated in both their positions ($x_A,\ x_B$) and momenta ($p_A,\ p_B$). In a real experiment one would measure the mean position or momentum with some experimental error, or variance, $\Delta x_{A,B}$ and $\Delta p_{A,B}$. However, in the thought experiment we have precise measurement systems. Therefore, measurement of the position or momentum of state A would then determine, instantaneously, the position or momentum of state B. By positioning the particles so that they could not interact, a measurement on one particle should not influence the wavefunction of the other. If this is strictly

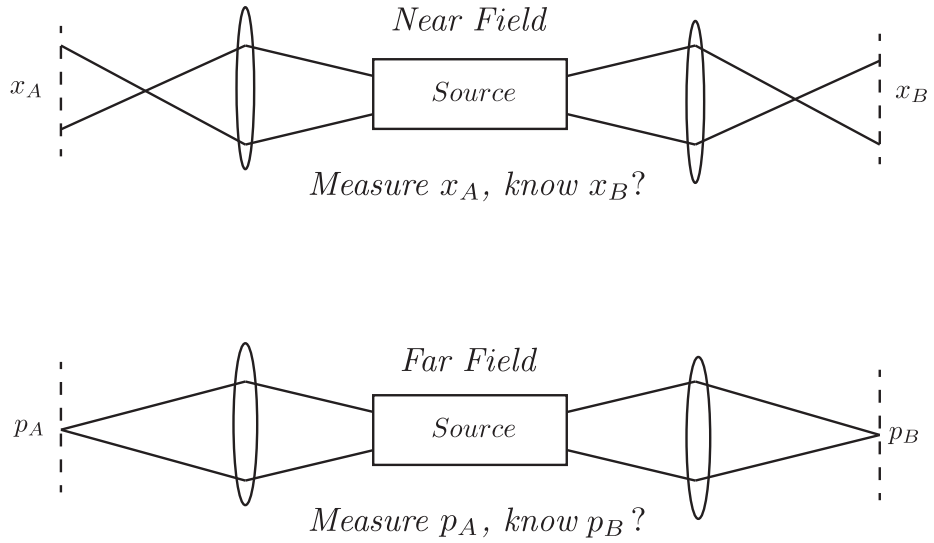


Figure 1.12: EPR paradox for variables of position and momentum. The source emits pairs of particles which are correlated in their position and momentum. Precise measurement of the position/momentum of A leads to precise knowledge of position/momentum of B. Both of these statements being true suggests a contradiction to Heisenberg's uncertainty relation.

true then it means that both the position and the momentum of the second particle must have been predetermined.

In this case, we have measured/inferred a state with $\Delta x_{A,B} = 0$ and $\Delta p_{A,B} = 0$ - in direct contradiction of Heisenberg's uncertainty relation. Quantum theory does not allow the simultaneous exact knowledge of two non-commuting observables, such as position and momentum and hence we have a paradox. The suggestion made by EPR to resolve the paradox was that quantum mechanics should be completed by some hidden variables to fully describe the state under investigation.

This then sets the challenge of how to quantify the statistics of quantum measurements: how does one identify the presence of hidden variables when they are, by definition, hidden from observation?

### 1.5.2 Bell's Inequalities - Polarization Entanglement

In 1964, John Bell published the derivation of a statistical limit of an inequality now known as Bell's inequality (modified versions of the inequality are commonly called Bell-type inequalities), with an upper bound which applies to specific measurements of systems exhibiting locality[41]. Bell's inequality therefore, would be violated for measurements in a non-local theory such as quantum entanglement. Bell considers pairs of measurements (as in EPR) correlated in a chosen property e.g. polarization. The original Bell inequality is

$$1 + C(\mathbf{b}, \mathbf{c}) \geq |C(\mathbf{a}, \mathbf{b}) - C(\mathbf{a}, \mathbf{c})| \tag{1.13}$$

where **a,b,c** correspond to different measurement settings (polarizer orientations) corresponding to polarization states **A,B,C** respectively and C is the expectation value of the product of the components (**B,C**),(**A,B**),(**A,C**). This inequality is statistically consistent with any classical correlations, such as those within local-realistic theories. Violation of this inequality would correspond to some non-local interaction between the states **A,B,C**.

This vector form of the inequality is not perfectly suited for experimental

conditions. There are a number of Bell-type inequalities, modified to be experimentally tractable.

The polarization variable is a suitable candidate for testing Bell's theorem. Polarization is easily accessible using polarizing filters, which yield a binary output for single photons (transmitted or not transmitted). Bell's theorem has been tested for sources of polarization entangled light, such as radiative cascade decay in atoms[42], and from parametric down conversion[43].

One can measure the coincidences between polarization entangled photons by placing polarizing filters at each detector. The coincidence rate will be a function of the relative angle between the polarizers, $\Delta\theta$ (depending on if the photons are correlated, anti-correlated or uncorrelated). For polarization - correlated photon pairs, one can fix the polarizer in one arm and rotate the other to observe how the coincidence rate varies as a function of $\Delta\phi$, Fig. 1.13. It is within these measurements that one can test whether or not, the act of measuring one photon non-locally sets the state of the other, i. e. if the photon pairs are entangled.

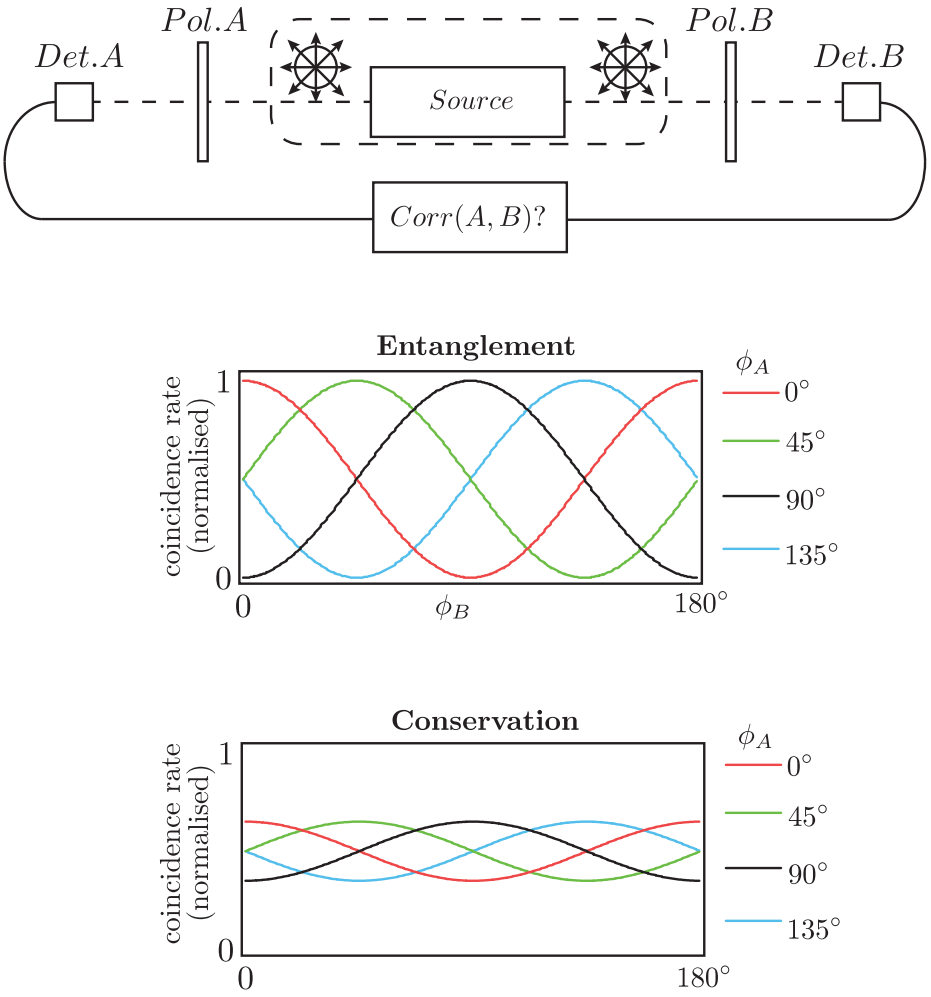


Figure 1.13: Schematic of a polarization entanglement experiment. Pairs of photons, correlated in their polarization, are emitted. If they are entangled, the act of measuring one photon polarization will set the other polarization, and correlations will occur as shown. If the polarization states are not entangled, but a well-defined property of the state before measurement, only conservation of spin will apply. The coincidence curve (bottom) is an example of one possible case where only conservation applies, manifesting in a reduced fringe contrast.

One example of a suitable inequality for experimental measurements of polarization is the Freedman inequality (Freedman and Clauser, 1972)[42], who performed the first of the experiments of Bell-type inequalities on entangled photon pairs. Freedman's inequality can be expressed as

$$\delta_p = \frac{|C_p(22.5^\circ) - C_p(67.5^\circ)|}{C_p(0)} - \frac{1}{2} \leq 0 \tag{1.14}$$

where $C(\phi)$ is the coincidence rate with a relative angle $\phi$, between polarizing filters in signal and idler arms, and $C(0)$ is the coincidence rate with both polarizers removed from the system. The relative angles of 22.5° and 67.5° degrees are where the differences between local and non-local statistics are most apparent, Fig. 1.14 (at relative angles of 0°, 45° and 90°, there is no distinction between local and non-local predictions).

A further modification of the Bell-type inequality is the Clauser-Horne-Shimony-Holt (CHSH) inequality[44]. This inequality has been violated in a number of historically significant experiments, the first of which was by Aspect et. al. in 1982[45]. In violating the CHSH inequality Aspect was able to exclude further types of local-hidden variable theories, thus favouring the quantum mechanics interpretation even more strongly.

The CHSH inequality places a statistical bound on local hidden variable theories with the parameter $S$, where

$$-2 \leq S \leq +2, \tag{1.15}$$

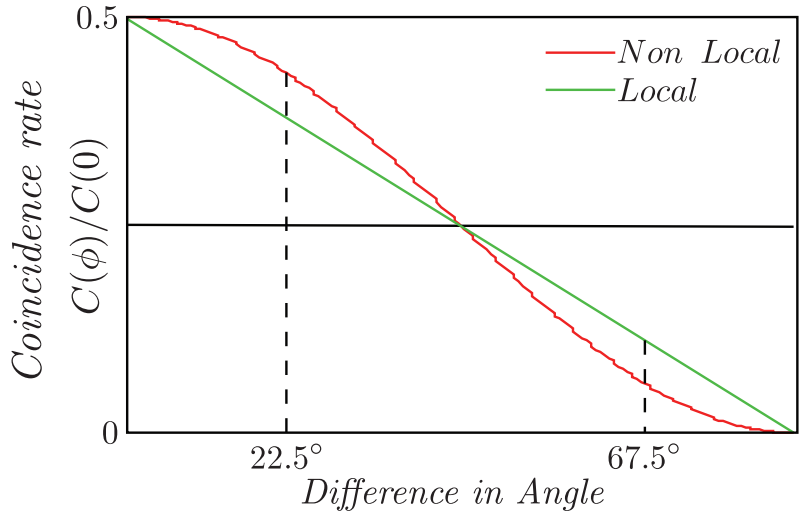


Figure 1.14: Local vs. non-local statistics as a function of relative polarizer angle to test the Freedman inequality. The deviation between local and non-local is greatest for a difference in polarizer angles of 22.5° and 67.5°. The coincidence rate is normalized with respect to $C(0)$ - the coincidence rate with both polarizers removed from the system.

with,

$$S = E(a,b) - E(a,b') + E(a',b) + E(a',b'), \tag{1.16}$$

where a,a',b,b' are measurement settings, in this case the orientation angles of polarizers in signal and idler beam paths. Each parameter $E(a^{(\prime)}, b^{(\prime)})$ is a different measured outcome from an experimental run. A schematic representation of the experiment is shown in Fig. 1.15, with detectors at each beamsplitter output designated + or −. The parameters E above are calculated as,

$$E = \frac{N_{++} + N_{--} - N_{+-} - N_{-+}}{N_{++} + N_{--} + N_{+-} + N_{-+}} \tag{1.17}$$

where $N_{\pm\pm}$ is the number of coincidence counts for a given output of the beamsplitters. By calculating S from these measurements, for a given set of polarizer angles, one can test whether or not the source produces non-local correlations . Again, the relative angles for which the statistics differ the most between local and non local correlations are 22.5° and 67.5°. A suitable set of polarizer angles to ensure this is $a = 0°$, $a' = 45°$, $b = 22.5°$ and $b' = 67.5°$. The upper bound for a local-hidden variable system is $|S| = 2$, and it can be shown that for a quantum entangled system the statistical bound is $S = 2\sqrt{2}$.

### Loopholes in Quantum Mechanics

Aspect's 1982 experiment differed from the previous experiments in that all possible outcomes were measured i. e. the output from both ports of the beamsplitters were recorded. This was significant because it excluded one of the so called *loopholes* in quantum mechanics measurements. That is, one could suggest that if only a subset of the entire state is measured (by only collecting the positive correlations), then the hidden variables could still be present, but masked by a statistical bias in measurement, suggesting that the illusion of non-locality would disappear by measuring all the possible outcomes. Aspect's experiment closed this loophole for polarization. However there exist many more loopholes, some of which have been closed, and

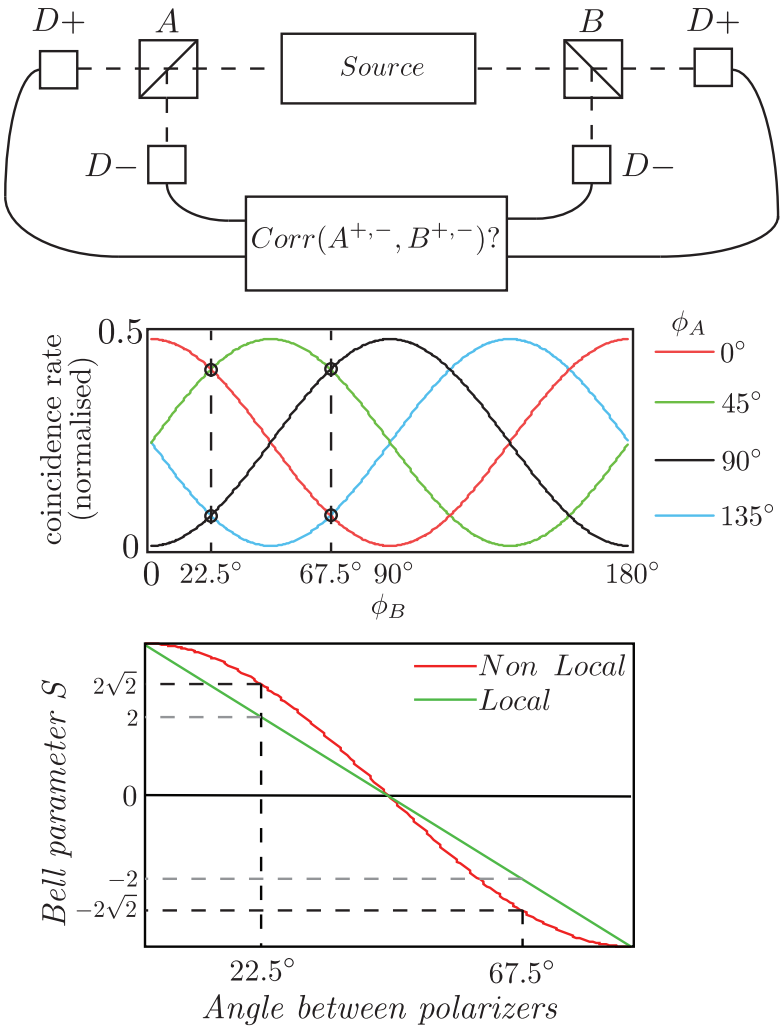


Figure 1.15: Aspect's improved "2 channel" Bell test experiment. Using polarizing beamsplitters, all possible measurement outcomes are observed, allowing for a stronger claim to non-locality over local hidden variable theories. Shown are the four measured coincidence curves for static polarizer angles, $\phi_A$. The black circles indicate the measurements which go into the CHSH inequality, where the Bell parameter S is most strongly violated.

some of which remain an experimental challenge. Many experimentalists accept quantum mechanics to be a suitable description for the observed phenomenon, as all experiments to date have been in favour of this. On the other hand, non-locality is such a fundamentally unintuitive phenomenon, that settling any challenges to quantum mechanics by closing the loopholes would be a very good idea!

These loopholes include but are in no way limited to;

- **The Fair Sampling loophole**: Closing this loophole places a lower limit on detection efficiency, and hence is a technological limitation. Most high efficiency detectors (such as semiconductor single photon avalanche diodes (SPAD) or photo multipliers) have a non-perfect detection efficiency, and any optical components will also contribute to loss. The suggestion is that by only measuring a fraction of the photons produced, there could be a statistical bias towards those which *appear* to be entangled, and the crucial information stored in the photons which are not registered, is lost. Optically, the quantum efficiency required to close the fair sampling loop hole is approximately $\eta = 0.8$[46,47].This loophole has been closed once using ions[48]. Because this is a technological difficulty for many experiments, the assumption of fair sampling is often made.

- **The Communication loophole**: The claim of quantum entanglement is that there is an instantaneous, non local effect between the

separated systems under observation. However if the two detectors are within the light cones of each other, then one cannot claim the effect is instantaneous. The detectors must be separated from each other at least $c\Delta t$, where c is the speed of light and $\Delta t$ is the timing resolution of the coincidence counting device. In general, most experiments do not close this loophole, as it can be inconvenient to separate the optical paths sufficiently. This loophole was perhaps most famously closed in the 144km path-length experiment between the islands of Tenerife and La Palma (although this was not the primary achievement of the experiment)[49].

- **Freedom of Choice loophole** This loophole suggests that the measurement device can in some way influence the outcome of the photons measured state. This loophole has been addressed for polarization by automating the polarizers to randomly choose a polarization state, timed such that this occurs after the photon pairs leave the source.

There are suggestions of novel ways to close these loopholes, for example making measurements in higher dimensional state spaces to violate a high-dimensional Bell inequality[50], in order to close the Fair Sampling loophole. It is thought that by exploring correlations in a higher dimensional state space, the required detection efficiency to close the Fair Sampling loophole falls. As an experimental challenge, the OAM variable seems to be a good candidate for addressing the Fair Sampling loophole, as it allows for correlations to be

measured in a potentially unbound state space.

## 1.6 Spontaneous Parametric Down Conversion

The nonlinear effects in certain crystals have been used widely within classical optics, to exploit phenomenon such as frequency doubling, optical parametric oscillation and spontaneous parametric down conversion[51]. These phenomena can occur when an input electric field interacts with the dielectric properties of the medium in a nonlinear way. SPDC is the process by which, an input electric field (pump) interacts with a nonlinear medium, resulting in two electric fields (signal and idler) whose combined energy is equal to that of the pump. These fields can be degenerate (same frequency) or non-degenerate, depending on certain conditions. In crystals, SPDC can be Type-I, where the down-converted photons have the same polarization, or Type-II, where they have orthogonal polarization.

It has only been in the past 20 years that SPDC has been shown to produce photon pairs known to be in an entangled state[43]. Since then, SPDC has become a popular method to produce entangled photon pairs. SPDC provides a relatively cheap, robust, and convenient (if inefficient) method of producing photon pairs.

Typically, the kinds of media used to produce down converted light are crystals found to have large nonlinear coefficients, such as BBO ($\beta\ BaB_2O_4$)

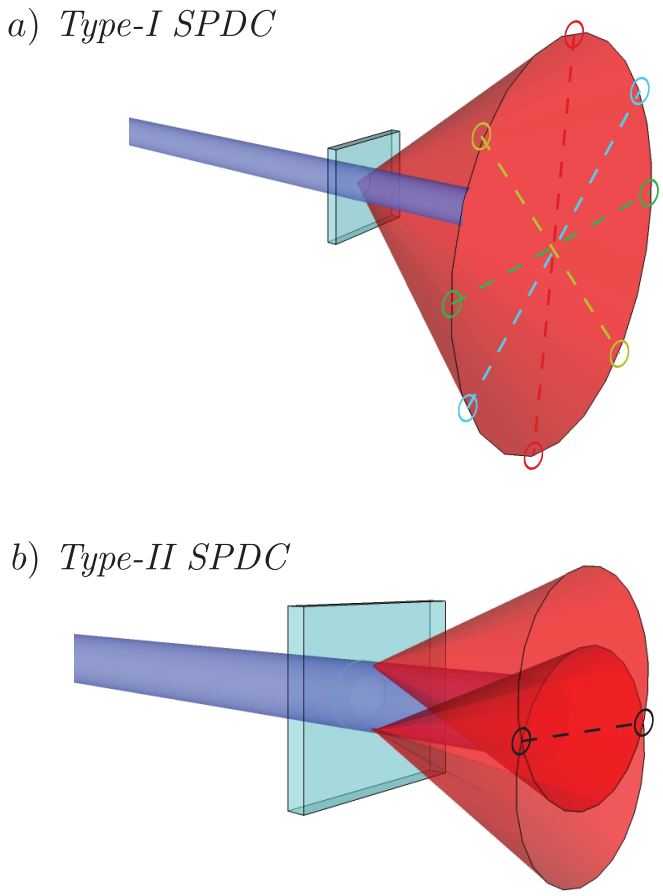


Figure 1.16: a) Type-I non-collinear down conversion. The emission cone angle is determined by the angle of the pump beam with the crystal axis. The entangled photon pairs in type-I are diametrically opposite as shown. b) Type-II down conversion. In a type-II crystal two cones (shown degenerate here) are produced. The entangled photon pairs are found in the region where both cones overlap.

or KTP ($KTiOPO_4$). The SPDC process is dependent on parameters such as the frequency and direction of the input light, which determines the possible

frequencies and momenta of the down-converted light, provided conservation of energy and momentum is satisfied. These selection rules are the phase matching conditions, Fig. 1.17. For BBO crystals, the phase matching is determined by the frequency of the pump, and the orientation angle of the crystal's optic axis with respect to the pump.

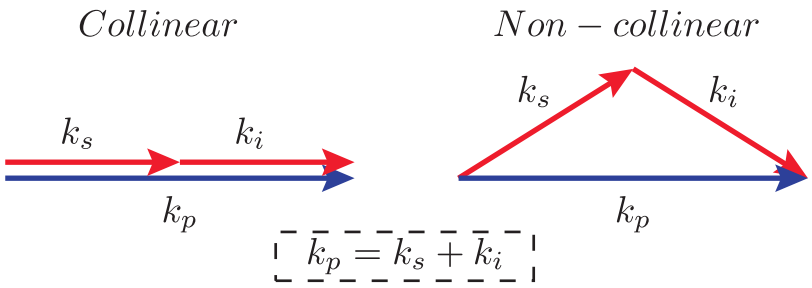


Figure 1.17: Phase matching conditions for wave vectors in collinear and non-collinear degenerate down-conversion.

In Type-I down conversion with non-collinear phase matching, the photon pairs are emitted with an angle between them and the direction of the pump beam. Crystal manufacturers cut non linear crystals to specification such that the phase matching is optimal for a certain angular separation between signal and idler. The down conversion process is ideally isotropic as a function of the azimuthal angle. This means the light is emitted in a cone, with the diametrically opposite photon pairs being the correlated with each other. For practical purposes, apertures are used to collect small portions of the ring which are on diametrically opposite regions of the cone.

In the 1980's, the Russian theoretician David Klyshko proposed a *retrod-*

*iction* interpretation[52] as a novel way to predict the outcome of experiments. In the retrodiction model, one treats the signal detector as a *source* of photons, propagated back through the system, to the crystal. These photons then see the crystal as a mirror, and propagate back to the idler detector. If a count is recorded at the idler detector in the unfolded system, then the prediction is the quantum system will measure a coincidence count. Of course, back-projecting from one detector to the other is not a quantum process (retrodiction considers an "advanced wave" instead of a two-photon wavefunction), but it does adequately predict the outcome of a given measurement. Shown in Fig. 1.18 is an example of a down conversion system, with it's unfolded counterpart. It is this retrodiction model which will be used to numerically simulate all of the experiments in this thesis.

In conjunction with the retrodiction model, one can also numerically predict the measured coincidences by calculating the overlap integral of signal, idler and pump fields[53]. It is calculated as the overlap between back-projected signal and idler modes with the pump mode at the crystal plane. The coincidence rate is proportional to the overlap intergal, i.e.

$$C \propto \frac{|\int \Psi_s^* \Psi_i^* \Psi_p \mathrm{d}A|^2}{\sqrt{\int |\Psi_s^* \Psi_p|^2 \mathrm{d}A \int |\Psi_i^* \Psi_p|^2 \mathrm{d}A}} \tag{1.18}$$

where $\psi_p$, $\psi_s$ and $\psi_i$ are the modes of the pump and back projected signal and idler respectively.

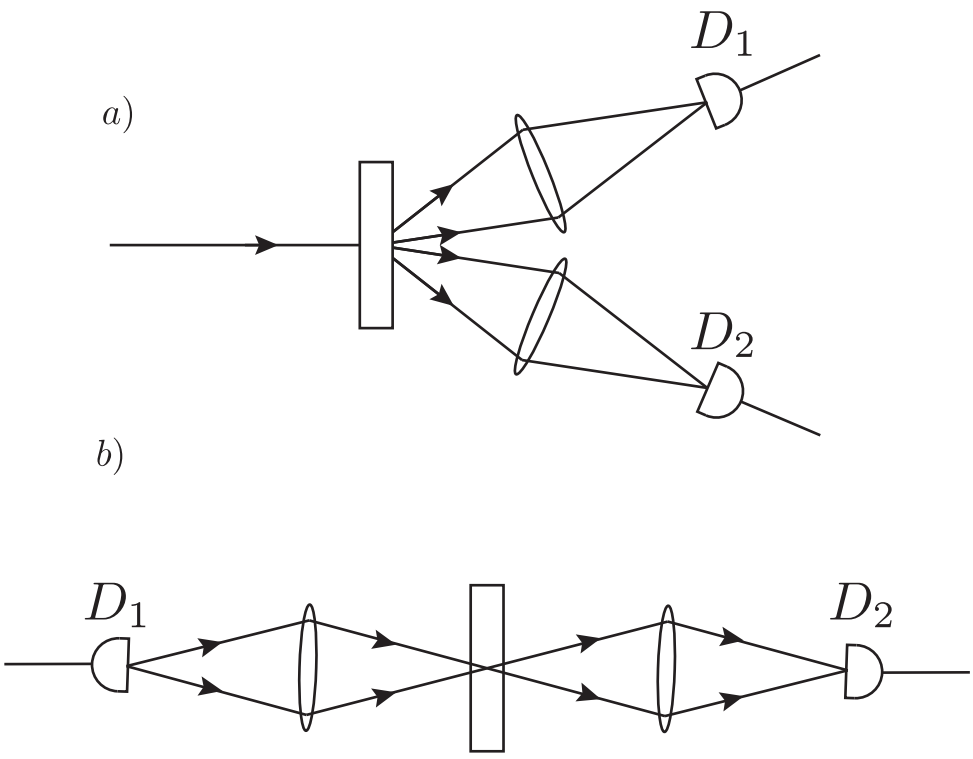


Figure 1.18: a) Schematic of a down-conversion system with detectors measuring in the far-field of the crystal. b) Unfolded retrodiction model of the same system. Retrodiction allows one to predict the outcome of a given measurement using classical optics.

### 1.6.1 Quantum Entanglement of OAM

The Austrian group of Zeilinger[33] were the first to demonstrate the non-separability of the OAM states of light, as a demonstration that OAM is an intrinsic property of single photons. The OAM states of light were measured holographically, by coupling the light into single mode fibers. By using holograms to convert a nonzero OAM state to the fundamental gaussian mode,

the group were able to measure the correlations between coherent OAM superpositions, demonstrating the non-local phenomenon of entanglement (the specific techniques used to measure OAM states of light are detailed in the experiment chapter, as they relate to experiments within this thesis). The photon pairs in this experiment were produced from SPDC, as it is a reliable method for producing photon pairs entangled over a broad range of OAM states.

In the same year, the Barcelona group of Torner developed a scheme to use entangled OAM states in a quantum communication protocol. Much in the same way that polarization can be used in quantum information protocols (QIP) with dimension 2[54], OAM can in theory be used to communicate quantum information, with dimension N - hence these high dimensional states are known as quNits[39].

Many recent experiments have been developed towards improving both the method of producing multi-dimensional sources of entangled photons, and the method by which operations are carried out on the photons, to improve the efficiency of generation, operation and detection. One of the advantages to using polarization in QIP is that, in principle, all possible states can be detected without loss - in theory, a polarizing beam splitter sorts modes of orthogonal polarization perfectly. Sorting OAM states with such fidelity continues to be a significant experimental challenge. In the past, proposals have been made for OAM mode sorting interferometrically with in principle, a high efficiency[55,56]. However, these mode sorters have experimental stability

issues, and distinguishing $2^N$ distinct OAM modes requires, at the very least $N$ interferometers (the experiment in[55] required $2^N - 1$ interferometers for sorting $2^N$ modes).

Holographic mode sorting by coupling light into a single mode fiber with off-axis spiral phased holograms does not sort OAM states in an efficient way. If the input light is in an ensemble of OAM states, the off axis hologram will only sort the OAM state with the opposite phase of the hologram phase, diffracting this mode into the +1 diffracted order (Fig. 1.19), however, this only allows one state to be measured at a time. There have been a number of novel methods proposed for more efficient methods to measure OAM states[57,58,59,60]. A recent proposed scheme is to use holographic methods to unwrap a $exp(i\ell\phi)$ from cylindrical to cartesian coordinates, such that each $\ell$ state is transformed to a different spatial coordinate in the far-field[61,62]. This scheme in principle can offer a high efficiency of mode conversion in a high dimensional OAM state space.

Another method to increase the dimensionality of the state space is to move from bi-partite to multi-partite entanglement. One scheme is the production of GHZ (Greenberger - Horne - Zeilinger) states[63,64], entangled states of 3 or more particles. Multi-partite entangled photon states can be produced, for example, by cascading second-order nonlinear crystals[65,66], or by exploiting interactions with third-order nonlinear media[67].

Remaining within bipartite entanglement systems, one can increase the information in an entangled photon pair by preparing photons entangled

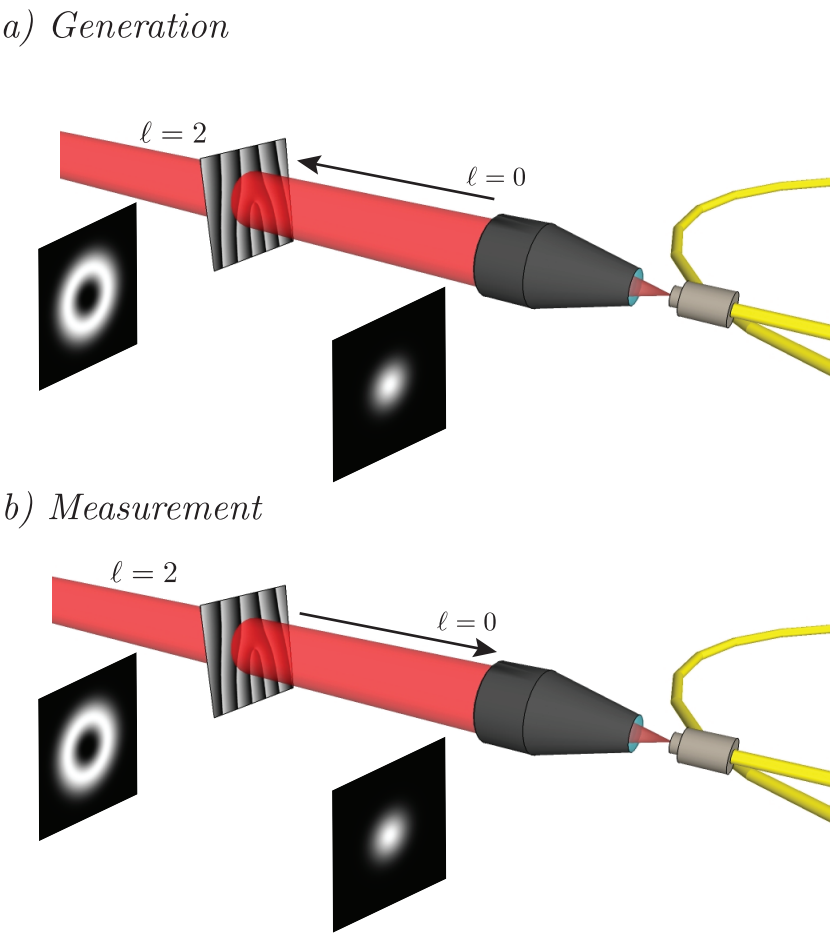


Figure 1.19: a) Generation of OAM. Light leaves the single mode fiber as a Gaussian beam ($\ell = 0$) and is converted by the hologram to $\ell = 2$. b) Detection of OAM. Light carrying OAM is converted by the hologram. If the phase of the hologram is opposite to that of the incoming light, it will be converted to $\ell = 0$ and subsequently detected.

in many degrees of freedom - known as *hyperentanglement*[68]. Preparing a state entangled in, say, both OAM and spin simultaneously, increases the dimensionality of the system as an alternative method to maximising the

dimensionality of the state space. The method to produce hyperentangled photon pairs was to use two adjacent non-linear crystals with orthogonal polarizations, such that there exists complete uncertainty over the birth place of the photon pairs[69]. This method produces a two-photon state entangled in OAM, spin, time and energy degrees of freedom. This was verified by making tomographic measurements of each parameter in turn to reconstruct a density matrix showing that the two-photon state produced was in 36-dimensional state space, vastly exceeding the 2-dimensional state space of polarization entanglement alone. A Bell-type inequality is then violated for each of the parameters, demonstrating the entangled nature of each parameter.

### Entangled States of Light Produced in SPDC

In Type-I down conversion, polarization entanglement is not observed, as the photons produced have the same polarization state. The spatial modes of the down converted light however, can be in an entangled state. Expressed purely in terms of the azimuthal phase index $\ell$, the entangled field produced in Type-I SPDC, $|\Psi_{SPDC}\rangle$, is given by,

$$|\Psi_{SPDC}\rangle = \sum_{\ell=-\infty}^{+\infty} c_\ell |\ell\rangle_s |-\ell\rangle_i, \tag{1.19}$$

provided the pump beam has a uniform phase distribution (i.e. $\ell_p = 0$). In the equation above, $\ell_s$ and $\ell_i$ are the azimuthal phase indices of signal and idler beams respectively, and $c_\ell$ is the probability amplitude of a state being

produced with a given $\ell_s$ and $\ell_i$ (and $|c_\ell|^2$ is the probability of such a state being produced). This process is symmetric, i.e. $c_\ell = c_{-\ell}$. The precise form of the probability distribution of the OAM spectrum produced in SPDC has been investigated theoretically and experimentally[70,71,72,73]. The probability amplitude for each mode $c_\ell$ is frequently constrained by experimental conditions, and tends towards zero for high values of $\ell$. Shown in Fig. 1.20 are examples of OAM mode spectra with different distributions of $c_\ell$.

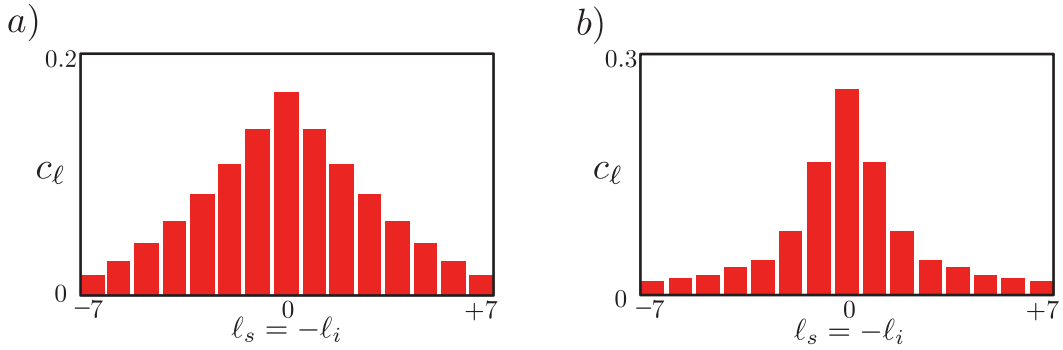


Figure 1.20: a),b) OAM spectra produced by SPDC for two different probability distributions $c_\ell$. The probability amplitudes are normalized such that $\sum |c_\ell|^2 = 1$.

For an entangled state with a given $c_\ell$, as above, one can then choose to explore the entirety of this space, or to measure within a dimensionally smaller subspace. While smaller state spaces do not utilize the full potential of the OAM spectrum, these 2-D state-spaces can be understood by analogy to the 2D state-space of polarization. An entangled OAM state in 2D can be written as

$$|\Psi^+\rangle = \frac{1}{\sqrt{2}}(|\ell\rangle_s|-\ell\rangle_i + |-\ell\rangle_s|\ell\rangle_i) \tag{1.20}$$

which is the OAM equivalent to one of the four Bell states for polarization.

### Quantum Entanglement of Angles

As an alternative to producing and measuring OAM states, preparing and measuring states within the complementary basis - angle - may offer advantages. By the Fourier relation, an angular distribution can be expressed as an infinite sum of OAM eigenstates. An angular measurement basis may provide an intuitive picture to realizing high-dimensional OAM superposition states.

Much in the same way that spiral phase plates can be used to generate/measure a single OAM mode, angular phase plates can be used to generate/measure states within a large OAM state-space. Entanglement between the angular states of light has been a recent subject of interest for the purpose of maximizing the dimensionality of the OAM space[74,75,38].

Using SLMs in signal and idler arms, it is possible for us to measure correlations between angular states, OAM states and complex superpositions of both. The programmability of our holograms means that we can cycle between holograms in an automated way. This automation allows for novel uses of SLMs within a down-conversion system, such as algorithms designed to automatically align the experiment, and to quickly replace holograms without

the need for re-alignment, as necessitated by phase plates. These techniques, and others, are detailed in the following chapter.

CHAPTER

# TWO

# EXPERIMENTAL METHODS AND APPARATUS

The majority of the work presented in this chapter involves measuring the OAM of photon pairs produced in SPDC, including the detail of experimental techniques and equipment (both software and hardware) required to build a down-conversion system, and how the SLMs are used to perform holographic measurements. Over the course of the experiments carried out on this system - as necessity and to improve understanding - there have been multiple imaging configurations. Fundamentally these can be separated into two categories; where measurements are made in the near-field (image plane) of the crystal, and where they are made in the far-field (Fourier plane).

## 2.1 Type I Parametric Down Conversion with a BBO crystal

The down converted light is produced by optically pumping a BBO crystal with ultra-violet laser light. The laser (Xcyte) is a diode-pumped, solid state (DPSS) laser, mode-locked at 355nm with an average power of 150mW, and is a pulsed with a repetition rate of 100MHz. It is a turn-key system, and the average power remains stable over very long periods of time, which makes it an ideal choice for use in low light level conditions, where data may be collected over long periods of time.

Both collinear and non-collinear phase matching conditions have been used to perform experiments, with SLMs placed in both the image plane and the Fourier plane of the source.

### 2.1.1 Non-Collinear Configuration

In the non-collinear configuration, the down converted photon pairs exit the crystal with an angle between them determined by the orientation of the crystal. The crystal used here is cut for a half angle of 8 degrees when phase matched.

The laser source is plane incident on the crystal, which is mounted on a rotation stage and goniometer. By adjusting the angle of the crystal with respect to the incident laser beam, we determine the correct phase matching angle by imaging the down converted light onto an intensified CCD camera

(Fig. 2.1).

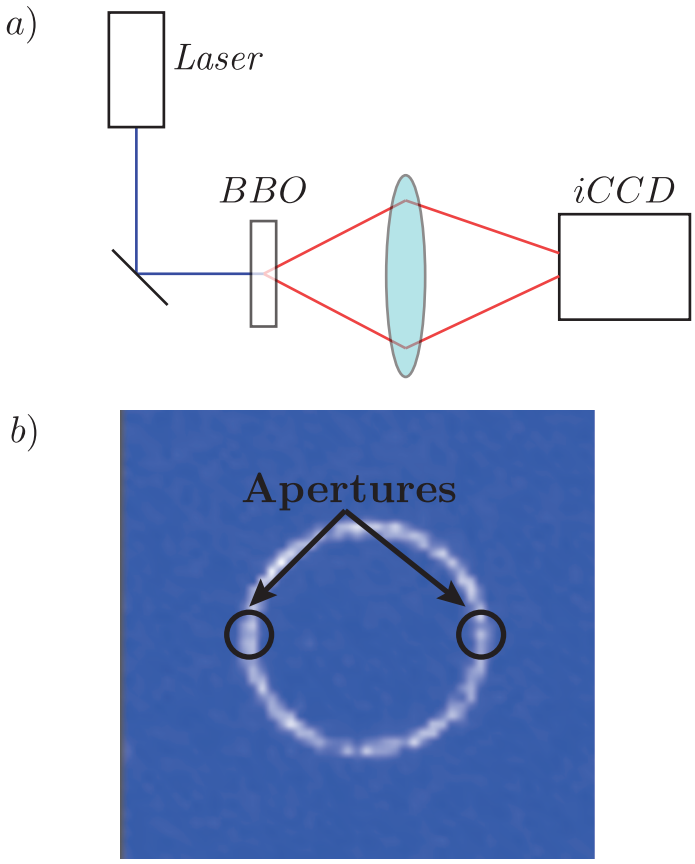


Figure 2.1: a) Experimental setup to image down-converted light. The intensified CCD camera is imaging the far-field of the crystal. b) Resulting image of the down-converted light.

For alignment purposes, is experimentally convenient to only select the photon pairs which are produced parallel to the laboratory bench, which is achieved by adding adjustable apertures into the system (illustrated in Fig. 2.1). Using the CCD camera to image the apertures, we can verify that the desired light is propagating through the system. This light can then be

coupled into optical fiber, where the count rates and coincidence rates are measured.

Single mode optical fibers are used to discriminate between different spatial modes. However, large aperture fibers can be used for alignment purposes, as a means to collect more light and reduce the alignment sensitivity.

Lenses are used to re-image the light from the crystal to different planes. Immediately after the crystal, large aperture lenses are desired in order to collect as much light as possible from the source. A short focal length lens is required to efficiently couple light into the fibers.

### 2.1.2 Collinear Configuration

The other mode of operation is where the down converted light is collinear phase matched. A different BBO crystal cut for collinear phase matching is used for this. The significant difference in this configuration is that the co-propagating signal and idler beams have to be separated by a beam-splitter. This means that the number of measured coincidences will be reduced by a factor of 2 i. e. there are four possible ways the two photons can leave the beamsplitter, and only two of those outcomes result in one photon in each arm. However, contrary to non-collinear down conversion where a fraction of the ring is collected, all of the collinear down converted light is localised to a spot, meaning less light is being discarded.

Additional to detection efficiency, there are further advantages and disadvantages to both colinear and non-colinear configurations. One of which has

already been discussed, which is the potential of loss of signal in each configuration. A further consideration in each case is the spatial distribution of the light which is imaged to the detector. In the collinear geometry, the signal and idler beams co-propagate. This means that, for example, projected measurements of linear or angular position will be rotationally symmetric, i.e. the overlap between the back projected positional (or angular) distribution does not depend on the chosen starting angle. For the non-collinear geometry, this is not the case. Because an apertured section of the ring is collected, the distribution of light has a "long" and "short" axis, so that any measurements of position will depend strongly on the chosen starting angle, as the overlap varies as a function of angle, Fig. 2.2.

### 2.1.3 Spiral Bandwidth

An important consideration in measuring the OAM states produced in SPDC is in understanding how to influence the number of modes being either generated or measured. The width of the distribution of OAM modes present in a system is called the Spiral Bandwidth,[70] and has a number of experimental dependencies. In addition to the number of modes produced in SPDC, the optical configuration can also have an effect of the number of modes observable. For example, an aperture restriction within the experiment would place an upper limit on the number of modes measurable, for example the numerical aperture of fibers, or the physical aperture of lenses present in the system will determine the range of measurable OAM states. The spiral bandwidth

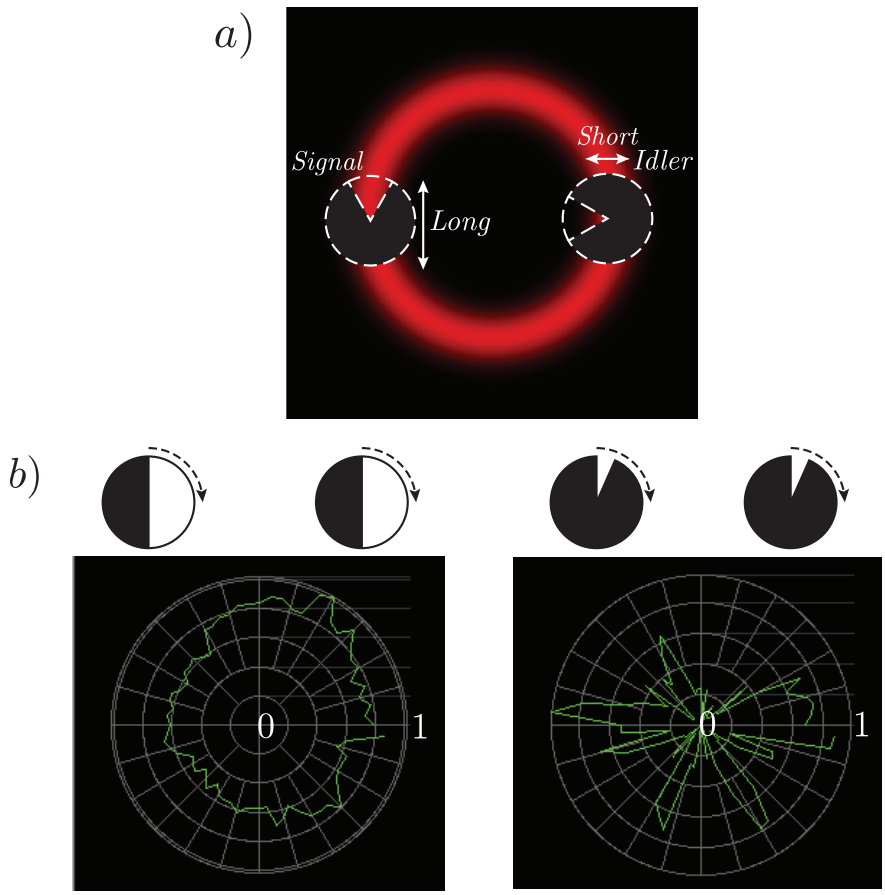


Figure 2.2: a) "Short" and "Long" axes of angular distributions measured in non-collinear down conversion. In this case where an angular state is measured, the overlap of signal and idler modes depends on the absolute orientation of the mask, as well as the relative angle between the signal and idler states. b) Measured coincidence rates (polar coordinates) as a function of starting angle of amplitude masks. In each case the masks are rotated through 360° with the same relative angle between them. The signature of asymmetry due to the down conversion ring becomes highly apparent for small angles.

of a system can therefore be separated into a "generation bandwidth" and a "measurement bandwidth", each dependant on separate parameters.

### Generation Bandwidth

For BBO crystals, the number of modes produced depends primarily on two parameters. Firstly, the thickness of the non-linear crystal (relative to the Rayleigh range of the pump) will partly determine the phase matching bandwidth, and thus the transverse momentum bandwidth. By making the crystal thicker, one makes the phase matching conditions more restrictive, and reduces the probability of higher order OAM eigenstates produced in signal and idler photons. A thinner crystal will result in a greater number of OAM modes produced. One must also consider that there is a trade off between number of modes produced, and photon count rates for each of those modes. Re-distributing a finite photon flux over a very large number of OAM states will result in a very low count rate for each OAM mode measured - a potential experimental problem.

The second parameter we will consider which has an effect on the generation bandwidth is the beam waist of the pump. A small pump beam waist will result in few OAM modes being produced in the crystal. The extreme case where the light is focused to a point; in this case, the down converted state produced can only be $\ell_s = \ell_i = 0$, and no entanglement is present. By increasing the beam waist, one increases the probability of a higher order mode being produced. As light modes with a phase profile $exp(i\ell\phi)$ have a

radial intensity distribution which is proportional to $\sqrt{\ell}$ (for p=0)[7], the size of the pump beam sets an upper limit on $\ell_s$ and $\ell_i$.

### Detection Bandwidth

The detection bandwidth is primarily limited by the imaging system used, and can be calculated from the overlap between pump and back-projected signal and idler modes at the crystal. For a given size of pump beam, there is a trade-off between the overlap between a given signal and idler mode, and the range of modes over which the overlap is non-zero. For example, a back projected $\ell_s = \ell_i = 0$ mode which is the same size as the pump beam will have a strong overlap for $\ell = 0$, but very little overlap for any higher order modes (because the radius increases with $\ell$). On the other hand, a very small back projected $\ell_s = \ell_i = 0$ mode will have far less overlap with the pump beam, but there will be a non-zero overlap for a much larger range of modes.

It is essential to have the appropriate imaging conditions in order to achieve a given experimental outcome, whether the requirement is for a large range of measurable OAM states, or a high photon count rate over a smaller range of OAM states.

## 2.2 Measuring Photon Count Rates and Coincidences

It is important to be able to record both the single channel events in signal and idler arms, and the coincidence events, with a high accuracy. This becomes especially important in situations where photon count rates are very low, as noise may dominate the signal. There can be multiple contributions to noise in a coincidence counting system. For example, background light in the laboratory space can leak into the detector modules, and result in increased background count rate. In single photon counting modules, there are several characteristics which will affect the accuracy of measurements,

- **Dark count rate**: Every photon counting module will register some events even when there is no light present. This can be due to thermal effects on the active area of the detector. More modern devices offer reduced dark count rates, and cooled photon counters also offer lower dark count rates.

- **Quantum Efficiency**: The quantum efficiency is the ratio of photons detected to photons incident on the detector. Typically, off-the-shelf detectors will have a range of wavelengths over which they are usable, but with a peak efficiency around a specific wavelength somewhere in the visible spectrum. Solid state detectors can be customized for peak efficiency at certain wavelengths, determined by parameters such as the

doping material used and absorption layers within the diode.[76]

- **Timing Jitter**: The timing jitter of a detector is the uncertainty in time of an event occurring. This can be tested by illuminating the detector with a periodic source with very low jitter. A histogram of recorded events within the period window can be recorded, and the FWHM of this distribution is the jitter of the detector (provided the source has negligible jitter). In many experiments where timing is crucial, such as in LIDAR, it is important to have as little timing jitter on the detection as possible[77,78].

In measuring the coincidences between detection events in each detector, sufficiently fast electronics are required to ensure that the correct events are registered as a coincidence, as opposed to uncorrelated events. Two different systems have been used to measure coincidences. In the first instance, the outputs from each detector were connected to a multi-channel interface (National Instruments PCI-6602), which was used to measure the single channel outputs of both detectors, and the coincidences between each channel. This device measures coincidences using a "start-stop" system - where the first detector event initalizes the second channel. When the leading edge of the pulse arrives on the second channel, a coincidence count is recorded.

The size of the coincidence detection window (set by the speed of the electronics), is $25ns$. This means that, after the first detection event, if an event is recorded from the second detector within $25ns$, a coincidence is

registered. Because of this finite coincidence detection window, coincidence events may be registered between uncorrelated photons, known as *accidental* coincidences, or accidentals. The accidental coincidence rate for two single channel count rates, $S_1$ and $S_2$ and a gate time $\Delta t$ is given by,

$$R_{acc} = S_1 S_2 \Delta t \tag{2.1}$$

A useful number to define the strength of the observed coincidence rate above the accidental rate is the *quantum contrast*. The quantum contrast is a normalized coincidence rate, and is defined as

$$Q.C. = \frac{C}{S_1 S_2 \Delta t}, \tag{2.2}$$

where $C$ is the coincidence rate for single channel rates $S_1$, $S_2$. This normalized coincidence rate is perhaps a more accurate indicator of the strength of the measured coincidences i.e. if all measured coincidences are accidental, the quantum contrast will be 1. Increasing the quantum contrast of a given measurement corresponds to improving the signal to noise ratio, either by increasing the true coincidence rate, or decreasing the accidental coincidence rate.

One way to improve the quantum contrast overall is to decrease the coincidence detection window, $\Delta t$. As an alternative to the NI-6602, we use a time-amplitude converter (TAC) for measuring the coincidences between the detection events. This device is an Ortec TAC-566. Similarly, the TAC uses

one detector as a starting trigger, and the other as a stop trigger. However, the time window is set by the voltage readout of the TAC. This device operates with a gate time of $10ns$, reducing the accidental coincidence rate by a factor of 2.5.

### 2.2.1 Single Photon Counting Modules

Two different types of photon counters have been used for the experiments in this thesis. Firstly, a pair photo-multiplier tubes (PMT) were used. After the first experiment, these were replaced with avalanche photo-diodes(APD). The detectors were replaced as the APDs have a higher quantum efficiency than the PMTs at the desired wavelength (710nm).

#### Hamamatsu PMT (Photo-multiplier tube)

The PMT's used were Hamamatsu H7421-50. The major advantage to these detectors is that they are inexpensive single photon counting devices, which exhibit a wide wavelength response. This model of PMT is shown below, along with the measured performance characteristics, Fig. 2.3.

Because of the large active area of the photocathode ($5mm^2$), care had to be taken to isolate these devices from all external light. The background count rate (dark count rate included) of these devices was measured to be approximately 800 $sec^{-1}$. This background count rate was measured after all efforts were made to isolate the detectors from background light, and is somewhat higher than would have previously been anticipated. These devices

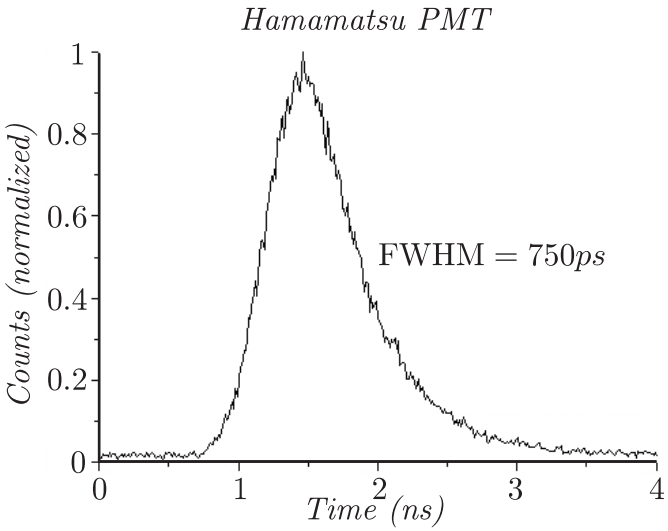


Figure 2.3: Hamamatsu PMT initially used for photon counting. The graph shows the performance characteristics of the device. The timing jitter of the device (FWHM) is 750ps. The large active area of the detector is indicated by the presence of the noise floor.

have an operating quantum efficiency which is estimated to be around 8-10%. In conditions with sufficiently high photon flux, these detectors function well. However, in extreme low-light situations, the low quantum efficiency becomes a problem. It is worth noting that current off-the-shelf PMTs have a much improved quantum efficiency and dark count rate than the ones used here.

**PerkinElmer APD (Avalanche Photo-diode)**

The second type of detectors used on this experiment were the PerkinElmer (SPCM-14) avalanche photo-diodes. These - more modern - devices have much improved performance characteristics compared to the model of PMTs used. They operate with a quantum efficiency at 710nm of approximately 60%, with a background count rate of around 200 $sec^{-1}$ because our laboratory environment is not completely dark (the rated dark count rate is approximately 20 $sec^{-1}$). The characteristics of the APDs is shown in Fig. 2.4.

The PMTs and the APDs interface simply with both the NI and the Ortec coincidence counting devices.

## 2.3 Spatial Light Modulator

As an alternative to using phase plates, one may use an SLM. Because of the anticipated difficulties of aligning a single photon experiment, having a reprogrammable phase element in the system removes the need to frequently replace optical elements - once a displayed hologram is aligned with respect

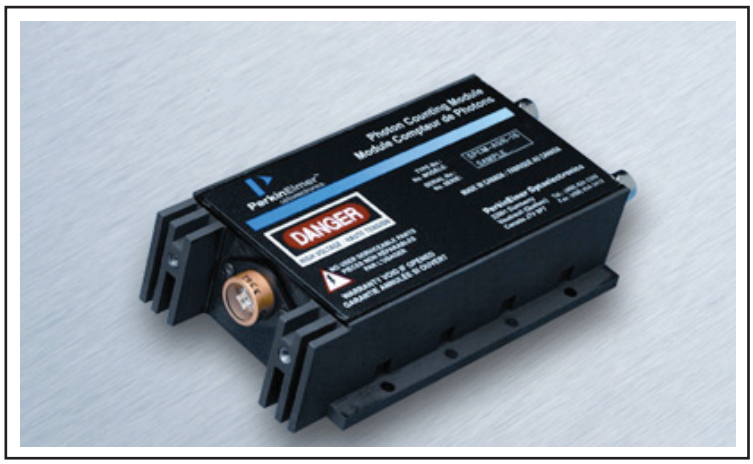


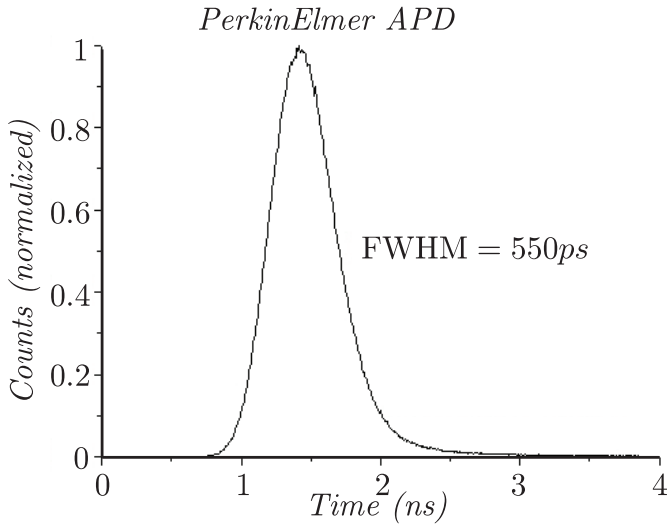


Figure 2.4: PerkinElmer SPCM-14 avalanche photo-diode. These devices are more robust, have reduced noise and reduced jitter compared to the PMTs.

to the beam, it's phase distribution can be changed without misalignment. This is a compelling reason to use SLMs, as opposed to phase plates in a

down-conversion system.

The versatility of SLMs has been well established. Their use has been demonstrated as spiral phase zone holograms[79], as beam steering devices in holographic optical tweezers[80,81], for generating complex functions such as Bessel and Laguerre-Gaussian functions[82,83], and for producing complex 3-dimensional distributions of light[84,85].

Using a spiral phase plane to convert the OAM state of a light beam is a highly efficient process; all of the light passing through the phase plate exhibits a phase retardation due to the refractive index of the material used. Representing a spiral phased hologram on an SLM is less efficient. Conventional SLMs work in reflection, so some loss can be attributed to absorption by the liquid crystal, and reflection by the glass covering the LCD (this effect is significant without wavelength-specific anti-reflection coating). In addition, a non-unity fill factor (due to space between pixels) also results in loss. For these reasons, the light directly reflected from a hologram displayed on an SLM will result in a mixture of the desired hologram phase, and light which has the same phase as the input light field. Due to the inherent inefficiencies of SLMs, there will always be a significant unmodulated component to any light directly reflected off the SLM.

In 1991, Heckenberg et. al. demonstrated that by adding the phase of a Fresnel lens modulo $2\pi$ to a given phase distribution, the light which is at the focal plane will contain precisely the phase specified by the hologram[79] and the unmodulated light remains unfocussed. In a similar way, by adding

a blazed linear grating modulo $2\pi$ to a given phase distribution, the desired phase information is found in the first diffracted order. This method of using a blazed diffraction grating to shift the modulated light to the first diffracted order will be the method we employ. By adding a blazed grating modulo $2\pi$ to a spiral phase, we obtain a "forked" hologram,[86] where the fork dislocation indicates the phase singularity, and the number of "prongs" indicates the charge $\ell$ of the hologram. Shown in Fig. 2.5 are example grayscale holograms for spiral phase masks of different charge, and the same holograms modulated by a blazed grating, to produce the desired light field in the first order.

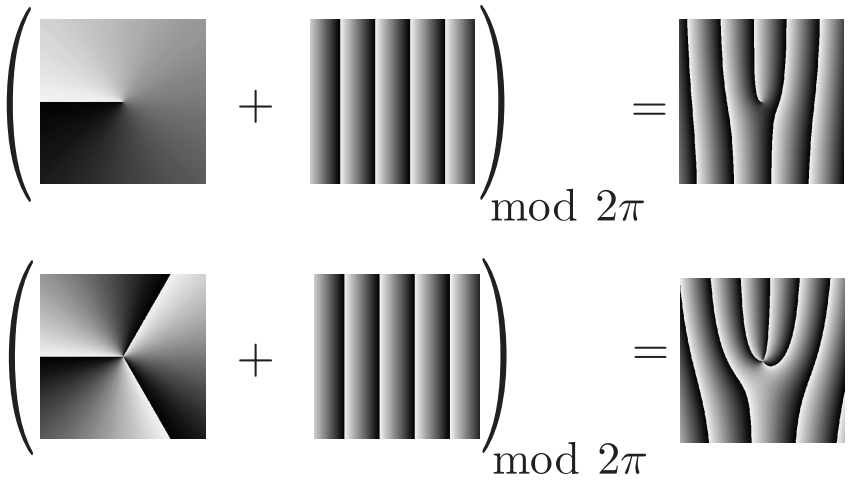


Figure 2.5: Examples of modulo $2\pi$ addition of a blazed diffraction grating with spiral phase of $\ell = 1$ (top) and $\ell = 3$ (bottom). These forked holograms result in a first diffracted order light mode with phase corresponding precisely to $\ell = 1$ and $\ell = 3$ respectively.

The SLMs we use are *phase only* modulators. However, they can also

be used to shape the intensity of a light field. Modulating the intensity of the light has been demonstrated previously as a method of producing light modes with precise spatial intensity distributions, such as the LG and HG modes. This is achieved by multiplying the phase hologram with an intensity distribution corresponding to the desired intensity in the first order, given by

$$\Phi(x,y)_{\text{holo}} = \left[\left(\Phi(x,y)_{\text{beam}} \ + \ \Phi(x,y)_{\text{grating}}\right)\right]_{\text{mod}2\pi} \text{sinc}^2\left[(1 - I(x,y)\pi)\right], \tag{2.3}$$

where $\Phi(x,y)_{\text{beam}}$ is the desired phase distribution, $\Phi(x,y)_{\text{grating}}$ is the phase distribution of the blazed diffraction grating, and $I(x,y)$ is the desired intensity distribution. The $sinc^2$ term accounts for the mapping of the phase depth to the diffraction efficiency of the spatially dependent blazing function.

### 2.3.1 SLM Characteristics

As we will be using the SLM to act as an off-axis hologram (to couple light from the first diffracted order into a single mode fiber), the primary concern is the diffraction efficiency. This is related to several properties of the device, such as the anti-reflection coating for the correct wavelength, the fill factor of the pixels (the ratio of the inter-pixel area to the active area) and the ability to fully modulate the phase over the full $2\pi$ range. Many SLMs offer fast update rates (100 Hz or higher), which is very important for, say, adaptive

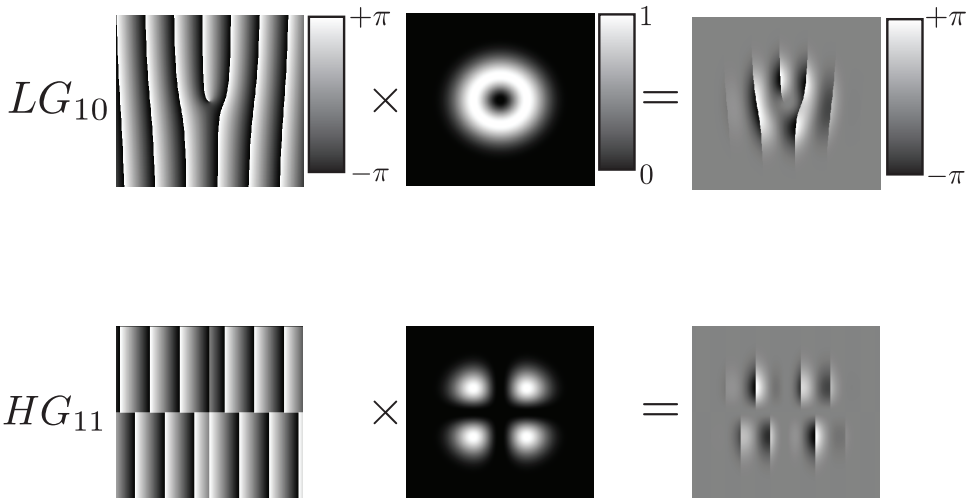


Figure 2.6: Phase holograms multiplied with the appropriate intensity modulation for a specific mode. As a result of the intensity modulation, a constant phase region in the hologram results in a null of intensity in the first diffracted order. This masking can be applied to the Laguerre-Gauss modes (top), and the Hermite-Gauss (bottom), or indeed any spatial mode.

optics or in holographic optical tweezers, where conditions change at a high frequency. However, any single photon experiment will involve collection of data for at least several seconds, if not minutes. Therefore, the speed of the phase modulator is not a primary concern. A final consideration is that the SLM window should be as close to phase flat as possible. This is generally the case for all modern SLMs, and any residual aberrations can be compensated for with an aberration correction hologram.

We use a Hamamatsu LCOS (Liquid crystal on silicon) SLM, Fig. 2.8. This SLM is electrically addressed and operates by the nematic liquid crystal

effect on the phase of the input light.

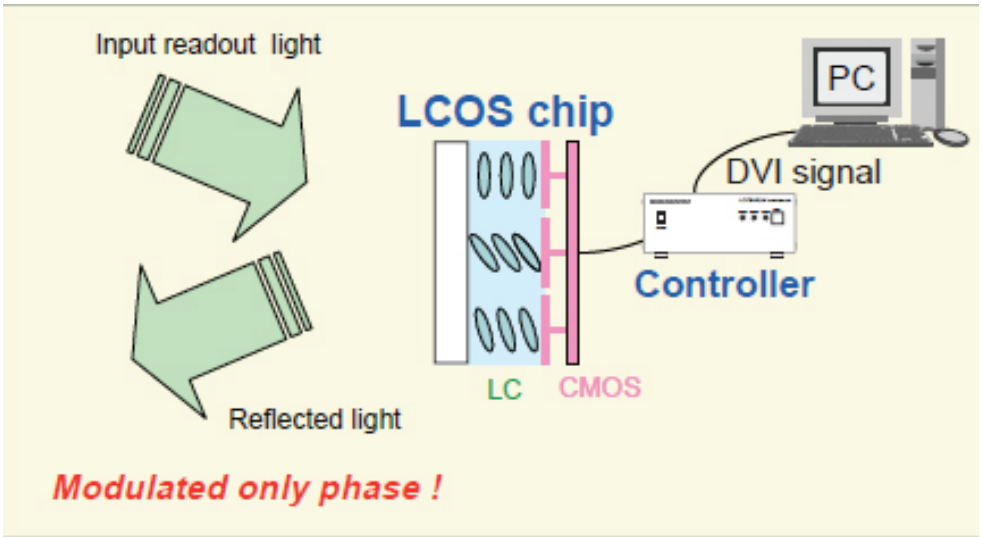


Figure 2.7: Schematic of LCOS operation (from Hamamatsu website)

The phase modulation range 0-2$\pi$ is set in 256 discrete voltage steps per pixel (represented as a grayscale 0-255). Shown in Fig. 2.9 are the measured count rates in the first diffracted order as a function of the phase contrast of the SLM. If the SLM had perfect grayscale to phase response over the entire 0-2$\pi$ range, then the count rates should vary linearly as a function of the phase modulation. As can be seen, the response is approximately linear except at the extremities close to pixel values of 0 and 255. This characteristic response is unique to each SLM, and this response can be used as a correction curve with which to compensate for the inaccuracies in pixel value to phase modulation. Once this correction is implemented, we can assume that the

phase modulation given to the light is correct.

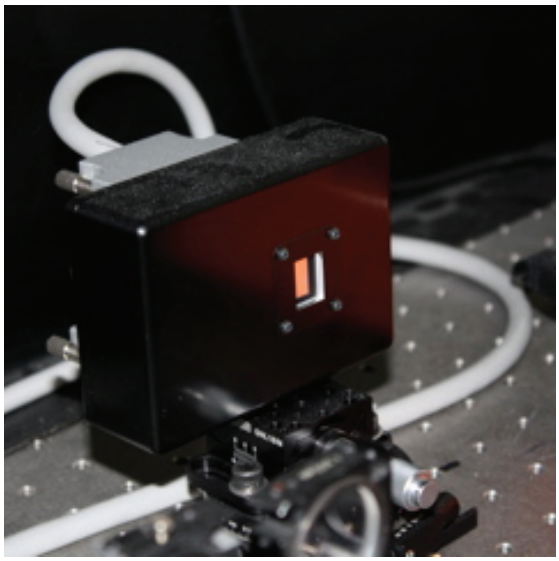

Figure 2.8: Hamamatsu LCOS electrically addressed SLM. These are placed in each arm of the down conversion experiment.

## 2.4 Building a System to Prepare and Measure Entangled Photon Pairs

The necessary components required to make holographic measurements of OAM states in SPDC are; a pump laser, BBO crystal, SLMs in signal and idler arms, single mode fibers and photon counting modules. The SLMs can be in one of two imaging planes - either in the far field or near field of the crystal.

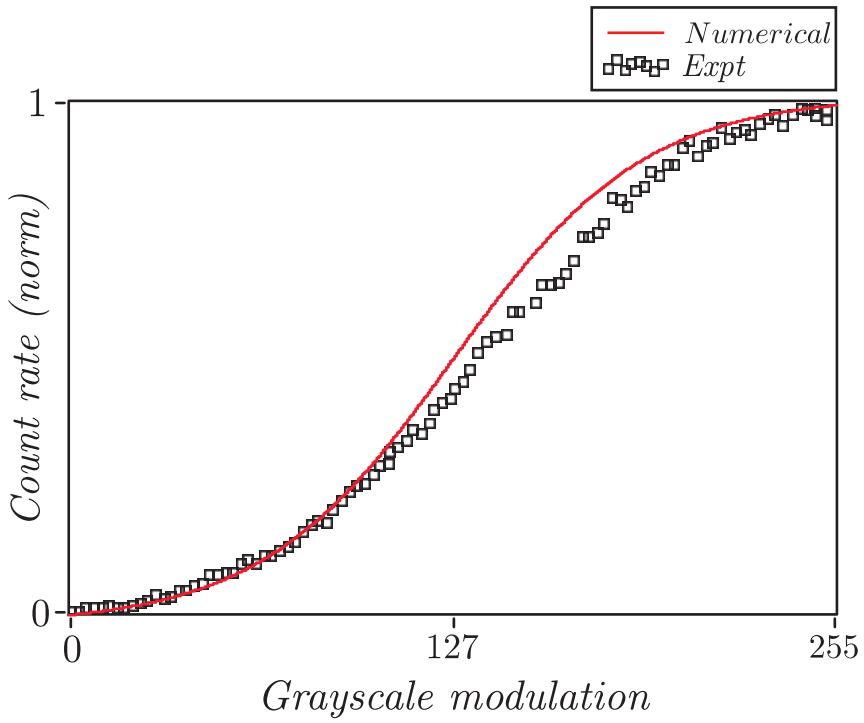


Figure 2.9: Calibration curve of measured count rates in the first order,as a function of the grayscale contrast of a blazed grating hologram. This curve is used as a correction lookup table, to ensure the expected relationship between pixel value and phase.

A far-field measurement system is where the SLMs are in the Fourier plane of the crystal. In Fig. 2.10 the SLMs are in the approximate far-field of the crystal. A near-field measurement system is where the SLMs and detectors are in the image plane of the crystal, Fig. 2.11. In this case, the back-projected light from the detectors is imaged to the SLMs, which is subsequently imaged to a spot at the crystal.

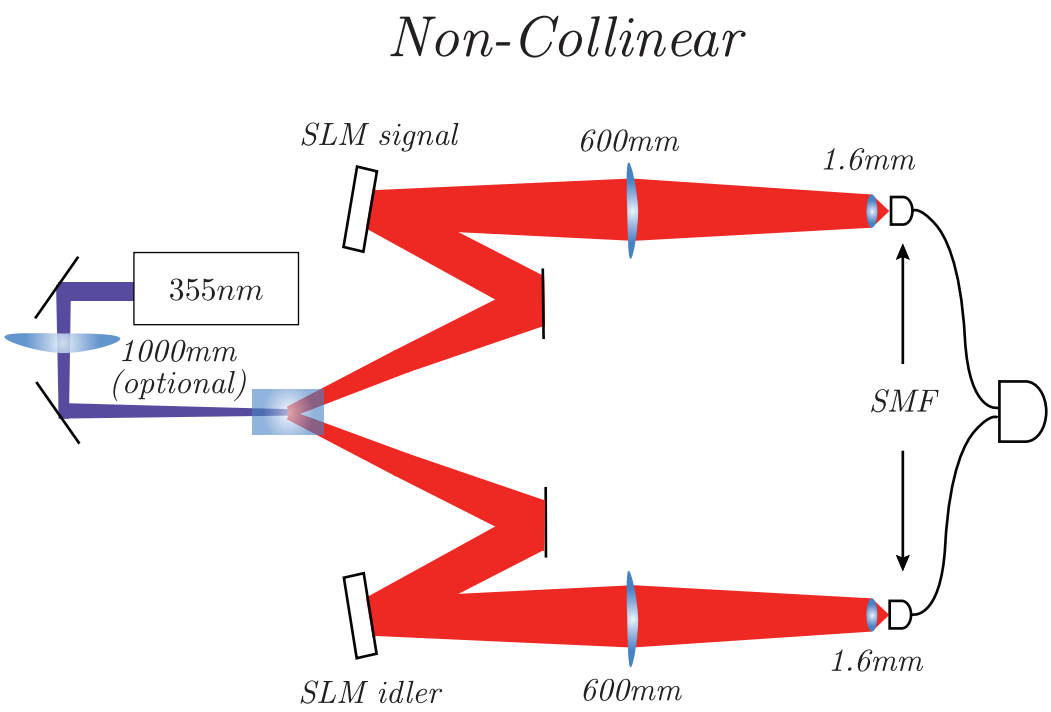


Figure 2.10: Experimental setup where measurements are made in the approximate Fourier plane of the crystal. The optional 1m focal length lens in the pump beam results in an increased pair production rate, but at a cost of reduced spiral bandwidth.

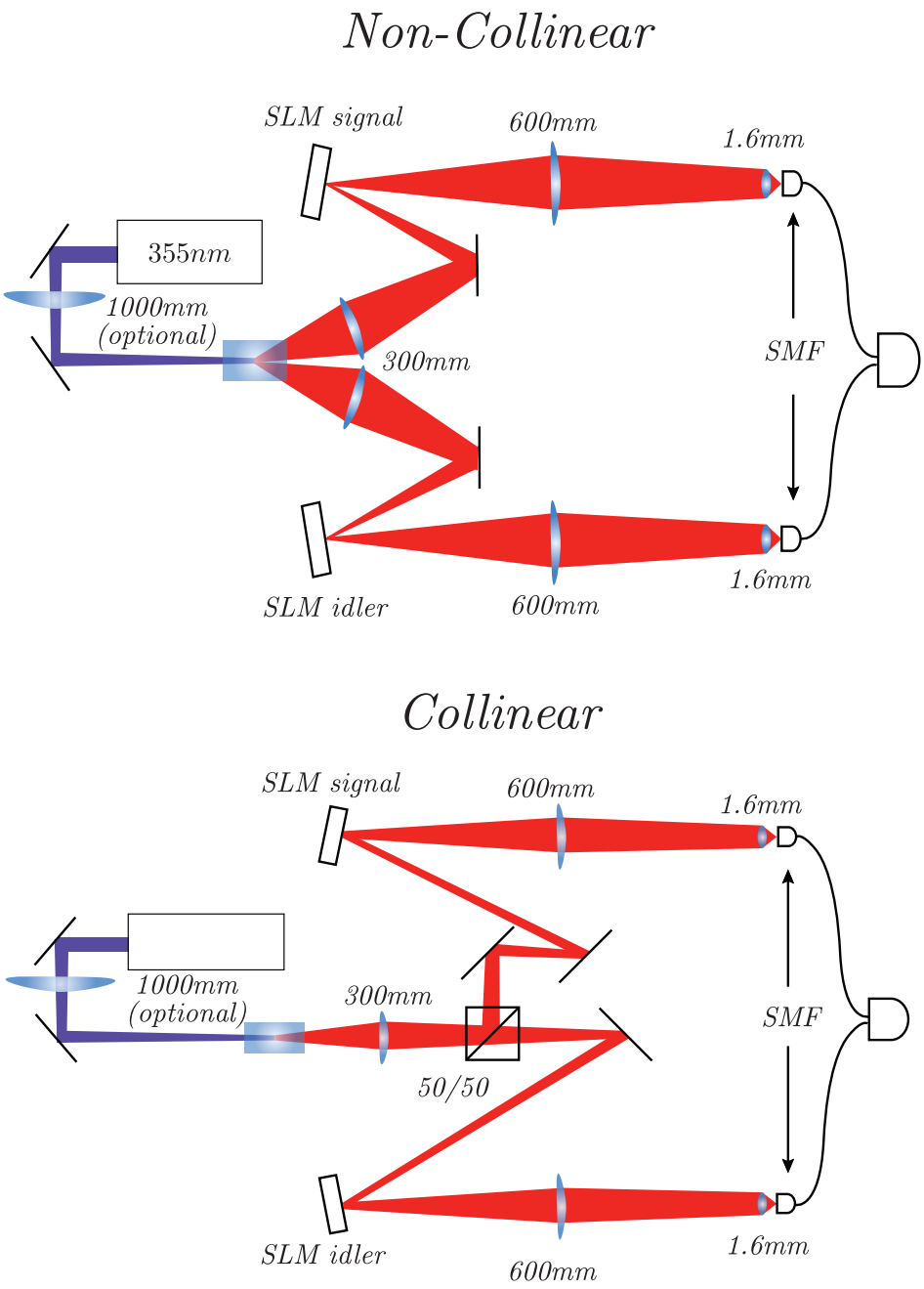


Figure 2.11: Experimental setup of near-field crystal measurements for both collinear and non-collinear systems.

A necessary condition for measuring coincidences between photon pairs in these experiments is that one of the single mode fibers can be back-projected and imaged onto the other single mode fiber, treating the crystal as a mirror. This condition is an effective predictor of the experimental outcome, and indicates whether or not a given optical configuration will work. One such unfolded system for measuring coincidences in the far field of the crystal is shown in Fig. 2.12 (a). The unfolded experiment suggests that the imaging conditions are met, and we would anticipate to measure coincidences in this configuration.

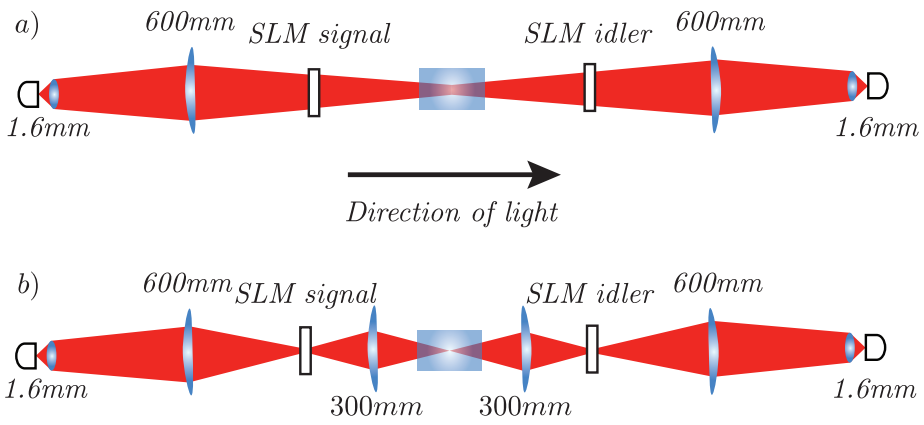


Figure 2.12: Unfolded system for both near (a) and far (b) - field measurement systems. The signal detector is imaged onto the idler detector in both cases. We can expect both of these experimental systems to be suitable for measuring coincidences.

The unfolded model with the SLMs in the image plane of the crystal is shown in Fig. 2.12 b). As can be seen, the fibers, SLMs and crystal are all

in conjugate planes.

It is worth noting the differences between linear position-momentum and angle-OAM for the down-converted light. Measurements of linear position correspond to near-field correlations, and measurements of linear momentum correspond to far-field correlations. For OAM, the singular point of phase is topologically stable in all planes. This means that in near field, far field or any intermediate field we can still measure the OAM state of the light. For angular distributions, the intensity distribution changes depending on the plane, but given that we can decompose any angular distribution into its spiral harmonics (from the Fourier relationship), we should be able to deduce a given angular function by measuring its OAM spectrum.

A further consideration beyond meeting the imaging conditions is which specific magnification/demagnification should occur and at which points. It is essential that a sufficient number of pixels on each SLM is illuminated, in order to avoid pixellation and loss of diffraction efficiency. However, completely filling the SLM window will necessitate aberration correction as the SLM isn't completely flat over the 20 $mm^2$ active area. The desired outcome is to illuminate an area large enough to avoid pixellation, but small enough to avoid aberration compensation. This approximately sets the condition of magnification between the fiber and the SLM. The single mode fibers have an aperture size of $5\ \mu m$. Coupling into the fiber with a 100x Zeiss objective (f=1.6), approximately 1200 mm away from the SLM gives a magnification of approximately 750, hence the spot size at the SLM is between 3 mm and

4 mm - small enough to avoid the need for aberration correction but large enough to illuminate many pixels on the SLM. Another lens is needed between the SLM and the crystal face to satisfy the imaging conditions. This means that a back-projected spot at the SLM has to be de-magnified onto the crystal. The choice of focal length for this lens sets the size of the back-projected signal and idler modes, and requires careful consideration in order to properly determine the detection bandwidth of the experiment. There are two extreme cases:

- The back-projected signal/idler beam is larger than the pump beam. In this situation we would *only* see overlap with the pump for the $\ell = 0$ mode because any back-projected mode with $\ell \neq 0$ will have a nodal point in the centre, and hence, zero overlap with the pump beam.

- The back-projected signal/idler beam is focussed very tightly. Here, the back-projected beam will have overlap with the pump for a large number of OAM states. However, we will only be collecting light from a very small portion of the crystal, and can expect to measure a very low count rate for all OAM measurements.

Using a 300mm focal length lens in a 4-$f$ imaging configuration, sets the back-projected spot size to around approximately $200\mu m$, sufficiently smaller than the pump beam to provide a good overlap for a large range of OAM states.

### 2.4.1 Alignment by Back-Projection

In a low photon flux regime, alignment of the optical path from the crystal to the fibers can be a significant challenge. A method used to simplify this is by aligning back-projected, visible laser light from each fiber to the crystal. We do this by coupling a 710nm laser diode into the single mode fibers in signal and idler arms, and propagating those back projected $\ell = 0$ beams to the crystal. Provided that both back projected beams propagate through the correct optical path (determined by apertures placed in the system) and overlap at the crystal, we can be assured that the down converted light will be approximately aligned, and subsequent fine adjustments can be made to fully optimize the system.

When initially aligning by back-projection, the SLMs are switched off. With no power to the SLM, the liquid crystal behaves as a mirror. By aligning the system with SLMs off, the down converted light coupled into the fiber will follow the path of the zero order light. Once optimized with the SLMs unpowered, the SLMs are powered, with blazed diffraction grating holograms displayed in signal and idler arms. This will reduce the coincident count rate to zero. This is because the light after the hologram will either be diffracted to a different position to the fiber (if the SLMs are in the Fourier plane of the fibers) *or* the light will be in the same position, but with an angle exceeding the acceptance angle of the fiber (if the SLMs are in the image plane of the fibers). In either case, one can recover the coincidences by adjusting the angle of the SLM, such that only the +1 diffracted order is coupled into

the fibers. Additionally, any hologram with a defined central axis (such as a spiral phase plate) must be centred with respect to the beam axis. An off-axis spiral phase hologram will couple a non-pure or superposition state of light into the single mode fibers.[34] Given that the holograms are addressed by computer, adjusting the centre of the hologram is a simple process. There are a number of ways one may choose find the optimal position of a hologram. For example, an $\ell = 0$ hologram has no central axis, so measuring $\ell_s = 0$ against $\ell_i = 1$ in signal and idler arms will yield zero coincidences if aligned, and non-zero if misaligned. This method can be applied to both signal and idler holograms to find the centres. Once the count rates are optimized in this configuration, the system is ready to measure coincidence rates as a function of any given spatial modes.

## 2.5 SLM control software

The SLMs are computer controlled through a DVI interface, effectively acting as additional monitors of the computer display. By assigning the greyscale holograms to display on these additional windows, each pixel of the LCD takes on a voltage determined by the greyscale level of the calculated hologram. The holograms are calculated within the LabView environment, which provides a convenient interface for calculating and displaying 2D arrays of data. The LCD displays on the SLMs have 512x512 active pixels. Arrays of this size can be handled by LabView without any issues concerning efficiency

and computation time.

We use a blazed diffraction grating to couple as much light as possible into the +1 diffracted order i.e. a grating where each "line" is modulated with continuous phase ramp from 0 to $2\pi$. This phase distribution is analogous to the phase change caused by a wedge of glass which is phase wrapped between 0 and $2\pi$. The "height" of the ramp sets the angle of deviation of the light which corresponds to increasing the number of lines across the grating. This hologram is calculated pixel by pixel, with phase values determined by

$$\phi_{x,y} = \frac{-2\pi}{\lambda}(xsin(\alpha) + ysin(\beta)) \tag{2.4}$$

where $x, y$ are the horizontal and vertical pixel positions, $\alpha, \beta$ is the diffracted angle in $x-z$ and $y-z$ planes respectively, and $\lambda$ is the wavelength of light.

Another commonly used hologram is the spiral phase hologram, characterized by the azimuthal phase $exp(i\ell\phi)$. The phase $\phi_{x,y}$ for each pixel is given by,

$$\phi_{x,y} = arctan\left(\frac{x}{y}\right), \tag{2.5}$$

where $x, y$ relate to the pixel position in horizontal and vertical directions, and the on axis phase singularity is at $x = 0, y = 0$. Multiplying this phase by a given integer $m = \ell$ determines the number of cycles $\phi$ rotates through in the full $2\pi$ period.

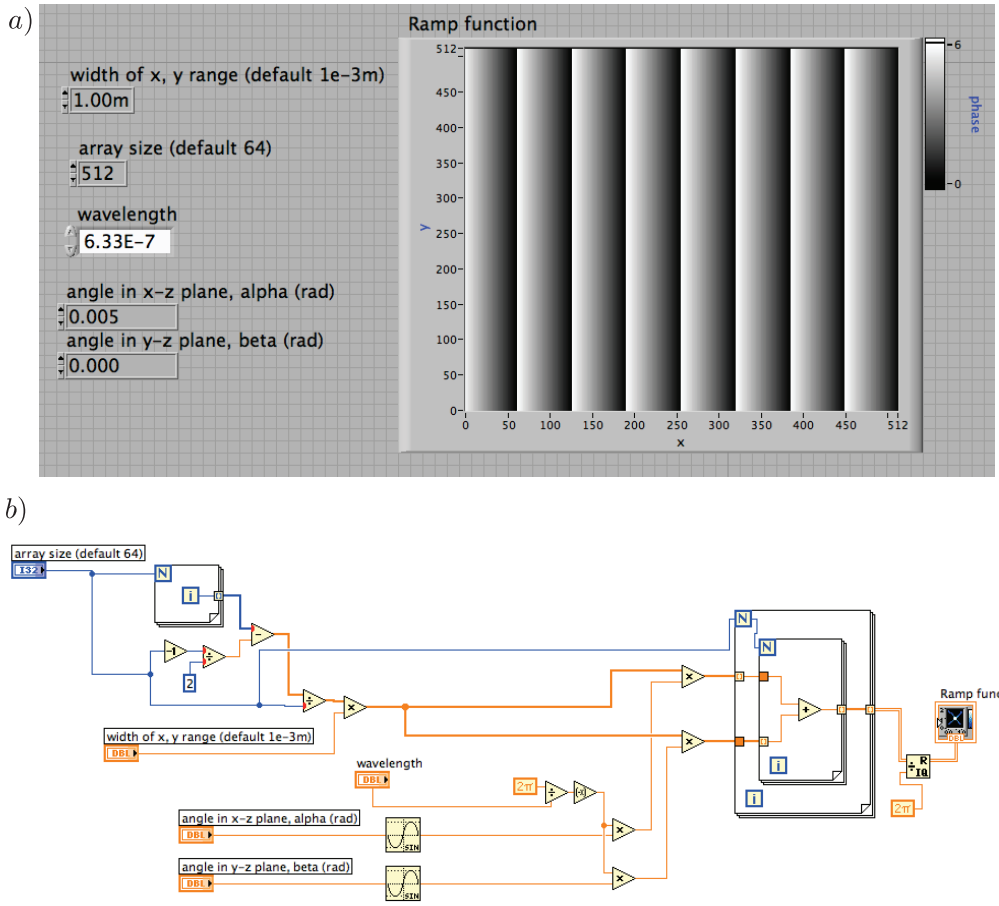


Figure 2.13: LabView code used to produce a blazed diffraction grating. a) Front Panel showing input parameters, and output array. b) Block-diagram algorithm used to generate the grating function.

With modulo $2\pi$ addition, any combination of phase masks can be added to produce another valid mask.

There are many more specific hologram designs which are used in the following experiments, which are all calculated using the same pixel-by-pixel method in LabView.

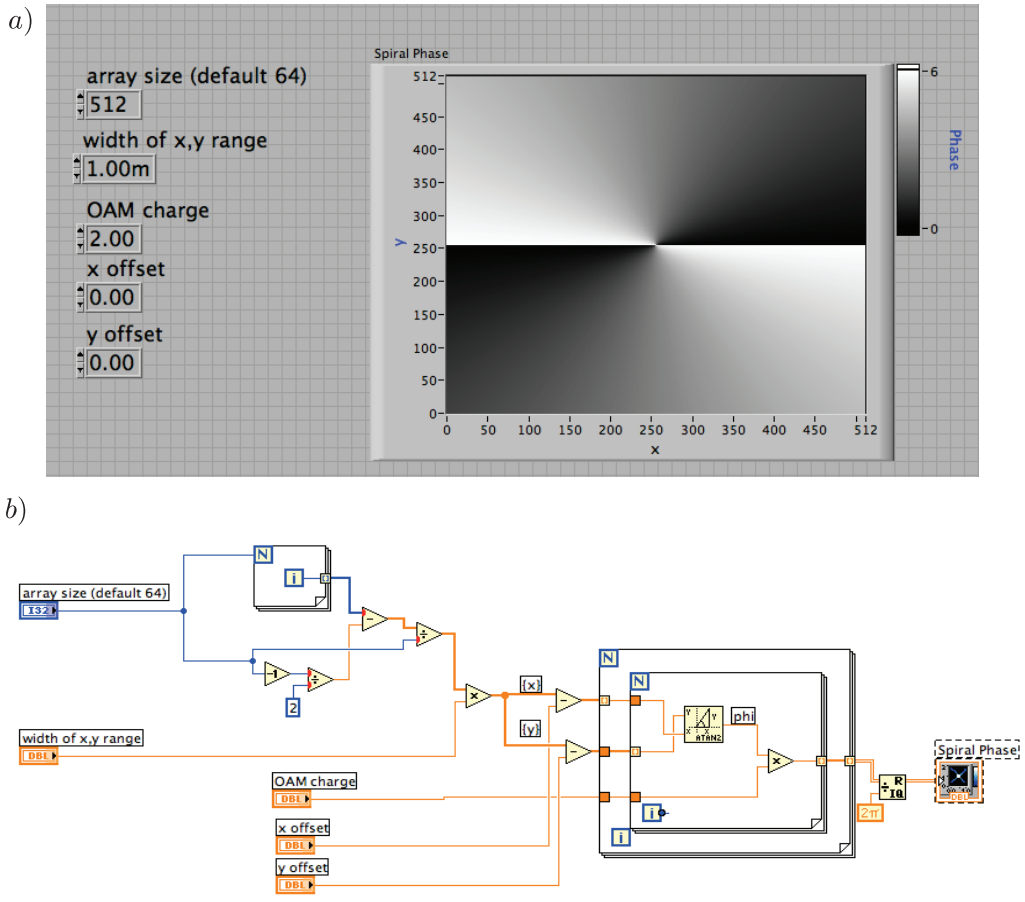


Figure 2.14: LabView code used to produce a spiral phase mask. a) Front panel showing input parameters and output. b) Block diagram of spiral phase algorithm.

### 2.5.1 General Purpose Control Software

It is useful to have a general purpose software tool, for the purposes of testing and diagnostics. This software need not be completely generic, but functional enough that one can run some simple experiments to test the system. For these reasons, a general purpose program was written with the capabilities

to:

- Assign holograms with spiral phase, blazed diffraction gratings, and $\pi$ phase discontinuities to both signal and idler SLMs.
- Measure single channel and coincidence count rates
- Scan a hologram property (grating angle, spiral phase, ... ) from one value to another, and measure the count rates as a function of that property.

Shown in Fig. 2.15 is the front-end user interface of the general purpose LabView program. Various hologram parameters can be set, such as diffracted angle in x and y, hologram centre in x and y, charge of spiral phase, number of phase/intensity dislocations, width and starting angle of phase/intensity dislocations. Each of these parameters can be scanned through a range of values, and the count rates measured for each value. For example, one can set SLM A to display an $\ell = 1$ mask, thus coupling $\ell = -1$ photons to the detector. By setting the program to scan the parameter L on SLM B, with range from -5 to +5, one can see the peak in coincidences when SLM B displays an $L = -1$ hologram, thus coupling $\ell = +1$ photons to the other detector.

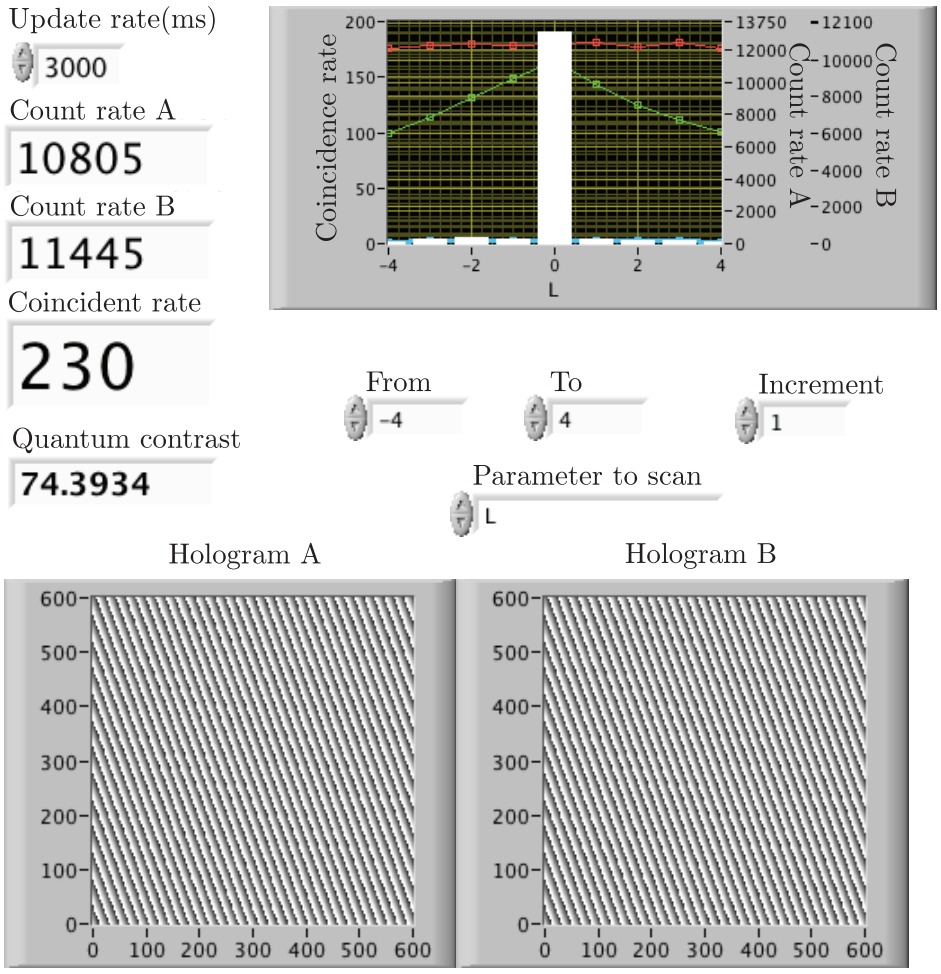


Figure 2.15: General purpose LabView Control software. Specific parameters can be assigned to both signal and idler holograms, and count rates measured. Additionally, any one of these parameters can be scanned through a given range, and count rates can be plotted as a function of the chosen parameter.

The grating angle of each hologram can be scanned to find the maximum coincidence rate, corresponding to the optimal angle in each case. Similarly, by scanning the central location of a (for example) $\ell = 1$ hologram on one SLM, with respect to an $\ell = 0$ in the other, one can find the optimal centre location. This is, in essence, a procedure for automatically aligning the down-conversion system.

### 2.5.2 Automatic Re-Alignment of the Optical System by Scanning Holograms

In setting up and aligning the down-conversion system, the most time consuming process is not in the coarse adjustments, but in the fine tuning of coupling the light into the fibers, and aligning the hologram centres. A system utilizing SLMs lends itself to an automated alignment process. Provided the SLMs are imaged onto the fibers, this can be done. If the fibers are in the Fourier plane of the SLMs, adjusting the angle of a grating results in a positional displacement of the diffracted order, which requires translation of the fiber position. Optimization of the centre of a hologram can be done in both near and far-field of the SLMs, as positional translation of a phase singularity occurs in all optical planes.

A suitable auto - alignment program has been developed in LabView, Fig. 2.16, which scans and measures coincidences as a function of eight parameters: x and y grating angles of SLMs A and B; x and y hologram centres

of SLMs A and B. A suitable scanning range and size of step is chosen for both angles and hologram centres. For the chosen parameters in this alignment method, scanning the angles will yield a maximum coincidence rate when optimal, and scanning the hologram centre will yield a minimum coincidence rate when optimal. Fitting a parabolic curve in each case is sufficient to find the optimal value for each parameter.

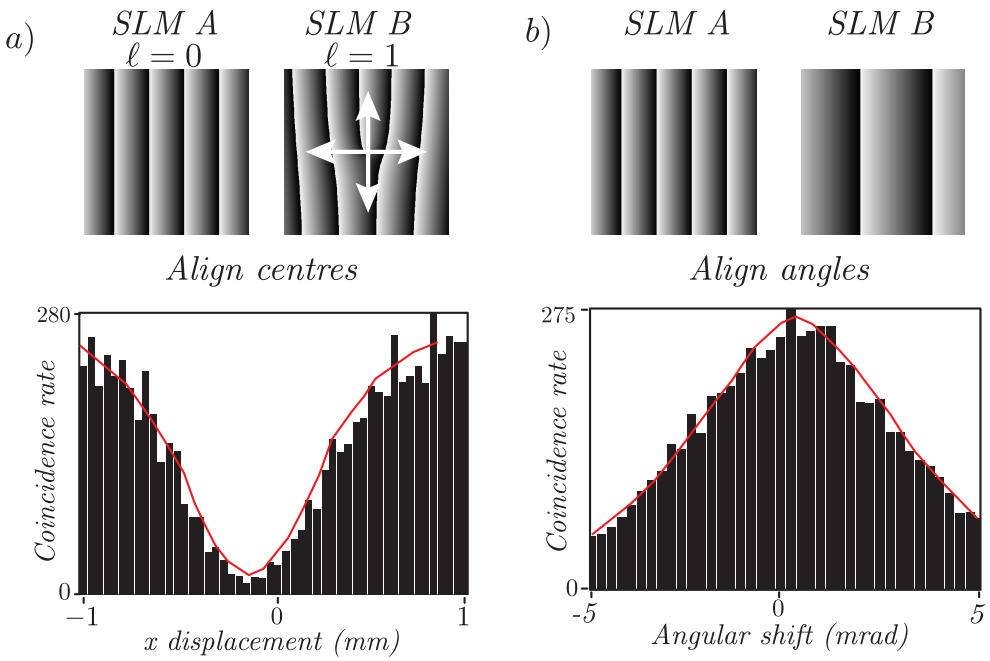


Figure 2.16: System to automatically align signal and idler holograms. (a) Setting the signal/idler hologram to measure $\ell = 0$ while scanning an $\ell = 1$ hologram in idler/signal results in zero coincidences when perfectly aligned. (b) Similarly, the optimum coupling into the fibers can be found by scanning the grating angle in one arm while keeping the other fixed. A parabolic curve (red line) is then fitted to each distribution, and the maximum/minimum is then taken to be the optimum value.

Using SLMs in this way to automatically align the optical setup is most

useful, as considerable time can be spent manually aligning the holograms. Additionally, thermal fluctuations result in misalignment of the optical path, and are measurable over a timescale of 2-3 hours, but can be periodically compensated for with automatic alignment. Automatic alignment allows data to be collected for an indefinite amount of time (provided the system is approximately aligned), meaning experiments with very low photon flux can be carried out without continual interruption.

CHAPTER

# THREE

# THE FOURIER RELATIONSHIP BETWEEN ANGLE AND ORBITAL ANGULAR MOMENTUM

This chapter presents the detail of two experiments designed to examine the Fourier relationship between OAM and angle variables. The first experiment described here examines purely classical phenomenon, and does not utilize the down-conversion system. It uses a Helium-Neon laser as a source, and a photo-diode for measuring optical intensity. In the second experiment of this chapter, similar holographic measurements are made, but the measurements now in coincidences of photon pairs produced in the SPDC experiment. This investigation of the Fourier relation between correlated photon pairs was carried out in collaboration with Dr. Anand Jha and Prof. Robert Boyd from the University of Rochester.

## 3.1 Angular Diffraction: A Classical Test

It is now established that OAM and angular position are related by a Fourier transform (Chapter 1).

This means that an angular restriction of the light profile modifies the OAM spectrum, generating new OAM components. This has previously been observed for classical light beams[87], and it is this work which we will expand on. Due to the analogy between the linear and angular Fourier relations, we interpret the effect of an angular mask on a light beam as "angular diffraction".

In the conventional single or multiple slit experiment a restriction in linear position of a light beam causes interference between the various Fourier components. This interference modifies the linear momentum and causes the characteristic diffraction pattern in the far field. The angular analogue of a single slit is a mask containing an angular step function, and the OAM spectrum of the transmitted beam is a discrete spectrum enveloped by a sinc square function, Fig. 3.1.

### 3.1.1 Theory of Angular Diffraction

Consider a mask with a uniform transmission of $t_1$ within an angle $\beta$ and a different transmission of $t_2$ elsewhere,

$$M(\phi) = \begin{cases} t_1 & \text{for } 0 \leq \phi < \beta \\ t_2 & \text{for } \beta \leq \phi < 2\pi \end{cases} . \tag{3.1}$$

The mask may be an amplitude mask, where the transmission takes on real values between 0 and 1, or a phase mask with $t = \exp(i\phi)$. The wavefunction of the transmitted beam is $\psi(\phi) = M(\phi)\psi_0(\phi)$, where we assume the initial mode $\psi_0(\phi)$ to be a pure OAM mode $\psi_0 \exp(i\ell_0\phi)$. The OAM spectrum of the transmitted beam is then the Fourier transform of the wavefunction:

$$A_\ell = \frac{1}{2\pi}\int_{-\pi}^{\pi} d\phi M(\phi) e^{-i\ell\phi}\psi_0 e^{i\ell_0\phi}. \tag{3.2}$$

The integration can be evaluated to

$$A_{\ell+\ell_0} = \psi_0 \begin{cases} \frac{\beta}{2\pi}(t_1 - t_2)\text{sinc}(\frac{\beta}{2}\ell)\exp(-i\frac{\beta}{2}\ell) & \text{for } \ell \neq \ell_0 \\ \frac{\beta}{2\pi}(t_1 - t_2) + t_2 & \text{for } \ell = \ell_0 \end{cases} \tag{3.3}$$

This is equivalent to expressing the mask in terms of the OAM harmonics $\exp(-i\ell\phi)$. Note that the relative weighting of the OAM modes other than $\ell = \ell_0$ remains the same irrespective of the values of $t_1$ and $t_2$, and in particular irrespective of whether it is an amplitude or phase mask.

The OAM spectrum for an absorption mask with $t_1 = 1$ and $t_2 = 0$

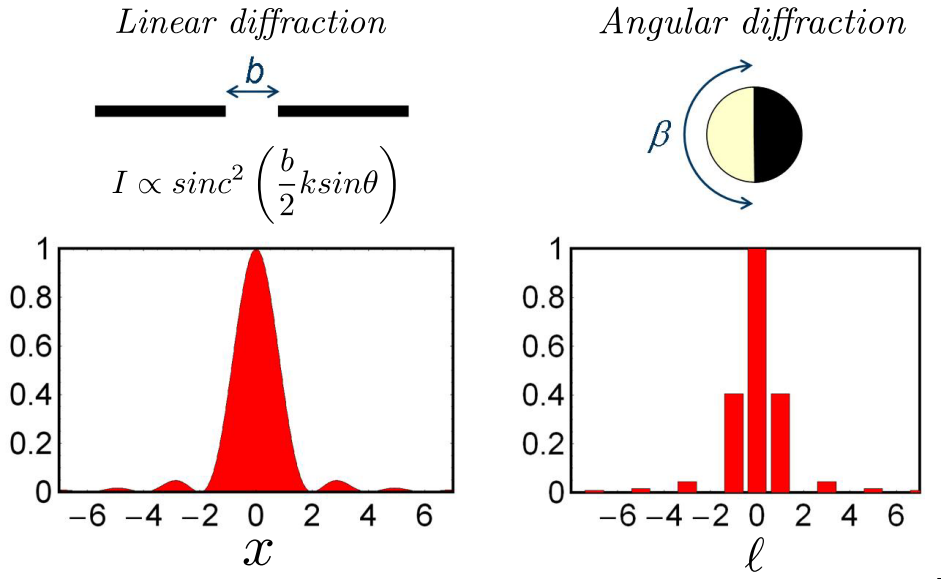


Figure 3.1: The analogy between linear diffraction at a slit, and angular diffraction at an angular aperture. Because of the cyclic nature of angle, the OAM spectrum is a discrete series, with a $sinc^2$ envelope determined by the angular width.

simplifies to

$$|A_\ell|^2 = |\psi_0|^2 \left(\frac{\beta}{2\pi}\right)^2 \mathrm{sinc}^2\left(\frac{\beta}{2}\ell\right). \tag{3.4}$$

This bears similarities to the diffraction pattern from a linear single slit experiment. While the diffraction pattern of a single slit is a continuous intensity distribution of linear momentum, or position in the far field, angular diffraction is a discrete distribution, enveloped by a $sinc^2$ function.

This analogy can be extended to multiple slit diffraction. The angular analogue of a double slit is a mask with two symmetrically placed opening

angles, and a grating of $N$ slits corresponds to an angle mask with $N$-fold symmetry. The individual opening angle $\beta$ corresponds to the single slit width and the repetition angle $\alpha$ to the separation between the individual slits, i. e. the grating constant, see Fig. 3.2.

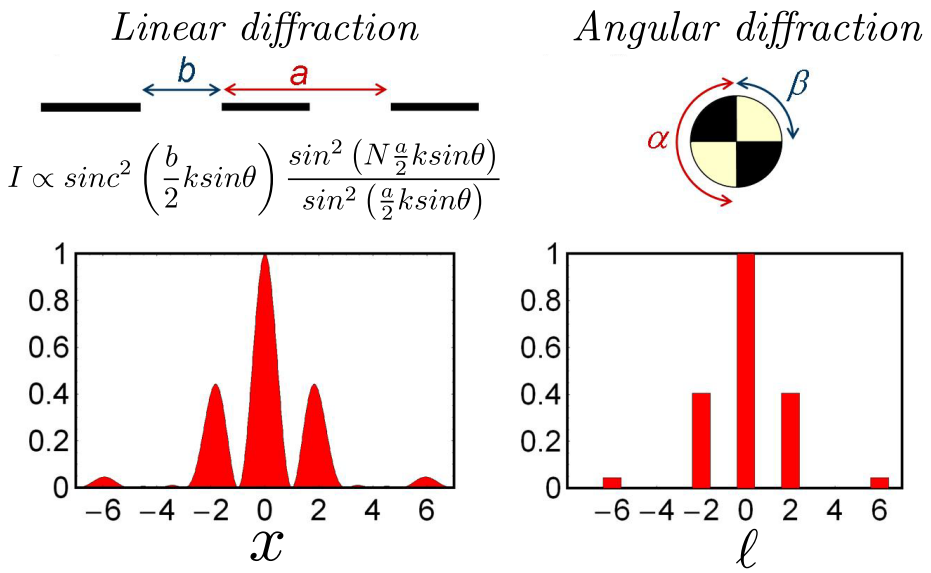


Figure 3.2: The analogy between linear diffraction at a grating, and angular diffraction with multiple angular slits. The N-fold symmetry of the angular mask determines which OAM states are suppressed. For a twofold symmetric mask, all odd OAM states cancel out.

As one may expect, in this case the sinc envelope of the single slit or opening angle is convolved with a function that describes interference between the slits/opening angles. Due to the periodicity of the angle mask, the repetition angle $\alpha$ is directly linked to the number of opening angles $N$ by $\alpha = 2\pi/N$. The angular version of a diffraction grating with with $N$ opening angles of width $\beta$ is described by the mask

$$M(\phi) = \begin{cases} 1 & \text{for } n\alpha \leq \phi < (n\alpha + \beta) \\ 0 & \text{else} \end{cases}, \tag{3.5}$$

where $n = 0, 1, ...N-1$ and $N = \alpha/(2\pi)$.

As before we can find the OAM decomposition of the transmitted beam from the Fourier transform:

$$\begin{aligned} A_{\ell+\ell_0} &= \frac{1}{2\pi} \sum_{n=0}^{N-1} \int_{n\alpha}^{n\alpha+\beta} d\phi e^{-i\ell\phi} \psi_0 & (3.6) \\ &= \psi_0 \frac{\beta}{2\pi} \text{sinc}(\frac{\beta}{2}\ell) \exp(-i\frac{\beta}{2}\ell) \sum_{n=0}^{N-1} e^{-i\ell 2\pi n/N} \\ &= \psi_0 \frac{\beta}{2\pi} \text{sinc}(\frac{\beta}{2}\ell) \exp(-i\frac{\beta}{2}\ell) \\ &\quad \times \exp[-i\ell\frac{\alpha}{2}(N-1)] \frac{\sin(N\frac{\alpha}{2}\ell)}{\sin(\frac{\alpha}{2}\ell)}, & (3.7) \end{aligned}$$

in analogy to diffraction off a conventional multiple slit experiment, see Fig. 3.2. A mask with two-fold symmetry causes cancelation of every odd OAM component and in an $N$-fold geometry only every $N$th OAM component survives. It is worth pointing out that for rational fractions between opening angle and repetition angle the typical cancelation of diffraction orders can be observed in the angular case.

### 3.1.2 Experimental Setup

We use a Helium-Neon (HeNe) laser tube producing a Gaussian beam, Fig. 3.3. This illuminates an SLM, which is used to realize both the angular aperture holograms and to measure the OAM spectrum of the light. This is done by coupling the first diffracted order from the SLM into a single mode fiber. The intensity of the coupled light at the output of the fiber is then measured with a photodiode.

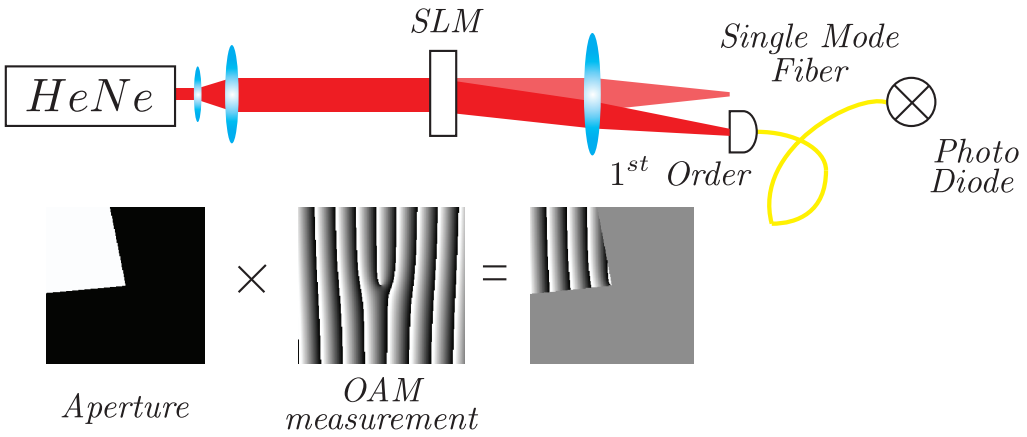


Figure 3.3: Experimental setup. The desired aperture is displayed on the SLM, on which the forked holograms of differing charge $\ell$ are scanned through a range of $\ell = -12$ to $\ell = +12$. Selective coupling to the fiber then allows us to measure the OAM spectrum for a given angular mask.

Fig. 3.4 shows the measured OAM spectrum for an aperture mask with a single opening angle. If no aperture is placed in the beam, the OAM is not modified, and accordingly we detect almost all of the light in the

state $\ell = 0$. Figs. 3.4b)-d) show the characteristic $sinc^2$ OAM spectrum for aperturing half, a third and a sixth of the beam respectively. The OAM spectrum is narrowest for an aperture of $\pi$ and becomes larger if the aperture angle increases or decreases. This is because for the periodic angle mask, the transmitted modes do not change if a mask is replaced with its inverse mask. Just like in a conventional single slit experiment, destructive interference between the transmitted light results in dark fringes in the diffraction pattern. A complete cancelation of OAM modes occurs if the opening angle $\beta$ is a rational fraction of $2\pi$, for example for a mask that blocks a third (or two thirds) of the beam, modes with $\ell = \pm 3, \pm 6, \pm 9, \ldots$ are suppressed in the OAM spectrum.

Alternatively, angular phase apertures can be realised with a $\pi$ phase discontinuity across the beam. Phase gratings are more efficient than amplitude gratings, as they do not discard any of the light. Phase gratings with opening angles which are rational fractions of $\pi$ completely suppress the zero order transmission through destructive interference, shown in Fig. 3.5.

The angular analogue to multiple slit diffraction is shown in Fig. 3.6, displaying the OAM spectrum of masks with 2, 3 and 4 symmetrically placed blocked beam areas of $\pi/3$. An $N$-fold repetition of an angular pattern will result in a spreading of the OAM modes just like an increase in the grating constant will result in a spreading of the diffraction pattern for a linear grating. The $sinc^2$ envelope of the single aperture of angular width $\pi/3$ is convolved with the $\frac{\sin^2(N\frac{\alpha}{2}\ell)}{\sin^2(\frac{\alpha}{2}\ell)}$ pattern arising from interference between the in-

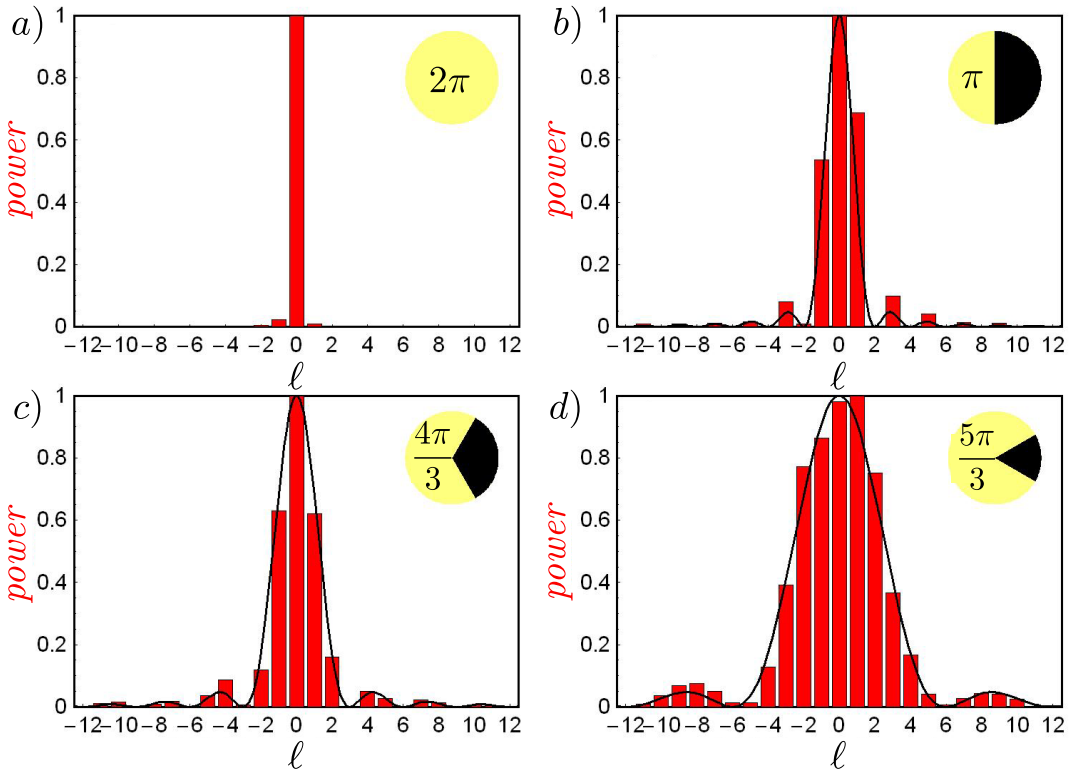


Figure 3.4: Measured OAM spectrum for single hard edged opening angles of a) $2\pi$, b) $\pi$, c) $4\pi/3$ and d) $5\pi/3$.

dividual angular opening angles. Fig. 3.6 visualises how an $N$-fold symmetric mask causes constructive interference for modes with OAM being multiples of $N$: The top row shows the phase profile of OAM modes with $\ell = 0 \rightarrow 4$ displaying $\ell$-fold symmetry. By blocking these light beams with a 2-fold symmetric mask, light emerging from the two opening angles has opposite phase for odd values of OAM and equal phase for even values. Consequently, all odd OAM components are missing from the OAM spectrum.

The description here applies to hard-edged apertures, however this does

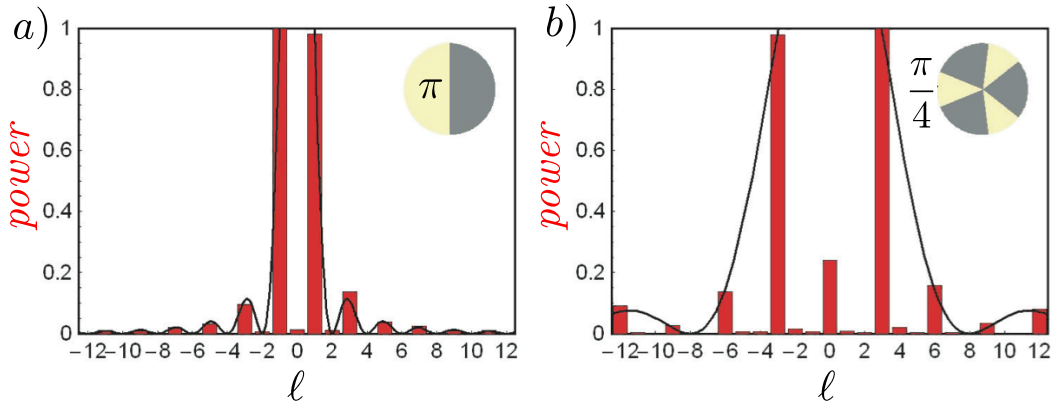


Figure 3.5: OAM spectra for two different phase masks. For each case, the spectrum is the same, with the exception of the $\ell = 0$ zero order, where destructive interference occurs.

not need to be the case e.g. one could engineer a Gaussian envelope for a Gaussian angular transmission function, or discrete sidebands for a sinusoidal variation of the angular transmission.

Angular diffraction is a direct demonstration of the Fourier relation between OAM and angular position. By expanding on the work of[87], we take the angular analogue of conventional diffraction from single and multiple slits, and we find excellent agreement with theory and experiment. These results, while classical, demonstrate that holographic measurements of angle and OAM states using both phase and amplitude masks can be made with a high degree of precision.

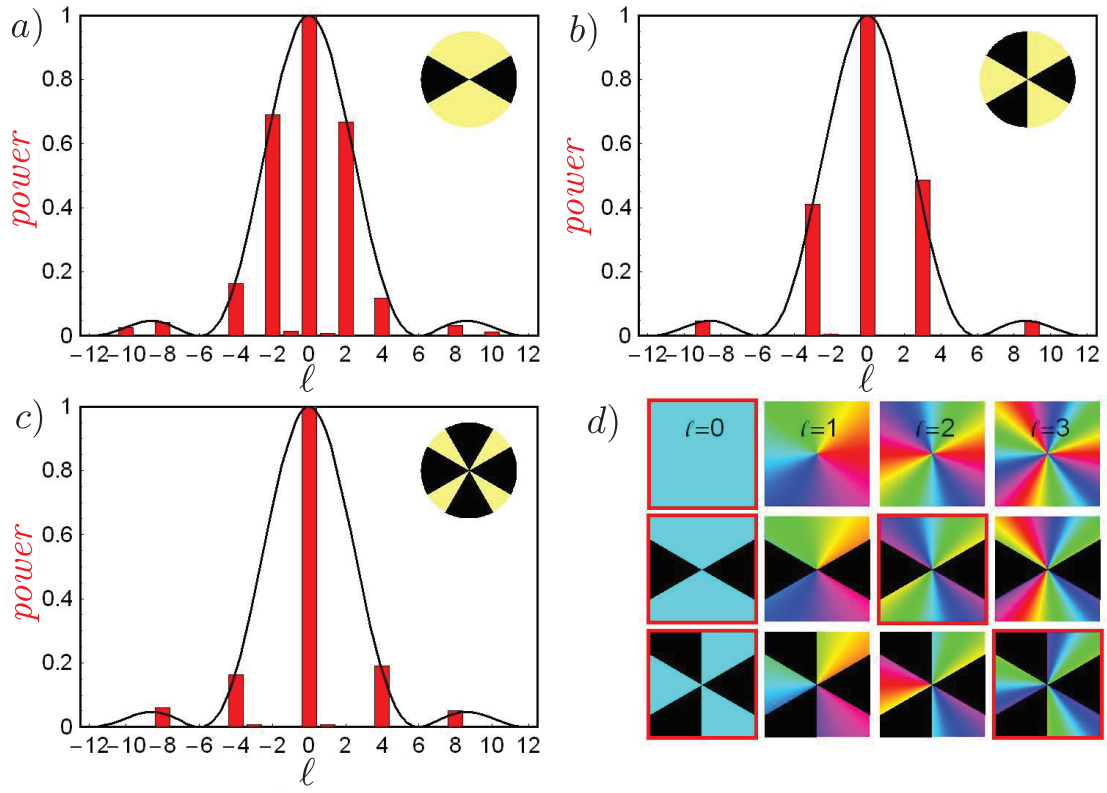


Figure 3.6: a),b),c), OAM spectra for multiple slits of varying number and mark-space ratio. The number of modes present is determined by the number of slits, and the suppressed orders are determined by the width of the apertures. d) Illustration of how certain apertures invoke total destructive interference of certain OAM states. When the correct OAM state overlaps with the correct aperture, the phase no longer cancels to zero, which determines the OAM spectrum.

## 3.2 Angular Diffraction at the Quantum Level

As Angular Diffraction is now well established at the classical level, it will now also be tested at the single photon level with down-converted photon pairs. Because of the correlated nature of these photon pairs, we can also demonstrate that the angular diffraction principle applies *non-locally* between signal and idler photons. By setting an angular mask in signal photons, one can then measure the effect on the OAM distribution non-locally in the idler photons.

Because each of the down-converted beams - viewed independently - are spatially incoherent[88], the diffraction signature we are exploring exists only in the coincidence measurements, and is not visible when considering the single channel count rates of either arm of the system. In the classical experiment, an angular mask was used to generate a superposition of OAM states, which were subsequently measured using single mode fiber. In this experiment, the light from the angular mask is coupled into single mode fibers, and is measuring, as opposed to generating, an angular state. In this case, it can be said that the angular mask in one arm filters out specific OAM modes in the other arm, which are measured in coincidence. Again, SLMs are used to realize holograms to set angular masks, and spiral phase masks to measure the OAM states. The angular state holograms are of the same type used in the classical experiment. The experimental setup is shown in Fig. 3.7.

In this experimental configuration, the down-converted light is emitted

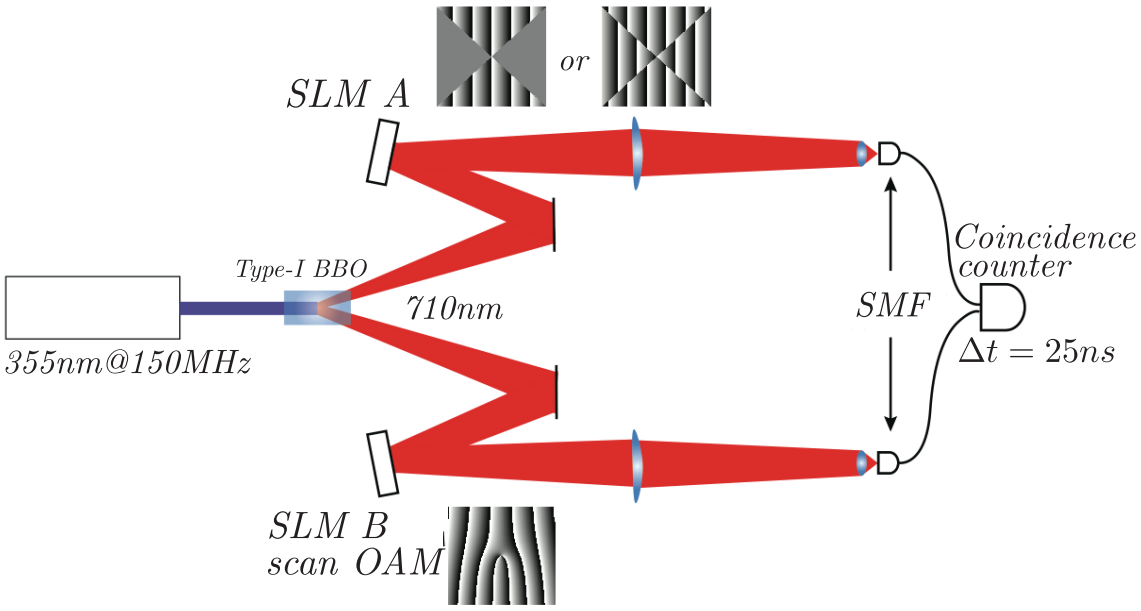


Figure 3.7: Experimental configuration. An angular aperture mask is displayed in one arm of the experiment, and the OAM measurement is performed in the other arm. By measuring the correlations, one should be able to non-locally measure the OAM spectrum in coincidences.

with a semi-cone angle of 4°. The single mode fibers are imaged to the crystal with a magnification of approximately 20:1, using 60mm focal length lenses. The SLMs are placed in the approximate far-field of the crystal plane.

As discussed, the anticipated coincidence rates can be numerically predicted using the overlap integral[53], which, for a large pump beam of $\ell_p = 0$, is proportional to

$$C \propto |\int \Psi_s \Psi_i \mathrm{d}A|^2 \tag{3.8}$$

where $\Psi_{s,i}$ are the wave-functions of the signal and idler states post-selected using the SLMs. The holograms used are angular functions of the same form as in the classical experiment, which can be phase or intensity distributions. These masks can be expressed as a Fourier series of OAM harmonics,

$$\psi(\phi) = \sum_{\ell=-\infty}^{\infty} A_\ell exp(i\ell\phi) \tag{3.9}$$

For hard-edged apertures of number N, with an open segment width $\beta$, $\psi(\phi) = 1$ for $-\beta/2 < \phi + 2\pi N/\ell \leq \beta/2$ and $\psi(\phi) = 0$ otherwise. For an $m$-fold symmetric mask, these non-zero $A_\ell$ components are,

$$A_{\ell=Nm} = \frac{m\beta}{2\pi} sinc\left(\frac{\beta}{2}\ell\right) \tag{3.10}$$

This mask, acting on an OAM eigenstate, produces a distribution of OAM values with amplitudes for the induced change in $\ell$ given by the $A_\ell$. As the individual signal and idler beams are spatially incoherent, this distribution is not visible in the single channel measurements. Conservation of OAM requires that if one of the down-converted beams passes through the mask and we measure the OAM of both beams, we should always find that the sum of the recorded OAM values is an integer multiple of m. Specifically, the coincidence rate will be proportional to

$$C_{\ell_s=Nm} \propto \left|\frac{m\beta}{2\pi} sinc\left(\frac{\ell_s\pi}{2m}\right)\right|^2. \tag{3.11}$$

### 3.2.1 Results

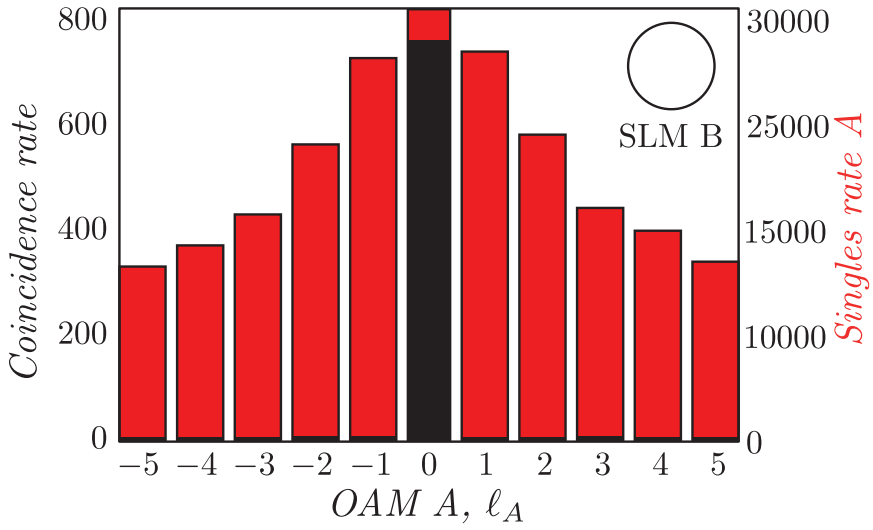


Figure 3.8: Coincidence measurements for no angular mask. Measuring signal OAM $\ell_s = 0$ sets the idler OAM $\ell_i = 0$. Any measured coincidences in other channels is due to cross-talk from misalignment of the holograms.

Fig. 3.8 shows the single channel and coincidence measurements for the case that no angular mask is present. The form of the single channel counts relate to the efficiency of the down-conversion process to generate different OAM states which decreases with increasing $|\ell|$. The single channel count rate in the arm with the mask is not affected by the scanning holograms in the signal arm, and is flat. The count rates on the two single channels was approximately $25000s^{-1}$. For $\ell_s = 0$ the coincidence count rate was approximately $750s^{-1}$, implying an overall quantum efficiency of detection of 3% and a pair production rate of around $10^6$. The accidental coincidence

rate here, from using the (NI PCI-6602) coincidence board is around $3s^{-1}$.

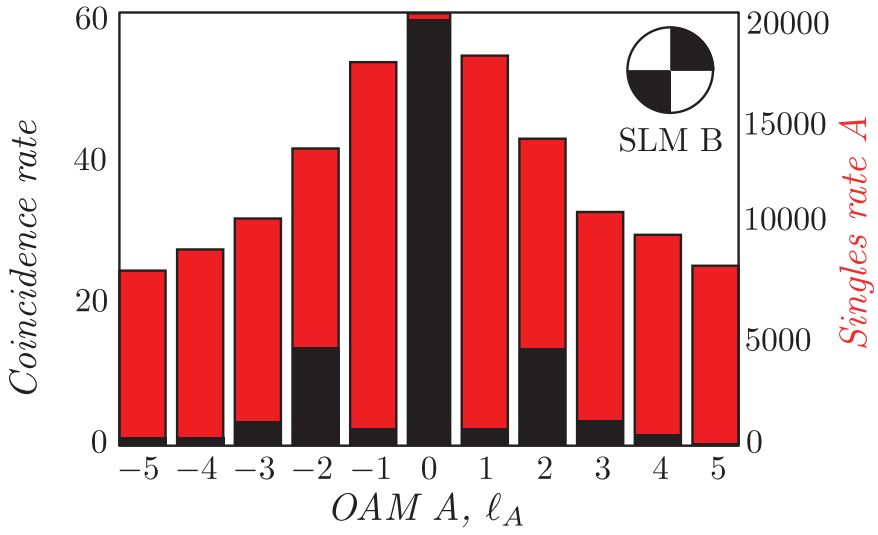


Figure 3.9: Coincidence measurements for a 2-fold symmetric angular intensity mask. Note the signature of the angular mask is present in the coincidence counts, but the single channel counts remain unaffected.

Fig. 3.9 shows the measured OAM distribution for a two-fold rotationally symmetric angular intensity mask (m=2). As can be seen, the coincidence measurements show sidebands at $\ell = \pm 2$, with the suppressed OAM modes at $\ell = \pm 4$, in accordance with theory. It is also apparent that the information in the single channel distribution has not changed - rather, that the mask in the signal arm has filtered out the appropriate OAM modes in the idler arm to be measured coincidentally.

Additionally, phase holograms can be displayed on the SLM to investigate the phase relationship between the correlated modes. For the case in

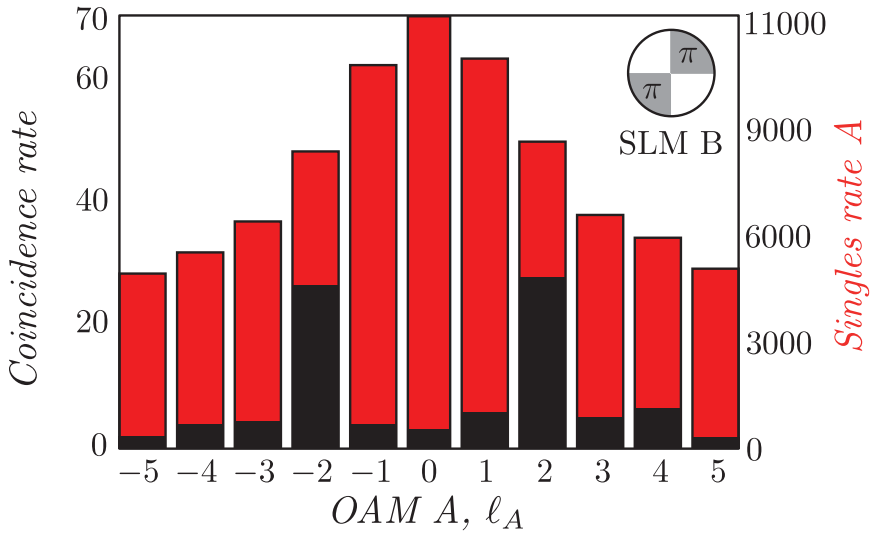


Figure 3.10: Coincidence measurements for a 2-fold symmetric angular phase mask. The mask has the same width as in Fig. 3.9, but varies phase apposed to amplitude. Note the cancellation of the $\ell = 0$ mode in the coincidence.

Fig. 3.10, there is a complete destructive interference of the $\ell = 0$ mode, due to the symmetry of the phase mask. Because the phase masks are more efficient than the intensity masks, the sidebands at $\ell = \pm 2$ have twice the coincidence count rate in each mode.

These results demonstrate the extension of the classical investigation of the angle-OAM Fourier relation into the single photon regime. Additionally, the angular states represented are non-local with respect to the OAM measurements. The results above show that, at the single photon level, it is possible to engineer specific OAM superposition states in idler photons, by realizing a specific angular state in signal photons. While these hard-edged

masks might not be suitable for tests of the EPR paradox or quantum measurements of the angular uncertainty principle, the results demonstrate that, with the appropriate holograms, the system should be capable of performing these types of experiment.

CHAPTER

# FOUR

# TESTS OF THE QUANTUM ENTANGLEMENT OF ORBITAL ANGULAR MOMENTUM

The previous chapter shows that our system can make single photon, holographic measurements of angle and OAM. This chapter will investigate quantitative measures of entanglement for the variables of angle and OAM. This includes a new, angular version of the historic EPR paradox, the violation of a Bell-type inequality for OAM subspaces, and tomographic measurements to reconstruct the entangled state produced by down-conversion. Experimental test of quantum entanglement firmly establish the variables of angle and OAM as quantum observables, and thus suitable candidates in quantum information protocols and quantum key distribution.

## 4.1 The Einstein-Podolsky-Rosen Paradox for Angles and Orbital Angular Momentum

In quantum systems, one of the hallmark tests is the violation of a Bell-type inequality, by demonstrating the measured correlations are not due to local-hidden variable theories. An alternative test of quantum entanglement is the demonstration of the EPR paradox. This is achieved by making coincidence measurements of conjugate variables with sufficient precision that - if the measured properties were predetermined before measurement - they would be in contradiction with Heisenberg's uncertainty principle.

In contrast to violating a Bell-type inequality, which applies to discrete state spaces, EPR correlations provide a demonstration of entanglement both for discrete and for continuous variables. Experimentally, EPR experiments have been demonstrated for polarization[89], energy and time[90], position and linear momentum[91] and with images[92].

We will demonstrate the EPR paradox for variables of angle and OAM, in analogy with the methods used by Howell *et. al.*[91]. In doing so, we will show that entanglement, as manifest in the EPR paradox, applies not only to linear, but also to angular variables[93].

To measure the angular position states, we define a Gaussian-profile, angular-sector transmission aperture that can be varied both in its width and orientation. A narrower aperture gives an inherently more precise measurement of angular position but with a reduced detection efficiency, as the

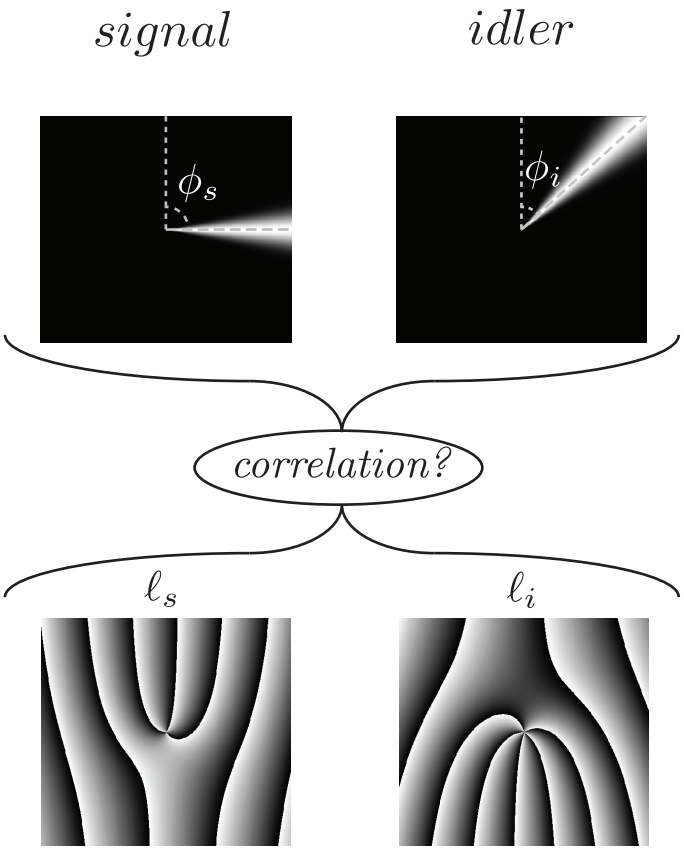


Figure 4.1: Method of measuring angles and OAM correlation. For angles, an aperture of fixed width is displayed on signal and idler SLMs. As the orientation of the aperture is varied, the angular correlation width, $\Delta\phi$ can be measured. For OAM, scanning through all possible values of a range of OAM states in signal and idler allows measurement of the OAM correlation width.

apertures are lossy in nature. Although the Gaussian profile does not correspond strictly to the minimum uncertainty state of angle[94], the precise profile and minimum width of the sector apertures are not central to this demonstration.

We use the SLMs in signal and idler arms to select both the angular orientation of each mask, and the charge, $\ell$, of the forked holograms, to measure the OAM, Fig. 4.1.

In practice, measurements are always made with a finite precision and hence the perfect correlations in both OAM and angular position are unobtainable. In order to demonstrate EPR correlations, we use the more experimentally useful criterion based on measuring the conditional probability of finding a particular outcome in one system given a measurement in the other[95]. This form of EPR can be expressed in the form of a joint uncertainty product,

$$[\Delta(\ell\hbar)]^2[\Delta\phi]^2 \geq \frac{\hbar^2}{4}. \tag{4.1}$$

The violation of this inequality demonstrates the non-separability of the angle and OAM measurements in signal and idler arms, and thus demonstrates the EPR paradox.

The experimentally measured angle and OAM correlations are shown in Fig. 4.2. Note that in both cases the actual value of the angular momentum or position in the signal and idler beams is not important; rather it is the difference between measurements in the signal and idler beams that determines the widths of the probability distributions. Fig. 4.3 expresses the measurements in terms of conditional probabilities $P(\ell_s|-\ell_i)$ and $P(\phi_s|\phi_i)$, from which the widths $\Delta\ell$ and $\Delta\phi$ are found.

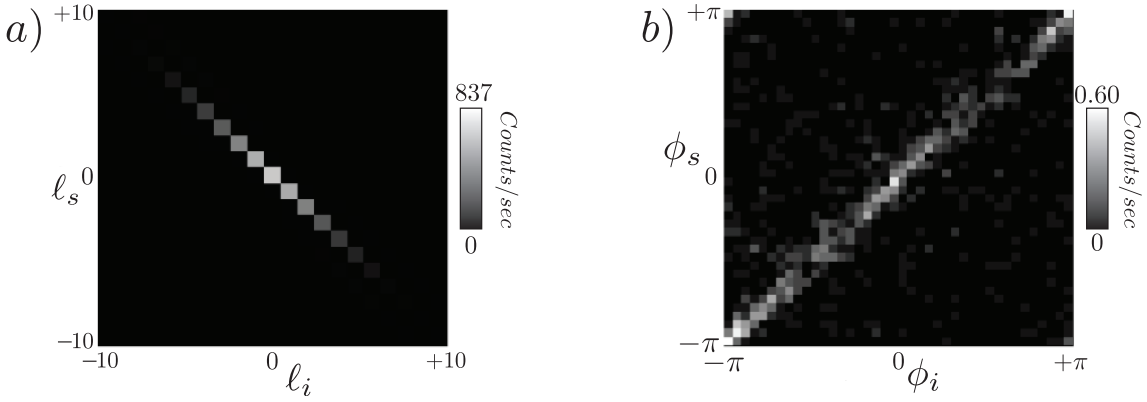


Figure 4.2: a) Measured coincidences for OAM measurements in signal and idler. As expected, the coincidences follow the anti-diagonal line and are anti-correlated. b) Coincidences for the angular measurements.

For the orbital angular momentum states we measure all combinations of $\ell_{s,i}$ from -7 to +7 corresponding to the approximate spiral bandwidth of our system. For the angular states we use an angular aperture width of $\pi/10$ and measure all combinations of $\phi_{s,i}$ in 60 equally-spaced angular bins. The measured correlations shown in Fig. 4.2 are maximal whenever $\ell_s = -\ell_i$ or $\phi_s = \phi_i$, respectively.

Care must be taken when determining the standard deviations of the angle and OAM distributions, $\Delta\ell$ and $\Delta\phi$. Small amounts of random noise, particularly at large deviations from the mean, leads to a measured standard deviation which depends on the range of OAM states measured and is therefore not physically meaningful. We attempt to minimize the noise level by running the experiment at low flux (approx. 20 000 photons/second) to

reduce the number of accidental coincidences. In addition, fitting a Gaussian distribution to the data will provide a more realistic measure of the standard deviation. A Gaussian fit is appropriate in this instance because the angular distribution is a narrow Gaussian in transmission.

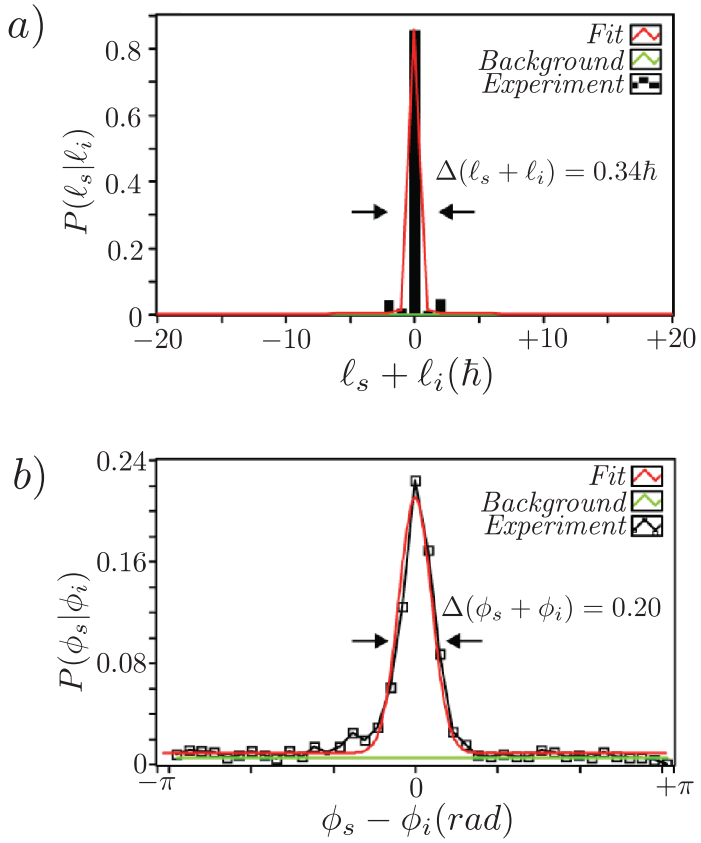


Figure 4.3: a) Conditional probabilities of the measurements in OAM. b) The conditional probabilities of the angle measurements.

Fig. 4.3 shows the measured correlations in OAM and angle. As can be seen, the peak in correlation is where $\ell_s + \ell_i = 0$ and $\phi_s - \phi_i = 0$. Fitting to

a Gaussian distribution, we find $[\Delta\ell]^2 = 0.11\hbar^2$ and $[\Delta\phi]^2 = 0.04\hbar^2$. Taking these values for the variance, we get a variance product of

$$[\Delta(\ell\hbar)]^2[\Delta\phi]^2 = 0.0048\hbar^2. \tag{4.2}$$

This product is clearly below the limit imposed by Heisenberg's uncertainty principle of $0.25\hbar^2$, demonstrating the EPR paradox for the chosen variables.

The results confirm that the EPR conclusion, namely that quantum mechanics is either incomplete or non-local, applies to angular position and OAM. Unlike demonstrations of Bell-type inequalities, which are restricted to discrete subspaces, EPR correlations simultaneously span an extended range of OAM states and the continuous state space of angular position. The demonstration of angular EPR correlations establishes that angular position and angular momentum are suitable variables for applications in quantum information processing, notably in protocols for quantum key distribution. True to the original EPR argument, the presence of hidden variables would resolve the system into one which fits a local-hidden variable theory.

## 4.2 Violation of a Bell's Inequality for Equally Weighted OAM Superposition States in 2 Dimensions

While EPR is a good demonstration of the non-local correlations which occur between entangled states, it does not rule out the possibility of hidden variables. In this section, we apply a Bell type inequality to OAM states, negating the presence of local-hidden variables as applied to the entanglement of OAM states. We make measurements in 2D subspaces of the unbound OAM space by drawing an analogy with the 2D state space of polarization.

We demonstrate the entangled nature of these OAM superposition states through violation of the CHSH inequality.

As described in Chapter 1, a Bloch sphere equivalent can be constructed for any superposition of $\pm\ell$ states, and provides a suitable description to explore 2-D state spaces of OAM. These $\pm\ell$ Bloch spheres are defined such that the north/south poles represent $\pm\ell$, and the equator states are equally weighted superposition "sector states" of differing orientation.

In order to quantify the degree of entanglement present between the correlated photons, we must measure correlations for a range of superposition states. For polarization, one can violate a Bell-type inequality by measuring the linear polarization states - the states on the equator of the Poincare$'$ sphere. A direct analogy for OAM then, would be to measure the correla-

tions between the sector states on the equator of the Bloch sphere. A sector state $|\psi\rangle$ is described by

$$|\psi\rangle = \frac{1}{\sqrt{2}}(|\ell\rangle_s + e^{i\ell\phi}|-\ell\rangle_i). \tag{4.3}$$

These sector states have $2\ell$ sectors of phase alternating between 0 and $\pi$.

Combining the above equation with the SPDC state (Chapter 1), we can calculate the anticipated coincidence rate $C(\psi_s, \psi_i)$ for a signal photon measured in equator state $|\psi_s\rangle$ and idler in $|\psi_i\rangle$ to be

$$C(\psi_s, \psi_i) = |\langle\psi_s|\langle\psi_i||\Psi\rangle|^2 \propto cos^2[\ell(\phi_s - \phi_i)] \tag{4.4}$$

where $\phi_{s,i}$ is the phase angle between sector states, represented as longitude on the equator of the sphere.

We realize sector state holograms like those shown in Fig. 4.4 on signal and idler SLMs, and measure coincidences as the angle between these holograms is varied, analogous to making measurements of linear polarization - by rotating polarizers in signal and idler arms. Historically, linear polarization states were measured to violate a Bell-type inequality and demonstrate entanglement, by measuring high visibility fringes in coincidence for different initial polarizer angles[45]. These high visibility sinusoidal fringes are the signature of two dimensional entanglement.

The sector states are experimentally defined by phase apertures on the SLMs. These phase apertures serve to select the two-dimensional subspace

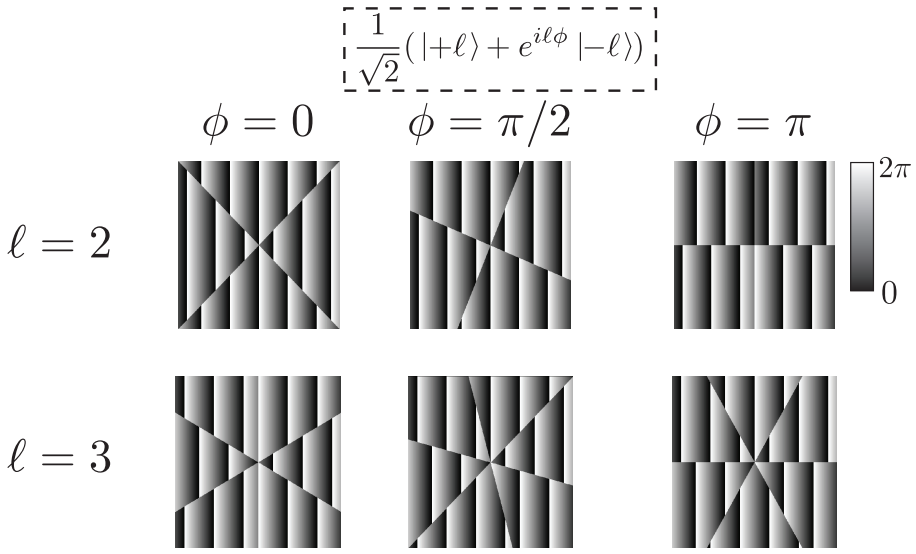


Figure 4.4: Examples of the sector state holograms used to violate the Bell inequality, for $\ell = 2$ and $\ell = 3$. By displaying the same sector holograms in each arm, and varying $\phi$ in one with respect to the other, one should observe sinusoidal fringes in coincidence.

and act as analyzers for these states when their relative orientation is changed. Using the SLMs as phase-only modulators results in measurements in a state-space higher than 2. This is because the hard edge of the phase step corresponds to small contributions associated with higher order $\ell$ components. These contributions however, are minimal.

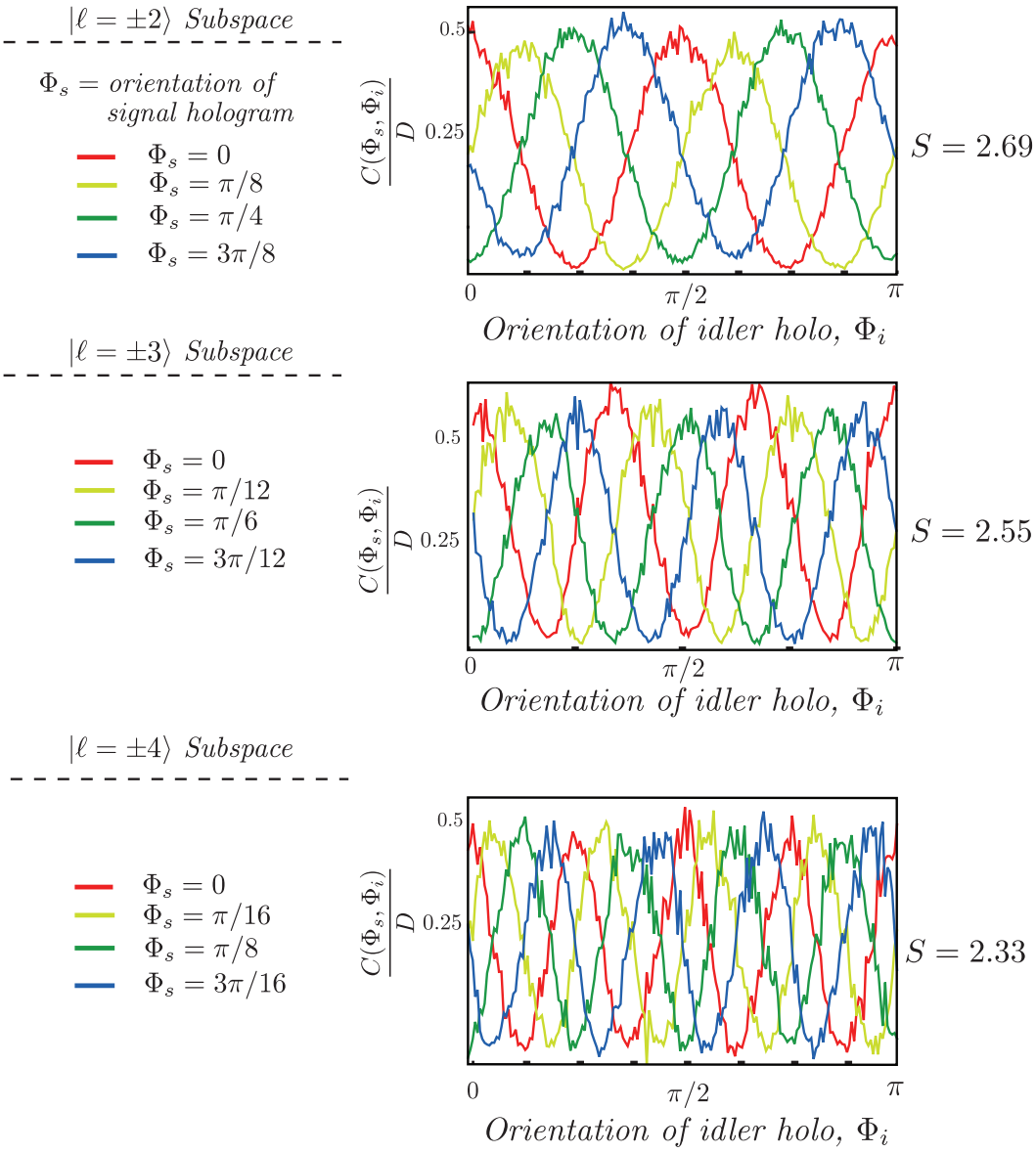


Figure 4.5: Bell curves for OAM subspaces of $\ell = 2, 3, 4$. In each case, the physical hologram is rotated through a full $2\pi$, to demonstrate the relationship between the phase angle and the physical orientation as $\ell$ increases. In each case, we violate the CHSH inequality, demonstrating the non-local correlations measured.

Fig. 4.5 shows the recorded coincidence fringes for sector state measurements for $\ell = 2, 3, 4$, as a function of the angle between the signal and idler states. The angles of the sector state holograms are equivalent to the orientation of the polarizers used to violate the Bell inequality for polarization. A frequently used Bell-type inequality is the Clauser-Horne-Shimony-Holt inequality (CHSH). For this experiment we define the Bell parameter S to be,

$$S = E(\mathbf{a}, \mathbf{b}) - E(\mathbf{a}, \mathbf{b}') + E(\mathbf{a}', \mathbf{b}) + E(\mathbf{a}', \mathbf{b}') \tag{4.5}$$

where $\mathbf{a}, \mathbf{a}'$, $\mathbf{b}, \mathbf{b}'$ are vectors corresponding to different measurement states selected by the appropriate holograms on the SLMs, and

$$E(\mathbf{a}, \mathbf{b}) = \frac{C(\mathbf{a}, \mathbf{b}) + C(-\mathbf{a}, -\mathbf{b}) - C(\mathbf{a}, -\mathbf{b}) - C(-\mathbf{a}, \mathbf{b})}{C(\mathbf{a}, \mathbf{b}) + C(-\mathbf{a}, -\mathbf{b}) + C(\mathbf{a}, -\mathbf{b}) + C(-\mathbf{a}, \mathbf{b})} \tag{4.6}$$

where $C(\mathbf{a}, \mathbf{b})$ is the measured coincidence rate as a function of hologram orientations $\mathbf{a}, \mathbf{b}$.

The CHSH inequality ($-2 \leq S \leq +2$) is violated for entangled systems, and sets the statistical bounds for local-hidden variable systems. The statistical upper limit for entangled systems in the CHSH inequality is $|S| = 2\sqrt{2}$. As can be seen from Fig. 4.5 each of the measurements of the equator states clearly violate the CHSH inequality, demonstrating the entangled nature of these sector states. The failure to reach the maximum value of $S = 2\sqrt{2}$ comes from degradation of the measured signal, potentially due to imper-

fections in alignment and accidental coincidences - resulting in a noise floor which reduces the overall fringe contrast.

## 4.3 Violation of a Bell's Inequality for Arbitrary Superpositions of OAM States in 2 Dimensions

One can further extend the analogy between polarization and 2-D OAM spaces by measuring not just the equator states, but also the OAM states analogous to circular and elliptical polarizations on the Poincare$'$ sphere. The versatility of the SLMs used to post-select specific modes means we are not restricted just to sector state measurements, but given the correct measurement holograms, we can access the entire 2-D OAM state-space. Again we measure the correlations between pairs of these modal superpositions to violate a Bell-type inequality. By demonstrating that these superposition states remain highly entangled, we are not only demonstrating the entangled nature of the states, but also that our measurement system can precisely measure correlations corresponding to arbitrary 2-D superpositions of OAM states.

In the previous section the measurements varied only one angular coordinate, $\phi_{s,i}$ as the equatorial angle on the Bloch sphere. In this section, we extend these measurements to superpositions represented by both longitude,

$\phi_{s,i}$, and latitude, $\theta_{s,i}$ for signal and idler states respectively.

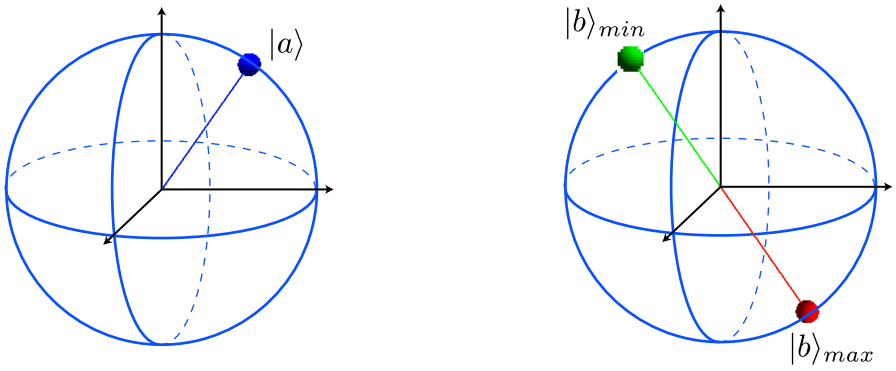


Figure 4.6: A state $|\mathbf{a}\rangle$ in the signal arm is maximally correlated with a state $|\mathbf{b}\rangle$ in idler, when it's latitude is reflected about the equator, but the same longitude. It's minimum is when it has the same latitude but reflected in longitude.

The coincidence rate $C(\mathbf{a}, \mathbf{b})$ for detecting one photon in state $|\mathbf{a}\rangle$ and the other in $|\mathbf{b}\rangle$, where $|\mathbf{a}\rangle, |\mathbf{b}\rangle$ are vectors on the Bloch sphere, is,

$$\begin{aligned} C(\mathbf{a}, \mathbf{b}) &\propto |\langle \mathbf{a}|\langle \mathbf{b}||\psi\rangle|^2 = \frac{1}{4}\Big[1 - \cos(\theta_a)\cos(\theta_b) \\ &+ \sin(\theta_a)\sin(\theta_b)\cos\left(\phi_a - \phi_b\right)\Big]. \end{aligned} \tag{4.7}$$

Therefore, we predict *maximum* coincidence for $\theta_b = \pi - \theta_a$ and $\phi_b = \phi_a$, corresponding to states with the same longitude but reflected about the equator, and *minimum* coincidence for $\theta_b = \theta_a$ and $\phi_b = \phi_a - \pi$, corresponding to states with the same latitude but reflected about the vertical axis, as shown in Fig. 4.6.

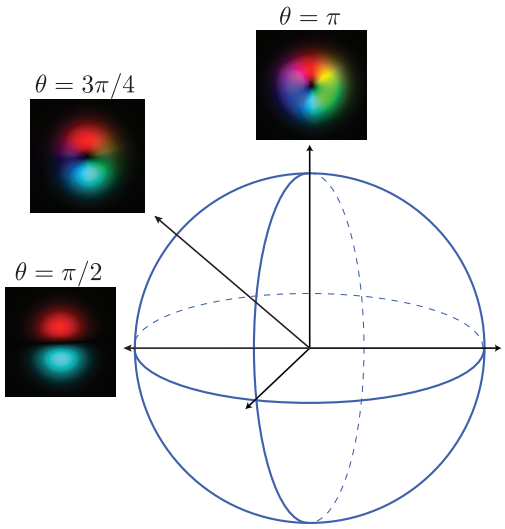


Figure 4.7: A state in-between the equator and the poles is equivalent to an elliptical polarization state. The example here shows the phase and intensity profile of an $\ell = 1$ superposition state which is halfway between the $HG_{10}$ and the $LG_{10}$ state. As a consequence, this state carries a fractional OAM charge.

The design of our SLM holograms here is necessarily more sophisticated than that of the previous holograms, which were either OAM eigenstates or sector states. The holograms incorporate a spatially dependent blazing function superimposed onto the phase distribution. This is necessary for the measurements to remain within a 2-D subspace of OAM and avoid significant mode contamination.

Our results, for the $\ell = \pm 2$ subspace, are shown in Fig. 4.8. In each case we plot the coincidence rate as one of the holograms is scanned around a great circle of the Bloch sphere, while maintaining the other superposition at one of four equally spaced states, represented by the black dots. The results from

the previous section correspond to measurements in a great circle around the equator of the Bloch sphere. The two examples shown here are those for a great circle which crosses both north and south poles, and an arbitrarily chosen great circle around the sphere. As expected, we observe sinusoidal fringes in the coincidence rate, characteristic of entanglement in 2 dimensions. In each case our results show a violation of a Bell-type inequality. We find the values of S to be $2.56 \pm 0.05$ for the polar great circle, and $2.59 \pm 0.05$ for the arbitrary great circle in Fig. 4.8 – clearly violating the constraints of a local, realistic hidden variable theory.

For the sector state measurements, one can approximate a 2-D OAM subspace by using phase-only holograms. The hard-edged phase step results in sidebands of higher-order OAM modes, but given that the SPDC source produces higher order modes with a reduced amplitude, they can be neglected, resulting in a minimal amount of mode contamination. However, measuring states on the sphere which are in between the equator and poles can only be effectively done with phase and intensity modulation of the holograms. To illustrate this point, Fig. 4.9 below shows the measured correlations between the same states as above in Fig. 4.8, but using *phase-only* holograms. In this case, it is clear that the measured variation in coincidence is not sinusoidal, and hence the phase-only holograms are inadequate for restricting the measurement space to 2 dimensions. It would be inappropriate to apply the CHSH inequality to these results, as the number of participating modes is no longer equal to 2.

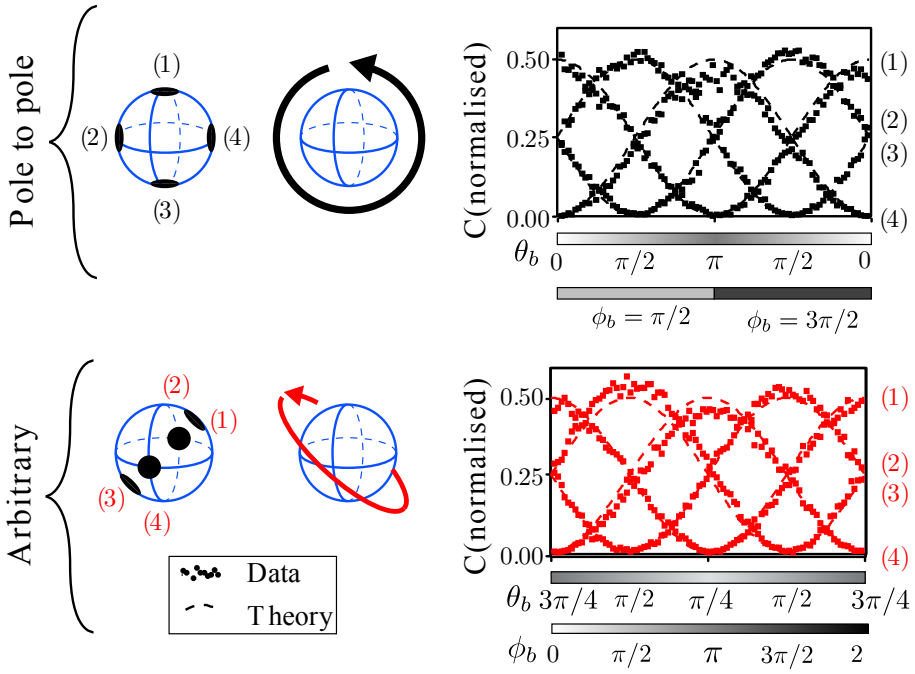


Figure 4.8: Bell curves within the $\ell = \pm 2$ subspace for states crossing both poles (top) and an arbitrarily chosen great circle (bottom). Note the close agreement with theory and experiment in each case, which is largely due to the precise intensity modulation of the states measured. This is reflected in the strong violation of the parameter S in each case.

In our method, we are not restricted to only measuring correlation between modes corresponding to great circles around the sphere. We are able to make coincidence measurements between *any* two superpositions of modes described by points $\mathbf{a}(\theta_a, \phi_a)$ and $\mathbf{b}(\theta_b, \phi_b)$, giving us access to the entire 2D state-space.

We demonstrate this by choosing one particular state, $\mathbf{a}$, and varying $\mathbf{b}$ over the full range of possible values ($\theta_b = [0, \pi]; \phi_b = [0, 2\pi]$). We can

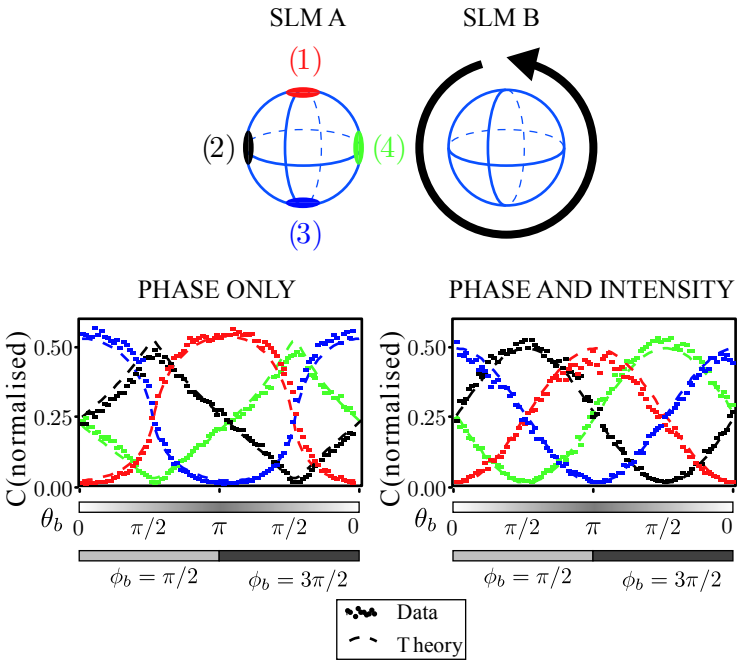


Figure 4.9: Measured correlations for phase-only holograms (left) compared with phase and intensity modulated holograms (right). As can be seen, for phase only modulation the curves are not sinusoidal, meaning that the number of modes selected by the holograms is not equal to 2.

then map out a sphere of coincidence rate between the static state in arm A, with respect to the full range of states measured in arm B. Our results are shown in Fig. 4.10 for reference holograms at a point on the equator ($\theta_a = \pi/2, \phi_a = 0$), and at a pole ($\theta_a = 0, \phi_a = 0$). As expected, we find that the coincidence rate varies sinusoidally in a great circle around the sphere with maximum counts when $\theta_b = \pi - \theta_a$ and $\phi_b = \phi_a$ and minimum counts when $\theta_b = \theta_a$ and $\phi_b = \phi_a - \pi$.

We have now established a holographic method for the arbitrary manipu-

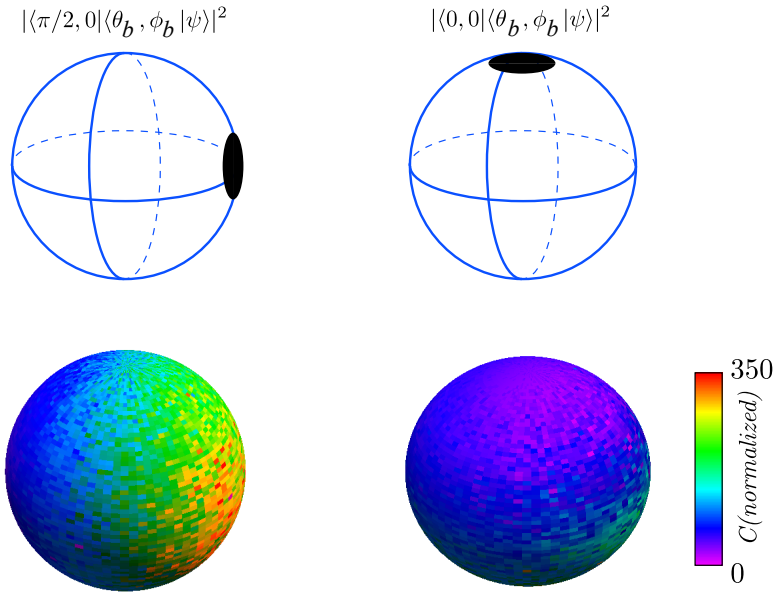


Figure 4.10: Measured correlations of the entire range of $\theta_b, \phi_b$ with respect to two different fixed reference holograms as shown. The coincidence count rates are normalized with respect to the single channel count rates as $\frac{C}{S_1 S_2 \Delta t}$ where $\Delta t$ is the coincidence gate time.

lation of OAM states within a 2D state-space. By testing this method within the context of violating a Bell-type inequality, we can confirm that we measure the desired states to a high degree of precision. Being able to measure the entire 2D state space holographically allows for further quantum tests, such as investigating the Leggett inequalities for OAM states[96,97,98].

## 4.4 Tomographic Reconstruction of Density Matrices for 2-Dimensional Orbital Angular Momentum Sub-Spaces

Any quantum system is completely characterized by its density matrix[99], which thus predicts the outcome of any measurement. The density matrix of a 2-state quantum system contains all the information on the degree to which they are entangled. Hence, a measurement based reconstruction of the density matrix with sufficient fidelity is a viable method to characterize any 2-state system as a resource for quantum information processing.

In this section we reconstruct the density matrices of the two-photon states with respect to various 2D subspaces of $+\ell$ and $-\ell$. It is important to distinguish correlated measurement outcomes that may also arise for mixed quantum states from quantum entanglement. We achieve this by reconstructing the complete density matrix of the two-photon system and evaluating various degrees of entanglement (including negativity, linear entropy, concurrence, tangle and entanglement of formation)[100,101,18]. These measures of entanglement, while theoretically involved, give quantitative measures of how pure/mixed our measured states are, and also how entangled/separable they are.

Measurements of high-dimensional OAM superposition states would allow for the practical implementation of quDits, which carry quantum information

in a D-dimensional basis. However, tomographic reconstruction of density matrices in large state spaces involves making a very large number of measurements. Here we restrict ourselves to 2-D subsystems within the OAM basis states of $\pm\ell$, ranging from $\ell = 1$ up to $\ell = 30$. This allows us to draw on tomographic methods developed for other 2-D bi-partite systems as in the polarisation basis. While the process of parametric down-conversion becomes less efficient for higher order OAM modes, the reconstructed density matrices here demonstrate that entanglement still persists for OAM states up to above $\ell = 20$.

We reconstruct the density matrices by making measurements of the pure OAM states and the equally weighted superpositions (sector states). Sector states which differ by a phase angle of $\pi/2$ are orthogonal and provide an alternate basis to the OAM basis. The sector states of interest here are the states $|\phi\rangle = |0\rangle, |\pi/4\rangle, |\pi/2\rangle$ and $|3\pi/4\rangle$, which are the equator states of the Bloch sphere analogous to the linear polarization basis states.

In the $\pm\ell$ state-space, the maximally entangled (Bell state) in both OAM and angle bases would be,

$$|\Psi\rangle = \frac{1}{\sqrt{2}}(|+\ell\rangle_s|-\ell\rangle_i + |-\ell\rangle_s|+\ell\rangle_i) \tag{4.8}$$

$$= \frac{1}{\sqrt{2}}(|\phi\rangle_s|\phi\rangle_i - |\phi+\pi/2\rangle_s|\phi+\pi/2\rangle_i), \tag{4.9}$$

meaning that the photons are anti-correlated in OAM, and correlated in

angular position. Ideally, our holographic measurements should measure this entangled state, and we will compare our experiment with this perfect case.

Any quBit density matrix can be written as,

$$\rho = \begin{pmatrix} A_{11} & A_{12}e^{i\phi_{12}} & A_{13}e^{i\phi_{13}} & A_{14}e^{i\phi_{14}} \\ A_{12}e^{-i\phi_{12}} & A_{22} & A_{23}e^{i\phi_{23}} & A_{24}e^{i\phi_{24}} \\ A_{13}e^{-i\phi_{13}} & A_{23}e^{-i\phi_{23}} & A_{33} & A_{34}e^{i\phi_{34}} \\ A_{14}e^{-i\phi_{14}} & A_{24}e^{-i\phi_{24}} & A_{34}e^{-i\phi_{34}} & A_{44} \end{pmatrix}$$

where $A_{i,j}$ are the amplitudes and $\phi_{i,j}$ the phases of the matrix elements.

The diagonal elements of the density matrix describe the probability to detect simultaneously each of the twin photons in one of the states $|+\ell\rangle$ and $|-\ell\rangle$. Determining the off-diagonal matrix elements requires measurements in superpositions of these states. The density matrix is reconstructed from projection measurements onto the 6 (non-orthogonal) states $|0\rangle$, $|\pi/4\rangle$, $|\pi/2\rangle$, $|3\pi/4\rangle$, $|+\ell\rangle$ and $|-\ell\rangle$. We measure the probability to find simultaneously each of the twin photons in one of these 6 states (36 measurements in total).

Each projection measurement can be expressed in terms of the density matrix elements $\rho_{i,j}$ , providing a set of 36 coupled equations to determine the 16 density matrix elements. In principle, a set of 16 measurements is sufficient if the corresponding transformation matrix is non-singular [100]. This procedure is favourable if a minimum number of potential measurements is required [102], however it is convenient for us to make all 36 measurements, as we can quickly switch holograms on the SLMs. This allows us to perform a

least square fit and the option to determine the largest and smallest degree of entanglement that is compatible with our measurements.

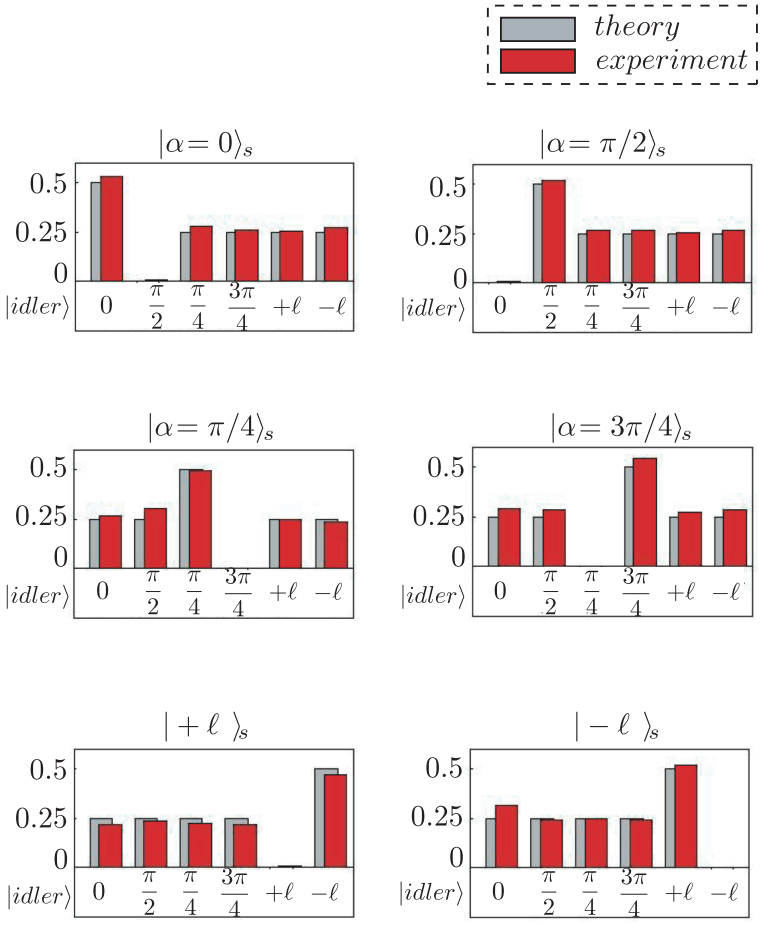


Figure 4.11: Characterization of the two-photon state by the 36 correlation measurements used to reconstruct the density matrices. These measurements demonstrate which states are correlated, anti-correlated, and only partially correlated for each basis. The example given here is for measurements in the $\ell = \pm 3$ subspace.

We measure the coincidences as we cycle the holograms in signal and

idler beam paths through the 36 possible permutations of the 6 modes in each arm.

For determining the density matrix we normalize the measured coincidence count rates with the single channel counts. This gives us the quantum contrast $QC = C/(S_1 S_2 \Delta t)$ which gives the ratio of coincidences, $C$ to accidental coincidences $S_1 S_2 \Delta t$. The 36 measurements which form the basis of the tomography are shown in Fig. 4.11 for the $\ell = \pm 3$ subspace.

### 4.4.1 Reconstructing the Density Matrix

A physically allowed density matrix needs to fulfil certain criteria: It must have a trace equal to unity and it must have positive eigenvalues, as these correspond to probabilities. This is not automatically guaranteed if we calculate the density matrix from measurements with finite precision. While the trace criterion can guaranteed with the appropriate normalization, other errors of the matrix obtained due to imperfect measurements such as negative eigenvalues cause more problems. In fact, for a strongly entangled system being close to a pure state, for which one eigenvalue is typically close to one and all the others close to zero, such errors are particularly likely. This can be caused simply by noise, but it may also sometimes indicate contributions from additional states in a larger Hilbert space, which are not perfectly filtered out in the measurements.

With the over-complete set of $N = 36$ measurements for the 16 unknowns, we can determine the density matrix that provides the best agreement with

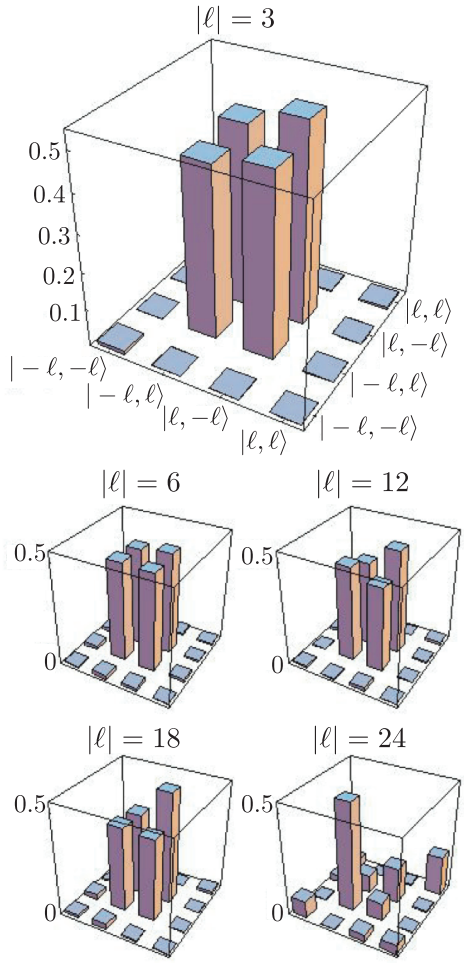


Figure 4.12: Graphical representation of the real part of the density matrix for several OAM subspaces. For $|\ell| \leq 22$ the four central entries of the density matrix dominate, indicating entanglement. For subspaces of larger $\ell$, the signal to noise ratio decreases, and the quantum conditions deteriorate.

the measured outcomes. This is done by numerically searching for the 10 independent amplitudes $A_{i,j}$ and 6 phases $\phi_{i,j}$ of the density matrix which minimizes,

$$\chi^2 = \sum_{i=1}^{36} \left( \frac{C_i^{(M)} - C_i^{(P)}}{\sqrt{C_i^{(M)} + 1}} \right) \tag{4.10}$$

In this $\chi^2$ function[103], $C^{(M)}$ is the experimentally recorded coincidence count rates, and $C^{(P)}$ are those predicted by the ideal density matrix. This minimization routine does not necessarily result in a matrix with positive eigenvalues. We therefore require the condition for positive eigenvalues as an additional constraint in the search algorithm. As an example, for the $|\ell| = 3$ subspace, this gives the density matrix with the minimum value of $\chi^2$, shown in Fig. 4.12,

$$\rho = \begin{pmatrix} 0.008 & -0.027 & -0.026 & -0.003 \\ -0.027 & 0.457 & 0.484 & -0.005 \\ -0.026 & 0.484 & 0.530 & 0.004 \\ -0.003 & -0.005 & -0.004 & 0.004 \end{pmatrix} + i \begin{pmatrix} 0 & -0.002 & 0.000 & 0.004 \\ 0.002 & 0 & 0.012 & 0.000 \\ 0.000 & -0.012 & 0 & 0.002 \\ -0.004 & 0.000 & -0.002 & 0 \end{pmatrix}$$

which has one large positive eigenvalue of 0.981, the three other eigenvalues being 0.013, 0.006 and 0.000. The sum of the squared eigenvalues is $Tr(\chi^2) = 0.963$. The large first eigenvalue, indicative of a Bell state, shows that our system is almost a pure entangled state.

While our $\chi^2$ minimisation procedure gives a valid density matrix, there are other correct solutions to the minimization which lie within our confidence limits. For a system such as ours which exhibits shot noise one would anticipate that $\chi^2/N \approx 1$. More precisely, one would expect $\chi^2$ to lie in the

range $N \pm \sqrt{2N}$[104]. Within this range of possible $\chi^2$ we use a secondary criterion to find the density matrix yielding the maximum or minimum entanglement that is consistent with the measurements, thereby establishing upper and lower confidence limits for the degree of entanglement.

For sub-spaces where the total number of counts are high, the statistical uncertainty is very low and even when minimised, the value of $\chi^2$ does not fall below the upper bound of the $N \pm \sqrt{2N}$ range. In these cases, any degradation of the experimental measurements are due to systematic noise sources such as alignment errors. In this case we simply take the $\chi^2$ minimised matrix as the optimum solution.

For higher order OAM sub-spaces where the overall count-rates are lower, the random statistical noise becomes dominant and $\chi^2$ can be reduced below the upper bound. It is in these cases that we can identify possible density matrices that yield the largest or smallest degree of entanglement. As one might expect, in the cases of extremely low count-rates the dominant statistical fluctuations mean that the least squares fit can be compatible with both large and no entanglement. Due to the presence of statistical noise in the detection system, the quality of the entangled state degrades for higher OAM sub-spaces.

### 4.4.2 Measures of Entanglement

From the two-photon density matrices we can obtain various measures of entanglement for a wide range of $|\ell|$ subspaces (linear entropy, fidelity, neg-

ativity, concurrence, tangle and entanglement of formation). A selection of these are shown in Fig. 4.13. A state is entangled if it cannot be described as the product state of its subsystems or as an incoherent mixture of such states. This feature can be quantified by evaluating the partial transpose of a two-photon state, transposing only one of the subsystems, and then identifying the eigenvalues of the partial transpose. If the system was a product state, the partial transpose would be simply the transpose of one of the subsystems, which is a valid density matrix. However if the system was entangled, the partial transpose exhibits one or more negative eigenvalues.

The linear entropy[105] $SL = \frac{4}{3}(1 - Tr(\rho^2))$ quantifies the "mixed-ness" of the state, with a pure state characterized by $SL = 0$, and a completely mixed state by $SL = 1$. We find that the measurements made within sub-spaces of small $|\ell|$ correspond closely to that of a pure state. For OAM subspaces from $|\ell| = 1$ to 20, we find values between $SL = 0.050$ and $SL = 0.350$. Photons generated with a higher OAM are found in an increasingly mixed state. The main reason for this is that the holographic post-selection technique is less efficient for high OAM states, due to pixellation on the holograms.

The fidelity[106] of a density matrix with the ideal state, the maximally entangled Bell state $\Phi_-$ is given by $F(\rho, \rho_T) = [Tr(\sqrt{\sqrt{\rho_T}\rho\sqrt{\rho_T}})]^2$, where $\rho_T$ is the density matrix of the ideal state. In our case, the target state is the Bell state, so the fidelity measure simplifies to $F = \langle\Psi|\rho|\Psi\rangle$. For OAM sub-spaces from $|\ell| = 1$ to 20, we find a fidelity ranging from $F = 0.978$ (at $|\ell| = 3$) to $F = 0.826$ (at $|\ell| = 20$). The fidelity with the maximally

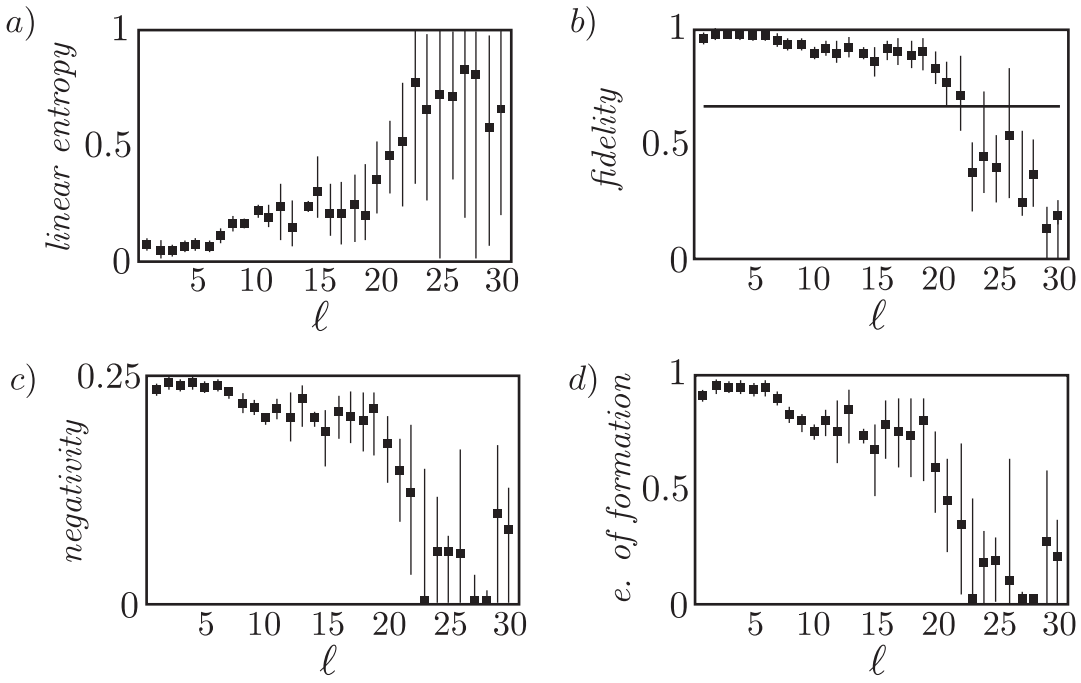


Figure 4.13: Measures of entanglement and state purity of OAM state-spaces from $|\ell| = 1$ to $|\ell| = 30$. Error bars show the maximum and minimum values of the measures which are consistent with the results. Strong entanglement persists up to around $|\ell| = 20$.

entangled Bell-state may be taken as a measure to quantify the degree of entanglement. A two-photon state cannot be described as the product state of its subsystems if the fidelity of the density matrix sinks below 2/3. In this sense, entanglement persists in our system up to the OAM subspace $|\ell| = 22$.

The negativity is defined as half the modulus of the smallest eigenvalue. For a maximally entangled state the negativity is 0.25 and is zero for a completely mixed state. For our system we find the largest negativity of

0.241 for the $|\ell| = 3$ subspace which decreases to 0.174 at $|\ell| = 20$ and almost vanishes for higher OAM subspaces as shown.

The concurrence is $C(\rho) = max(0, \lambda_1 - \lambda_2 - \lambda_3 - \lambda_4)$, where $\lambda$ are the eigenvalues, in decreasing order of the Hermitian matrix $\sqrt{\sqrt{\rho}\bar{\rho}\sqrt{\rho}}$, where $\bar{\rho}$ is obtained from $\rho$ by an OAM flip on both states[101]. For a maximally entangled state, the concurrence is equal to 1, whereas for an un-entangled state it is 0. From our measurements we calculate a concurrence ranging from $C = 0.969$ to $C = 0.700$ (at $|\ell| = 20$).

The entanglement of formation $\varepsilon$ is expressed as a function of the concurrence $C$ which also is a measure of entanglement. The entanglement of formation characterises the entanglement of a given state by the resources needed to create it. It is defined as $\varepsilon = -xlog_2(x) - (1-x)log_2(1-x)$, where $x = 1/2(1 + \sqrt{1 - C^2})$. For this parameter, we find values ranging from $\varepsilon = 0.956$ to $\varepsilon = 0.591$.

For each of the measures of entanglement, we observe the greatest degree of entanglement for low $\ell$ states, decreasing as $\ell$ increases. We observe the largest values for $|\ell| = 3$ which can be explained by the fact that the contribution of higher order sidebands generated by our segment masks are more dominant for the OAM subspaces of $|\ell| = 1$ and $|\ell| = 2$. The coincidence counts become comparable to the accidental coincidences for OAM subspaces of $|\ell| > 22$, and consequently, quantum correlations deteriorate towards this cut-off.

This method of reconstructing the density matrix of a state allows us

to calculate the degree of entanglement within each chosen $\pm\ell$ sub-space of OAM. Confirming that entanglement persists for OAM states as high as $|\ell| = 20$ gives an indication of the effective dimension of the usable Hilbert space defined by the OAM states in our experiment.

CHAPTER

# FIVE

# GHOST IMAGING USING ORBITAL ANGULAR MOMENTUM

## 5.1 Introduction

This final chapter considers a potential application of the correlated nature of down-converted photons beyond the basis of what has been considered so far. Imaging with correlated light sources allows for some interesting phenomena, such as ghost imaging, to be investigated. Ghost imaging was first proposed as an illustration of the quantum correlations between pairs of photons produced in SPDC[107]. The unique characteristic of ghost imaging is that the image emerges from the coincidences between the photon pairs, while not being present in either single arm of the system. There have been a number of experiments since the first observations over a decade ago[108,109], inves-

tigating ghost imaging using both quantum and classical light sources[110]. Although ghost imaging requires only *correlated* light, the phenomenon has remained controversial, and has led to much debate about which features of ghost imaging are quantum and which are not[111,112,113,114,115]. A recent analysis of this question may be found in reference[116].

Our down conversion experiment is suitable for implementing a ghost imaging system for two reasons. Firstly, it allows for high precision quantum measurements on states, which would allow us to test for certain quantum features. Secondly, our holographic techniques allow us to measure OAM states and spatial modes, both of which are closely related to images.

As our system has been designed for making holographic quantum measurements, as opposed to imaging, our system will be markedly different from other ghost imaging systems. We can use the nature of our experiment to make quantum measurements of a ghost image - to measure the entangled nature of the images our system produces. One way to determine whether a ghost image has quantum properties would be to test against a Bell inequality. As is now established, experimental investigation of Bell's inequality is the standard method to test whether results can be explained through local hidden-variable theories. Previous to this investigation, a Bell test approach has not been applied to the analysis of ghost images.

In classical imaging, various techniques give enhanced images. Many of these techniques were developed within microscopy and include dark-field and phase-contrast[117]. Traditionally each technique required different objective

lenses or phase filters within the microscope. However SLMs have recently been incorporated into a microscope to introduce specific phase filters so that all of these imaging modes can be sequentially implemented without any change of hardware. For example, the use of spiral phase plates introduces modes with OAM which can result in images with edge enhancement[118].

Our experiment applies these edge enhancement techniques to a down-converted ghost imaging system. Because of the non-local nature of the photons, the object can be non-local with respect to the enhancement filter, yet enhanced images can be recovered in the coincidence measurements.

## 5.2 Recording a Ghost Image

The major difference between our ghost imaging system and previous ghost imaging systems is that, while most systems incorporate a camera in one arm and a single pixel detector in the other, we incorporate single mode fibers in each arm. This is overcome by raster scanning the object in one arm to build up the image, pixel by pixel.

Images are produced from the correlations between the down-converted photons, and the spatial resolution and contrast of such images is set by the size of the detection aperture. In our experiment, the single-mode fibers ensure both high resolution and single mode selectivity.

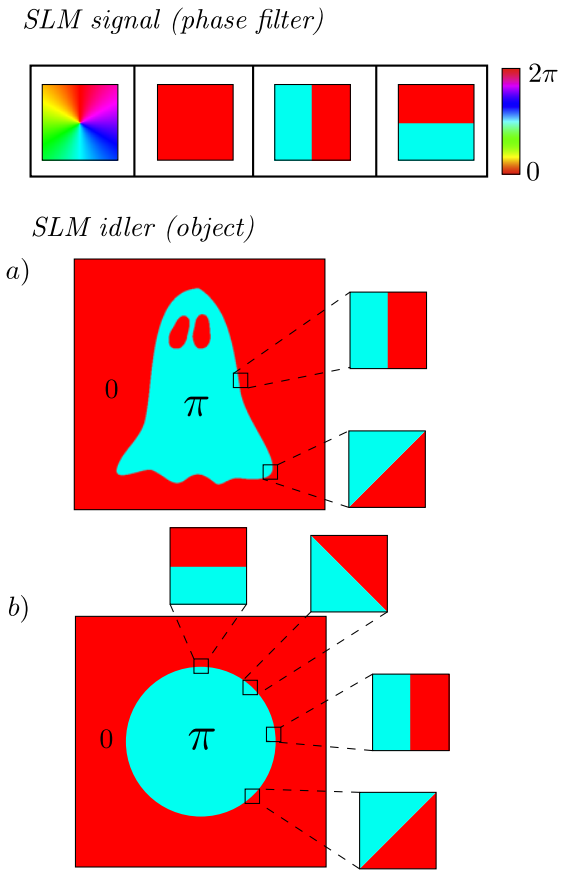


Figure 5.1: "Object" holograms used to perform ghost imaging with down-converted light. The signal SLM is used to filter out a specific OAM or sector state from the light. The idler SLM is used to represent the object, which is either a) a "ghost" b) a circular disc. The objects are a $\pi$ phase step. The objects are represented much larger than the SLM window, such that the detector only sees a small portion of the object, which - at the edge of the object - appears as a phase step with a particular orientation.

If the down-converted light is used as the illumination source for an imaging system, the spatial incoherence results in images that generally have low spatial resolution and poor contrast. However, coherent imaging can be achieved by using the correlations between the down-converted photons. The precise measurement of the position of either photon gives spatial information about the other photon, and therefore, images formed using coincidence measurements will have high spatial resolution and good contrast. Note that, for simple imaging of this type, these correlations need not be quantum in nature: all that is required is conservation of transverse momentum between the photon pairs.

In our system the object is larger than the point spread function of detection, such that we see only a small portion of the object at any one time. The image is acquired by stepping the object in the transverse plane and recording the corresponding coincidence count. For a phase object, the spatial incoherence of the source means that the image derived from the object arm alone has a very low contrast, see Fig. 5.2 (b), which decreases with increasing modal bandwidth of the down-conversion and detection processes.

When a spiral phase filter, with index $\ell_{\mathrm{ref}}$, is placed in the reference arm, the resulting coincidence count is proportional to the modal component of the object that corresponds to $\ell_{\mathrm{obj}} = -\ell_{\mathrm{ref}}$. Any part of the object described by a uniform phase corresponds to $\ell_{\mathrm{obj}} = 0$, which gives a high coincidence count for $\ell_{\mathrm{ref}} = 0$ and zero coincidence count for $\ell_{\mathrm{ref}} \neq 0$. For a part of the object containing a $\pi$-phase step, an expansion in terms of $\exp(i\ell_{\mathrm{obj}}\phi)$

gives non zero components for $\ell_{\text{obj}} = \pm 1$. Such a phase step therefore gives a high coincidence count for $\ell_{\text{ref}} = \pm 1$. Hence both $\ell_{\text{ref}} = 0$ and $\ell_{\text{ref}} = \pm 1$ give images with high-contrast edges, but with dark and bright edges respectively. A phase filter of $\ell_{\text{ref}} = 0$ results in high coincidence counts wherever the phase of the object is uniform and zero coincidence at the edge, see Fig. 5.2 (c). Also, a phase filter with $\ell_{\text{ref}} = \pm 1$ results in high coincidence counts only at positions of the phase steps, giving bright edges, see Fig. 5.2 (d). The high contrast of the images (there is no background subtraction) relies upon the spatial mode selectivity of detection and, in this case, the same images could not be obtained by using a multi-mode "bucket" detector in either the object or reference arm. (Note, in general, $\ell_{\text{ref}} = \pm 1$ will give edge enhancement to all images irrespective of the precise height of the phase step).

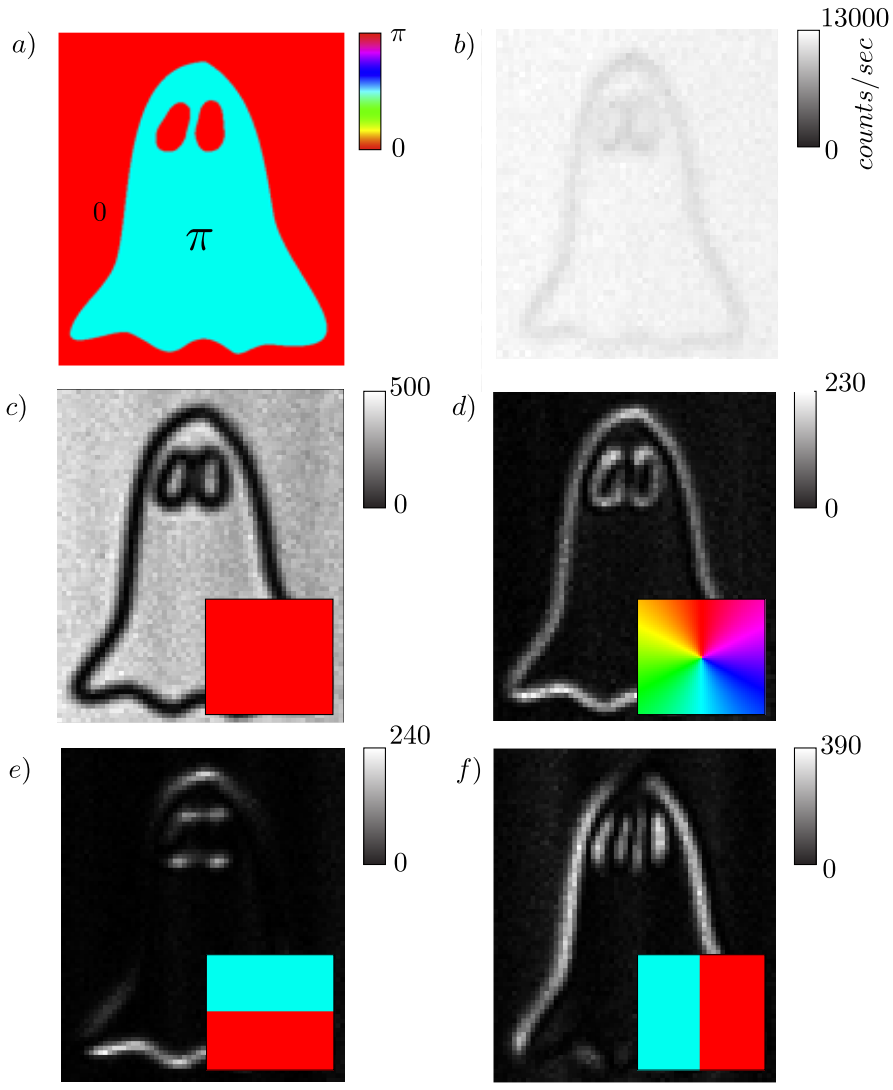


Figure 5.2: a) Phase object b) Single channel counts in the object arm, c)-f) Coincidence images of the phase object shown in (a) with each different phase filter (inset).

Although the coincidence images have features that are not present in images derived from the object detector alone, the correlations required to produce the image need not be uniquely quantum. All that is required is conservation of OAM between the photon pairs. The signature of quantum entanglement is not that correlations exist for a particular variable, but that these correlations persist when measured in a complementary basis. In the linear position-momentum case, the quantum signature is that both the image and diffraction pattern from a slit can be observed, without background subtraction[91]. For OAM, the correlations must persist between the OAM states and their superpositions. Hence, within our imaging system the complementary basis is a reference hologram formed from the linear superposition of $\ell = 1$ and $\ell = -1$, a $\pi$ phase step orientated at an angle $\theta$ - determined by the phase difference. Using this phase step as the reference hologram gives coincidence images where the contrast of the edge detection depends on the relative orientation of the edge with respect to the reference phase step, see Fig. 5.2 (e), (f).

The high contrast between parallel and orthogonal states in complementary basis sets seems to be a qualitative demonstration of the non-local correlations. However it is not sufficient to distinguish between quantum and local-realistic theories. This can be achieved by violating a Bell inequality. For this we record the coincidence rate as a function of the relative angle $\theta_s - \theta_i$ between the orientation of the edge in the object and phase step in the reference arm. Our measurements detect only superpositions of $\ell = 1$

and $\ell = -1$ and therefore our observations are sensitive only to this subspace of the OAM states; hence the two-photon entangled state is

$$|\psi\rangle = \frac{1}{\sqrt{2}}[|1\rangle_s|-1\rangle_i + |-1\rangle_s|1\rangle_i]. \tag{5.1}$$

To violate a Bell inequality the coincidence rate $C$ must vary sinusoidally. The coincidence rate is predicted to be

$$C = K\cos^2(\theta_s - \theta_i), \tag{5.2}$$

where $K$ is a constant. Such a violation can be quantified with the previously used CHSH Bell-type inequality.

By imaging a circular phase object which is much larger than the imaging point spread function, and using a $\pi$ phase step as the reference hologram, we can generate images containing all orientations of edges and measure the coincidence rate at the edges as a function of orientation. In this situation, our state-space for the transverse mode comprises the OAM states $\ell_{\text{ref}} = \pm 1$ of an equally weighted superposition. Hence we can test a Bell inequality on the $\ell = \pm 1$ subspace of transverse modes. It is known that tests on such subspaces reveal the quantum features of the full high-dimensional system[119]. Fig. 5.3 shows images of the circular phase object with the reference hologram orientation at 0°, 45°, 90° and 135° respectively. The variation in count rates for each image is shown in Fig. 5.3 (a)-(d). These curves are calculated from the azimuthal variation in count rate around the coincidence image. From

these measurements, we determine the value of $S$ to be $2.69 \pm 0.10$, clearly exceeding the local-hidden-variable bound of 2 and revealing the quantum nature of our ghost imaging arrangement. It should be noted that the calculated value of $S$ depends on the chosen radial range and in this case we average over the width of the measured signal, see dashed lines in Fig. 5.3 e). The failure to reach maximal entanglement of $2\sqrt{2}$ reflects both finite fringe contrast, and possible contamination of the single-mode detection by higher order modes ($|\ell| > 1$). Both of these effects which reduce the value of $S$.

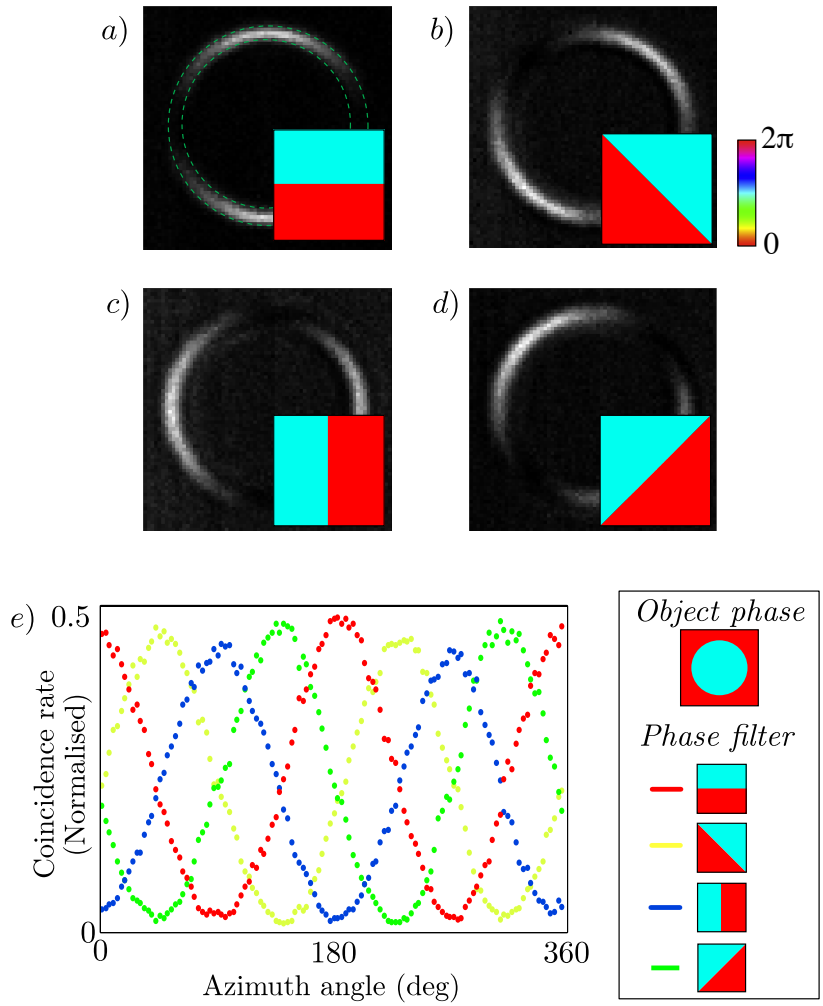


Figure 5.3: a)-d) Coincidence images for reference orientations of $0°, 45°, 90°$ and $135°$. By plotting the azimuthal intensity variations in each image (e), one can see the sinusoidal pattern in coincidence, and appropriate phase shift for each analyzer hologram.

It is important to consider what results could be achieved if our entangled source was replaced with a classical, thermal light source. Coincident images obtained with thermal light have a finite background[112,114,111] which reduces the observable contrast to the level at which there will be no violation of Bell's inequality. An explicit demonstration of this is a potential topic for future research.

We have proposed a new form of ghost imaging, where the introduction of a phase filter into one of the arms can non-locally modify the coincidence image such that its edges have enhanced contrast. The use of single mode detectors means that the images have high contrast without need for background subtraction. Although similar types of images could be generated through means of a non-entangled source, they would not have sufficient contrast to violate a Bell-type inequality. Indeed, satisfying or violating a Bell inequality as demonstrated here might reasonably be used to distinguish between classical and quantum ghost-imaging systems.

CHAPTER

# SIX

# CONCLUSIONS

This thesis presents several unique experiments designed to explore both the nature of the orbital angular momentum of light, both at the classical and quantum levels. This includes an angular analogue to linear diffraction (Angular diffraction), verified classically and non-locally on entangled photons. Following this, are a series of quantitative tests of quantum entanglement, including a new form of the EPR paradox, violation of a Bell inequality for OAM states, and fully characterising these states through tomographic reconstruction of density matrices. The final chapter reports a new form of Ghost Imaging using both OAM states and entangled photons, and highlights key quantum features in a ghost image, in a field where quantum *vs.* classical effects is a topic under debate. The techniques developed throughout the course of my PhD have the potential for widespread use, such as the devel-

opment of a holographic automatic alignment system for down-conversion experiments. This system allowed for measurements to be made over very long timescales, without the need for manual intervention, and has the potential to be made into a general purpose software package.

As is common in the experimental sciences, in the process of answering one question, many more questions are uncovered. In uncovering these questions, it is clear what lies ahead for future experiments. This includes the potential of further and more advanced tests of quantum mechanics (beyond the Bell inequality), a solid understanding of how to control the OAM bandwidth in down conversion, and how entangled ghost imaging could be used to image biological samples. These are a few of the many avenues of potential research which could be explored using the down conversion system, and holographic techniques that I developed over the past three and a half years.

# BIBLIOGRAPHY


[1] W. Heisenberg and C. Eckart. The physical principles of the quantum theory. Dover Publications, 1930.

[2] J. C. Maxwell. A dynamical theory of the electromagnetic field. Philosophical Transactions of the Royal Society of London, 155:459–512, 1865.

[3] R.A. Beth. Mechanical detection and measurement of the angular momentum of light. Physical Review, 50(2):115, 1936.

[4] D. Jackson. Classical electrodynamics, 1962.

[5] S. Pancharatnam and GW Series. Collected works of S. Pancharatnam. Oxford University Press for the Raman Research Institute, 1975.

[6] M. J. Padgett and L. Allen. The poynting vector in laguerre-gaussian laser modes. Optics communications, 121(1-3):36–40, 1995.

[7] L. Allen, S.M. Barnett, and M.J. Padgett. Optical angular momentum. Taylor & Francis, 2003.

[8] L. Allen, M. W. Beijersbergen, R. J. C. Spreeuw, and J. P. Woerdman. Orbital angular momentum of light and the transformation of laguerre-gaussian laser modes. Physical Review A, 45(11):8185–8189, 1992.

[9] J.F. Nye. Natural focusing and fine structure of light: caustics and wave dislocations. Taylor & Francis, 1999.

[10] J. Leach, M.R. Dennis, J. Courtial, and M.J. Padgett. Laser beams: knotted threads of darkness. Nature, 432(7014):165, 2004.

[11] M.R. Dennis, R.P. King, B. Jack, K. OHolleran, and M.J. Padgett. Isolated optical vortex knots. Nature Physics, 6(2):118–121, 2010.

[12] D. R. Poole, H. Scoffield, C. F. Barenghi, and D. C. Samuels. Geometry and topology of superfluid turbulence. Journal of low temperature physics, 132(1):97–117, 2003.

[13] J. Ruostekoski and Z. Dutton. Engineering vortex rings and systems for controlled studies of vortex interactions in bose-einstein condensates. Physical Review A, 72(6):063626, 2005.

[14] G. Gibson, J. Courtial, M.J. Padgett, M. Vasnetsov, V. Pas' ko, S.M. Barnett, and S. Franke-Arnold. Free-space information transfer using light beams carrying orbital angular momentum. Opt. Express, 12(22):5448–5456, 2004.

[15] M. J. Padgett and J. Courtial. Poincaré-sphere equivalent for light beams containing orbital angular momentum. Optics letters, 24(7):430–432, 1999.

[16] C.H. Bennett, G. Brassard, et al. Quantum cryptography: Public key distribution and coin tossing. In Proceedings of IEEE International Conference on Computers, Systems and Signal Processing, volume 175. Bangalore, India, 1984.

[17] P.A.M. Dirac. The principles of quantum mechanics, volume 27. Clarendon Press, 1988.

[18] S. Barnett. Quantum information. Oxford University Press, USA, 2009.

[19] S.M. Barnett and D. T. Pegg. Quantum theory of rotation angles. Physical Review A, 41(7):3427, 1990.

[20] J.B. Gotte, K. O'Holleran, D. Preece, F. Flossmann, S. Franke-Arnold, S.M. Barnett, and M.J. Padgett. Light beams with fractional orbital angular momentum and their vortex structure. Optics Express, 16(2):993, 2008.

[21] B. Jack, M. J. Padgett, and S. Franke-Arnold. Angular diffraction. New Journal of Physics, 10:103013, 2008.

[22] C. Aragone, G. Guerri, S. Salamo, and J. L. Tani. Intelligent spin

states. Journal of Physics A: Mathematical, Nuclear and General, 7:L149, 1974.

[23] S. Franke-Arnold, S.M. Barnett, E. Yao, J. Leach, J. Courtial, and M. Padgett. Uncertainty principle for angular position and angular momentum. New Journal of Physics, 6:103, 2004.

[24] D. Judge. On the uncertainty relation for lz and phi. Physics Letters, 5:189–189, 1963.

[25] D.T. Pegg, S.M. Barnett, R. Zambrini, S. Franke-Arnold, and M. J. Padgett. Minimum uncertainty states of angular momentum and angular position. New Journal of Physics, 7:62, 2005.

[26] B. Jack, P. Aursand, S. Franke-Arnold, D.G. Ireland, J. Leach, S.M. Barnett, and M.J. Padgett. Demonstration of the angular uncertainty principle for single photons. Journal of Optics, 13(064017), 2011.

[27] The nobel prize in physics, 1921.

[28] M. Planck. The Theory of Heat Radiation. Kessinger, 1914.

[29] Arthur H. Compton. A quantum theory of the scattering of x-rays by light elements. Physical Review, 21(5):483–502, 1923.

[30] E. Schrödinger. An undulatory theory of the mechanics of atoms and molecules. Physical Review, 28(6):1049, 1926.

[31] L. De Broglie. The revolution in physics: a non-mathematical survey of quanta. Noonday Press, 1956.

[32] P. Grangier, G. Roger, and A. Aspect. Experimental evidence for a photon anticorrelation effect on a beam splitter: a new light on single-photon interferences. EPL (Europhysics Letters), 1:173, 1986.

[33] A. Mair, A. Vaziri, G. Weihs, and A. Zeilinger. Entanglement of orbital angular momentum states of photons. Arxiv preprint quant-ph/0104070, 2001.

[34] A. Vaziri, G. Weihs, and A. Zeilinger. Experimental two-photon, three-dimensional entanglement for quantum communication. Physical Review Letters, 89(24):240401, 2002.

[35] C. Simon and J.W. Pan. Polarization entanglement purification using spatial entanglement. Physical Review Letters, 89(25):257901, 2002.

[36] O. Gühne and G. Tóth. Entanglement detection. Physics Reports, 474(1-6):1–75, 2009.

[37] J. Fan. Quantum state tomography of a fiber-based source of polarization-entangled photon pairs. Technical report, DTIC Document, 2007.

[38] B.J. Pors, S.S.R. Oemrawsingh, A. Aiello, M.P. Van Exter, E.R. Eliel, G.W. t Hooft, and J.P. Woerdman. Shannon dimensionality of quan-

tum channels and its application to photon entanglement. Physical Review Letters, 101(12):120502, 2008.

[39] G. Molina-Terriza, J.P. Torres, and L. Torner. Management of the angular momentum of light: preparation of photons in multidimensional vector states of angular momentum. Physical Review Letters, 88(1):13601, 2001.

[40] A. Einstein, B. Podolsky, and N. Rosen. Can quantum-mechanical description of physical reality be considered complete? Physical Review, 47(10):777, 1935.

[41] J.S. Bell. On the einstein-podolsky-rosen paradox. Physics, 1(3):195–200, 1964.

[42] S.J. Freedman and J.F. Clauser. Experimental test of local hidden-variable theories. Physical Review Letters, 28(14):938–941, 1972.

[43] Z.Y. Ou and L. Mandel. Violation of bell's inequality and classical probability in a two-photon correlation experiment. Physical Review Letters, 61(1):50–53, 1988.

[44] J.F. Clauser and M.A. Horne. Experimental consequences of objective local theories. Physical Review D, 10(2):526, 1974.

[45] A. Aspect, P. Grangier, and G. Roger. Experimental realization of einstein-podolsky-rosen-bohm gedankenexperiment: a new violation of bell's inequalities. Physical Review Letters, 49(2):91–94, 1982.

[46] A. Garg and N.D. Mermin. Detector inefficiencies in the einstein-podolsky-rosen experiment. Physical Review D, 35(12):3831, 1987.

[47] J.Å. Larsson. Bells inequality and detector inefficiency. Physical Review A, 57(5):3304, 1998.

[48] M.A. Rowe, D. Kielpinski, V. Meyer, C.A. Sackett, W.M. Itano, C. Monroe, and D.J. Wineland. Experimental violation of a bell's inequality with efficient detection. Nature, 409(6822):791–794, 2001.

[49] R. Ursin, F. Tiefenbacher, T. Schmitt-Manderbach, et al. Entanglement-based quantum communication over 144 km. Nature Physics, 3(7):481–486, 2007.

[50] D. Collins, N. Gisin, N. Linden, S. Massar, and S. Popescu. Bell inequalities for arbitrarily high-dimensional systems. Physical Review Letters, 88(4):40404, 2002.

[51] R.W. Boyd. Nonlinear optics. Academic Pr, 2003.

[52] D.N. Klyshko. A simple method of preparing pure states of an optical field, of implementing the einstein–podolsky–rosen experiment, and of demonstrating the complementarity principle. Soviet Physics Uspekhi, 31:74, 1988.

[53] S. Franke-Arnold, S.M. Barnett, M.J. Padgett, and L. Allen. Two-photon entanglement of orbital angular momentum states. Physical Review. A, 65(3B):033823–1, 2002.

[54] T. Jennewein, C. Simon, G. Weihs, H. Weinfurter, and A. Zeilinger. Quantum cryptography with entangled photons. Physical Review Letters, 84(20):4729–4732, 2000.

[55] J. Leach, M.J. Padgett, S.M. Barnett, S. Franke-Arnold, and J. Courtial. Measuring the orbital angular momentum of a single photon. Physical Review Letters, 88(25):257901, 2002.

[56] H. Wei, X. Xue, J. Leach, M.J. Padgett, S.M. Barnett, S. Franke-Arnold, E. Yao, and J. Courtial. Simplified measurement of the orbital angular momentum of single photons. Optics communications, 223(1-3):117–122, 2003.

[57] G.C.G. Berkhout and M.W. Beijersbergen. Method for probing the orbital angular momentum of optical vortices in electromagnetic waves from astronomical objects. Physical Review Letters, 101(10):100801, 2008.

[58] J.M. Hickmann, E.J.S. Fonseca, W.C. Soares, and S. Chávez-Cerda. Unveiling a truncated optical lattice associated with a triangular aperture using lights orbital angular momentum. Physical Review Letters, 105(5):53904, 2010.

[59] S.N. Khonina, V.V. Kotlyar, R.V. Skidanov, V.A. Soifer, P. Laakkonen, and J. Turunen. Gauss-laguerre modes with different indices in

prescribed diffraction orders of a diffractive phase element. Optics Communications, 175(4-6):301–308, 2000.

[60] E. Nagali, F. Sciarrino, F. De Martini, B. Piccirillo, E. Karimi, L. Marrucci, and E. Santamato. Polarization control of single photon quantum orbital angular momentum states. Arxiv preprint arXiv:0902.0740, 2009.

[61] G.C.G. Berkhout, M.P.J. Lavery, M.J. Padgett, and M.W. Beijersbergen. Measuring orbital angular momentum superpositions of light by mode transformation. Optics Letters, 36(10):1863–1865, 2011.

[62] G.C.G. Berkhout, M.P.J. Lavery, J. Courtial, M.W. Beijersbergen, and M.J. Padgett. Efficient sorting of orbital angular momentum states of light. Physical Review Letters, 105(15):153601, 2010.

[63] J.W. Pan, D. Bouwmeester, M. Daniell, H. Weinfurter, and A. Zeilinger. Experimental test of quantum nonlocality in three-photon greenberger–horne–zeilinger entanglement. Nature, 403(6769):515–519, 2000.

[64] D. Bouwmeester, J.W. Pan, M. Daniell, H. Weinfurter, and A. Zeilinger. Observation of three-photon greenberger-horne-zeilinger entanglement. Physical Review Letters, 82(7):1345–1349, 1999.

[65] H.C. Guo, Y.Q. Qin, and S.H. Tang. Parametric downconversion via

cascaded optical nonlinearities in an aperiodically poled mgo: Linbo superlattice. Applied Physics Letters, 87:161101, 2005.

[66] H. Hubel, D.R. Hamel, A. Fedrizzi, S. Ramelow, K.J. Resch, and T. Jennewein. Direct generation of photon triplets using cascaded photon-pair sources. Nature, 466(7306):601–603, 2010.

[67] J. Douady and B. Boulanger. Experimental demonstration of a pure third-order optical parametric downconversion process. Optics letters, 29(23):2794–2796, 2004.

[68] J.T. Barreiro, N.K. Langford, N.A. Peters, and P.G. Kwiat. Generation of hyperentangled photon pairs. Physical Review Letters, 95(26):260501, 2005.

[69] P.G. Kwiat, E. Waks, A.G. White, I. Appelbaum, and P.H. Eberhard. Ultrabright source of polarization-entangled photons. Physical Review A, 60(2):773–776, 1999.

[70] J.P. Torres, A. Alexandrescu, and L. Torner. Quantum spiral bandwidth of entangled two-photon states. Physical Review A, 68(5):050301, 2003.

[71] F.M. Miatto, A.M. Yao, and S.M. Barnett. Full characterization of the quantum spiral bandwidth of entangled biphotons. Physical Review A, 83(3):033816, 2011.

[72] A.M. Yao. Spectral decomposition of entangled photons with an arbitrary pump. Arxiv preprint arXiv:1012.5021, 2010.

[73] H. Di Lorenzo Pires, H.C.B. Florijn, and M.P. Van Exter. Measurement of the spiral spectrum of entangled two-photon states. Physical Review Letters, 104(2):20505, 2010.

[74] SSR Oemrawsingh, A. Aiello, ER Eliel, G. Nienhuis, and JP Woerdman. How to observe high-dimensional two-photon entanglement with only two detectors. Physical review letters, 92(21):217901, 2004.

[75] A. Aiello, S.S.R. Oemrawsingh, E.R. Eliel, and J.P. Woerdman. Nonlocality of high-dimensional two-photon orbital angular momentum states. Physical Review A, 72(5):052114, 2005.

[76] A.Y. Loudon, P.A. Hiskett, G.S. Buller, R.T. Carline, D.C. Herbert, WY Leong, and J.G. Rarity. Enhancement of the infrared detection efficiency of silicon photon-counting avalanche photodiodes by use of silicon germanium absorbing layers. Optics Letters, 27(4):219–221, 2002.

[77] R.E. Warburton, A. McCarthy, A.M. Wallace, S. Hernandez-Marin, R.H. Hadfield, S.W. Nam, and G.S. Buller. Subcentimeter depth resolution using a single-photon counting time-of-flight laser ranging system at 1550 nm wavelength. Optics Letters, 32(15):2266–2268, 2007.

[78] M.J. Stevens, R.H. Hadfield, R.E. Schwall, S.W. Nam, R.P. Mirin, and J.A. Gupta. Fast lifetime measurements of infrared emitters using

a low-jitter superconducting single-photon detector. Applied Physics Letters, 89(3):031109–031109, 2006.

[79] N.R. Heckenberg, R. McDuff, C.P. Smith, and A.G. White. Generation of optical phase singularities by computer-generated holograms. Optics Letters, 17(3):221–223, 1992.

[80] J.E. Curtis, B.A. Koss, and D.G. Grier. Dynamic holographic optical tweezers. Optics Communications, 207(1-6):169–175, 2002.

[81] D.G. Grier. A revolution in optical manipulation. Nature, 424:810–816, 2003.

[82] C. Paterson and R. Smith. Higher-order bessel waves produced by axicon-type computer-generated holograms. Optics Communications, 124(1-2):121 – 130, 1996.

[83] J Arlt, K Dholakia, L Allen, and M. J. Padgett. The production of multiringed laguerre-gaussian modes by computer-generated holograms. Journal of Modern Optics, 45(6):1231–1237, 1998.

[84] J. Leach, M. R. Dennis, J. Courtial, and M. J. Padgett. Vortex knots in light. Nature, 7:55, 2005.

[85] J. Leach, G. Sinclair, P. Jordan, J. Courtial, M. J. Padgett, J. Cooper, and Z. Laczik. 3d manipulation of particles into crystal structures using holographic optical tweezers. Optics Express, 12(1):220–226, Jan 2004.

[86] V. Y. Bazhenov, M. V. Vasnetsov, and M. S. Soskin. Laser beams with screw dislocations in their wavefronts. Optical Angular Momentum, 52(8):152, 1990.

[87] E. Yao, S. Franke-Arnold, J. Courtial, S. M. Barnett, and M. J. Padgett. Fourier relationship between angular position and optical orbital angular momentum. Arxiv preprint physics/0606142, 2006.

[88] R. Ghosh, C.K. Hong, Z.Y. Ou, and L. Mandel. Interference of two photons in parametric down conversion. Physical Review A, 34(5):3962, 1986.

[89] Y.H. Shih and C.O. Alley. New type of einstein-podolsky-rosen-bohm experiment using pairs of light quanta produced by optical parametric down conversion. Physical Review Letters, 61(26):2921–2924, 1988.

[90] P.G. Kwiat, A.M. Steinberg, and R.Y. Chiao. High-visibility interference in a bell-inequality experiment for energy and time. Physical Review A, 47(4):2472–2475, 1993.

[91] J.C. Howell, R.S. Bennink, S.J. Bentley, and R.W. Boyd. Realization of the einstein-podolsky-rosen paradox using momentum-and position-entangled photons from spontaneous parametric down conversion. Physical Review Letters, 92(21):210403, 2004.

[92] V. Boyer, A.M. Marino, R.C. Pooser, and P.D. Lett. Entangled images from four-wave mixing. Science, 321(5888):544, 2008.

[93] J.B. Gotte, S. Franke-Arnold, and S.M. Barnett. Angular epr paradox. Journal of Modern Optics, 53(5-6):627–645, 2006.

[94] D.T. Pegg, S.M. Barnett, R. Zambrini, S. Franke-Arnold, and M. J. Padgett. Minimum uncertainty states of angular momentum and angular position. New Journal of Physics, 7(05):62–62, 2005.

[95] M. D. Reid, P. D. Drummond, M. D. Reid, and P. D. Drummond. Quantum correlations of phase in nondegenerate parametric oscillation. Physical Review Letters, 60(26):2731, 1988.

[96] A. J. Leggett. Nonlocal hidden-variable theories and quantum mechanics: An incompatibility theorem. Foundations of Physics, 33(10):1469–1493, 2003.

[97] J. Romero, J. Leach, B. Jack, S.M. Barnett, M.J. Padgett, and S. Franke-Arnold. Violation of leggett inequalities in orbital angular momentum subspaces. New Journal of Physics, 12(123007), 2010.

[98] S. Groblacher, T. Paterek, R. Kaltenbaek, C. Brukner, M. Zukowski, M. Aspelmeyer, and A. Zeilinger. An experimental test of non-local realism. Nature, 446:871–875, 2007.

[99] U. Fano. Description of states in quantum mechanics by density matrix and operator techniques. Rev. Mod. Phys., 29(1):74–93, Jan 1957.

[100] D.F.V. James, P. G. Kwiat, W. J. Munro, and A. G. White. Measurement of qubits. Physical Review A, 64(5):052312, Oct 2001.

[101] W.K. Wootters. Entanglement of formation of an arbitrary state of two qubits. Physical Review Letters, 80:2245, 1998.

[102] A. Ling, A. Lamas-Linares, and C. Kurtsiefer. Accuracy of minimal and optimal qubit tomography for finite-length experiments. ArXiv: 0807.0991, page 5, 2008.

[103] W.H. Press, S. A Teukolsky, W. T. Vetterling, and B. P Flannery. Numerical recipes in C (2nd ed.): the art of scientific computing. Cambridge Univ Press, New York, NY, USA, 1992.

[104] C. I. Osorio, G. Molina-Terriza, and J. P. Torres. Correlations in orbital angular momentum of spatially entangled paired photons generated in parametric down-conversion. Physical Review A, 77(1):015810, Jan 2008.

[105] N. K. Langford, R. B. Dalton, M. D. Harvey, J. L. O'Brien, G. J. Pryde, A. Gilchrist, S. D. Bartlett, and A. G. White. Measuring entangled qutrits and their use for quantum bit commitment. Physical Review Letters, 93(5):053601, Jul 2004.

[106] R. Jozsa. Fidelity for mixed quantum states. Journal of Modern Optics, 41:2315–2323, 1994.

[107] A.V Belinskii and D.N. Klyshko. Two-photon optics. Soviet Physics Uspekhi, 78, 1994.

[108] T.B. Pittman, Y.H. Shih, D.V. Strekalov, and A.V. Sergienko. Optical imaging by means of two-photon quantum entanglement. Physical Review A, 52(5):3429–3432, 1995.

[109] DV Strekalov, AV Sergienko, DN Klyshko, and YH Shih. Observation of two-photon ghost interference and diffraction. Physical review letters, 74(18):3600–3603, 1995.

[110] D. Magatti, F. Ferri, A. Gatti, M. Bache, E. Brambilla, and L.A. Lugiato. Experimental evidence of high-resolution ghost imaging and ghost diffraction with classical thermal light. Arxiv preprint quant-ph/0408021, 2004.

[111] R.S. Bennink, S.J. Bentley, R.W. Boyd, and J.C. Howell. Quantum and classical coincidence imaging. Physical Review Letters, 92(3):33601, 2004.

[112] A. Gatti, E. Brambilla, M. Bache, and L.A. Lugiato. Correlated imaging, quantum and classical. Physical Review A, 70(1):013802, 2004.

[113] R.S. Bennink, S.J. Bentley, and R.W. Boyd. two-photon coincidence imaging with a classical source. Physical Review Letters, 89(11):113601, 2002.

[114] M. D'Angelo, Y.H. Kim, S. P. Kulik, and Y.H. Shih. Identifying entanglement using quantum ghost interference and imaging. Physical Review Letters, 92(23):233601, Jun 2004.

[115] B. I. Erkmen and J. H. Shapiro. Ghost imaging: from quantum to classical to computational. Advances in Optics and Photonics, 2(4):405–450, Dec 2010.

[116] A. Gatti, E. Brambilla, M. Bache, and L.A. Lugiato. Quantum Imaging. Springer, New York, NY, USA, 2007.

[117] E. Hecht. Optics. Pearson Education, Essex, United Kingdom, 2001.

[118] S. Fürhapter, A. Jesacher, S. Bernet, and M. Ritsch-Marte. Spiral phase contrast imaging in microscopy. Optics Express, 13(3):689–694, Feb 2005.

[119] N. Gisin. Bell's inequality holds for all non-product states. Physics Letters A, 154(5-6):201 – 202, 1991.